IOWA STATE UNIVERSITY
Digital Repository

Retrospective Theses and Dissertations

Large eddy simulations of a confined rectangular jet

Anup Ganesh Gokarn
Iowa State University

Recommended Citation

Large eddy simulations of a confined rectangular jet

by

Anup Ganesh Gokarn

A dissertation submitted to the graduate faculty

in partial fulfillment of the requirements for the degree of

DOCTOR OF PHILOSOPHY

Major: Mechanical Engineering

Program of Study Committee:
Francine Battaglia, Major Professor
Rodney O. Fox
James C. Hill
Shankar Subramaniam
Michael G. Olsen

Iowa State University

Ames, Iowa

2007

UMI Number: 3259464

UMI®

TABLE OF CONTENTS

LIST OF TABLES

LIST OF FIGURES

x

NOMENCLATURE

C_s	Smagorinsky coefficient
$\mathcal{D}$	molecular diffusivity
u_i	velocity vector
p	pressure
Re	Reynolds number
S_{ij}	rate of strain tensor
$|S|$	magnitude of rate of strain tensor
Sc	molecular Schmidt number
Sc_t	turbulent Schmidt number
l_{ij}	Leonard tensor
c_{ij}	Cross stresses
r_{ij}	Reynolds stresses
T_{ij}	subfilter stress tensor
t	time
x_i	space vector
t	time
G	filter function

Greek Symbols

δ	spatial or temporal increment
Δ	filter width

η	Kolmogorov scale
λ_B	Batchelor scale
λ_i	subgrid scalar flux vector
Λ_i	subfilter scalar flux vector
μ	dynamic viscosity
ν	kinematic viscosity
ν_t	turbulent or eddy viscosity
ϕ	passive scalar
ρ	density
σ_{ij}	viscous stress tensor
τ_{ij}	subgrid stress tensor
Ω_{ij}	rate of rotation tensor

Superscripts

$'$	RMS variable
$''$	subgrid component

Subscripts

i, j	Components of vectors and tensors

List of Operators

∇	gradient operator
$\nabla\cdot$	divergence operator
∇^2	Laplacian operator
$\nabla\times$	curl operator

	grid–filtering operation
$\widehat{\ },\widetilde{\ }$	test–filtering operation
$\langle\rangle$	ensemble mean

Abbreviations

CFL	Courant-Fredrichs-Lewy number
DNS	direct numerical simulations
LES	large eddy simulations
PDF	probability density functiom
RANS	Reynolds averaged Navier–Stokes equations
SGS	subgrid scale

ABSTRACT

Turbulent flows have the ability to transport momentum and mix species at a higher rate than molecular diffusion alone, which is critical in reacting flows. Of importance to this research is the mixing of liquid-phase high Schmidt number flows for applications in the chemical process industry. Computational fluid dynamics (CFD) has the potential to be used as a tool to improve reactor designs and examine the mixing characteristics but requires extensive validation of the computational models. This research presents detailed analysis and validation of a nonreacting turbulent flow for a confined rectangular jet with a co-flowing fluid using CFD. Large eddy simulations (LES) for the incompressible filtered Navier–Stokes equations are performed on a partially staggered finite difference grid. A second-order central difference scheme and sixth-order compact scheme are employed for the spatial derivatives. A third-order low storage Runge–Kutta method is used for the temporal derivatives. To reduce computational memory and time requirements, message passing interface (MPI) is implemented and an efficient parallel linear equation solver (Aztec) is utilized for solving the elliptical pressure Poisson equation. Solutions for the momentum and non-reacting scalar transport are obtained for a Reynolds number of 20,000 based on the average velocity at inlet and hydraulic diameter. Validation is performed for the LES by comparing one-point and two-point statistics with particle image velocimetry data for the velocity field and planar laser induced fluorescence measurements for the scalar concentration. Such detailed validation with experiments is performed for the very first time. The effect of different parameters such as grid resolution, numerical schemes and subgrid models on the numerical solution are studied. For the scalar transport, numerical schemes that preserve boundedness are tested and implemented. Overall, the LES compared very well with the experiments and recommendations are made to extend the LES work toward reacting flows.

CHAPTER 1. INTRODUCTION

1.1   Motivation and objective

Turbulent flows have the ability to transport momentum and mix species at a higher rate than molecular diffusion alone. The process of turbulent mixing in reacting flows becomes important when the goal is to increase reaction rates by increasing surface area for molecular contact. In the chemical process industry, proper mixing is necessary to control product formation and therefore a well-designed reactor plays a key role. Computational fluid dynamics (CFD) has the potential to be used as a tool to improve reactor designs and systematically examine the mixing of reactants, since it is a relatively inexpensive approach compared to the costs associated with experiments.

For modeling purposes, reacting flows are often classified based on the time scales for reaction and turbulent mixing. The Damköhler number is a non–dimensional number which is used to describe the ratio of mixing and reaction time scales. A high Damköhler number indicates a process with fast reaction rates that is diffusion limited. A low Damköhler number indicates slow reaction rates where the reactants are mixed homogeneously before any reaction occurs. For slow reactions, often, assumptions of homogeneous mixing are made before the reaction mechanism is taken into account. However, for processes in which the reaction time scale is less than or on the same order as the mixing time scale (finite–rate reactions), both processes are important. Examples include reactive precipitation and free–radical polymerization, which involve fast and finite–rate chemical reactions whereby product distribution is affected by turbulent transport. Currently, CFD models that can describe the physical interactions between mixing and chemical reactions for finite–rate reactions have not been fully validated for liquid-phase reactions. In such cases, models based on the moments of the concentration fields have

been inadequate for predicting product selectivity[1]

To obtain numerical solutions for turbulent flow problems, the three main approaches are:

1. Direct numerical simulation (DNS), in which all scales of turbulence are resolved.

2. Large eddy simulation (LES), in which the large energy containing scales of motion are solved, and the small unresolved (subgrid) scales and their interactions on the large scales are modeled.

3. Reynolds-averaged Navier–Stokes (RANS) calculations, in which all scales of turbulence are modeled.

The LES approach stands in between DNS and RANS methods. DNS is mainly used to solve low Reynolds number flow problems where the range of scales present is small, and is not feasible for practical flows at high Reynolds numbers. RANS is the method of choice for most flows of practical importance where complex geometries and high flow rates are present because the resolution requirements are low as compared to DNS and LES. However, when compared to RANS, LES can provide much more accurate data. Flows in the chemical process industry often involve large-scale, time-dependent phenomena which have significant influence on turbulent transport, but which are not resolved at the level of one-point turbulence models. This accuracy comes at a higher computational cost, however, with an increase in computational power and parallel computing techniques, LES solutions can be obtained in a reasonable amount of time. LES has achieved success in turbulent flow predictions due to the fact that large scales are the rate controlling process in a flow and small scale interactions can be approximated by models. This advantage of LES is questionable for reacting flows, since reactions occur at the molecular level (subgrid scales). For liquid phase reactions, where the molecular diffusion occurs in a thin region (as compared to gases), the subgrid scalar variance can be large and LES fails to give a good prediction since all subgrid information is lost. Closure models similar to those in RANS calculations must therefore be used for LES and the development of subgrid scale closures for macroscopic simulations of turbulent reacting flows are therefore important.

---

[1]For reactions that produce more than one byproduct, product selectivity is the formation of a favorable product instead of an unwanted one.

Closures based on moment methods, conditional moment methods and probability density function (PDF) methods, although well understood (Baldyga and Henczka, 1997; Baldyga and Bourne, 1999; Pipino and Fox, 1994; Tsai and Fox, 1996), have not been fully validated for liquid–phase reacting flows. For simple reactions, the presumed PDF approach has shown success in LES for modeling the subgrid scalar variance. For more complex reactions, the only known form of complete closure for the chemical source term is based on the transported PDF approach, where a transport equation is solved for the joint scalar PDF. Such a PDF code has been developed and validated at Iowa State University (Raman et al., 2004). However, validation of subgrid models has not been performed for liquid-phase reacting flows due to lack of experimental data. The main motivation of this research is the detailed validation of subgrid models for liquid–phase (low molecular diffusion) chemical reactions.

A reactor configuration has been designed and built at Iowa State University to obtain measurements of the turbulent flow field and the concentration fields inside a liquid-phase chemical reactor. Figure 1.1 shows a photograph of the reactor along with a schematic. Although the configuration is not common for industrial applications, the design is kept simple for ease of measurements and CFD simulations. Common industrial reactor designs include stirred tanks (Patterson, 1990) and tubular designs (Brodkey, 1974; Forney et al., 1996). Figures 1.2-1.4 are schematics of reactor designs for non–premixed inlet conditions, each representing different ways of introducing reactants into the reactor (A and B represent the reactants and P the final product). A continuously stirred tank reactor (CSTR) is shown in Fig. 1.2 and is used for non–corrosive applications. If the reactants have a corrosive effect on the mixer, this configuration cannot be used. Industrial gas–phase chlorination processes typically use coaxial, jet–stirred reactors as shown in Fig. 1.3. Forney et al. (1996) find the configuration of a turbulent jet in a cross-flow or tee-mixer (Fig. 1.4) to be the most efficient passive design for fast reactions that require short residence times. The rectangular reactor (Fig. 1.1) in the present research is 1.0 m long and has a cross–sectional dimension of 0.06 m by 0.1 m. The inflow to the reactor is separated by two splitter plates. The lengths of splitter plates are 0.08 m within the test section. The three inlet streams are denoted in Fig. 1.1 by A, B and C. Measurements are obtained using particle image velocimetry (PIV) for the flow (velocity field)
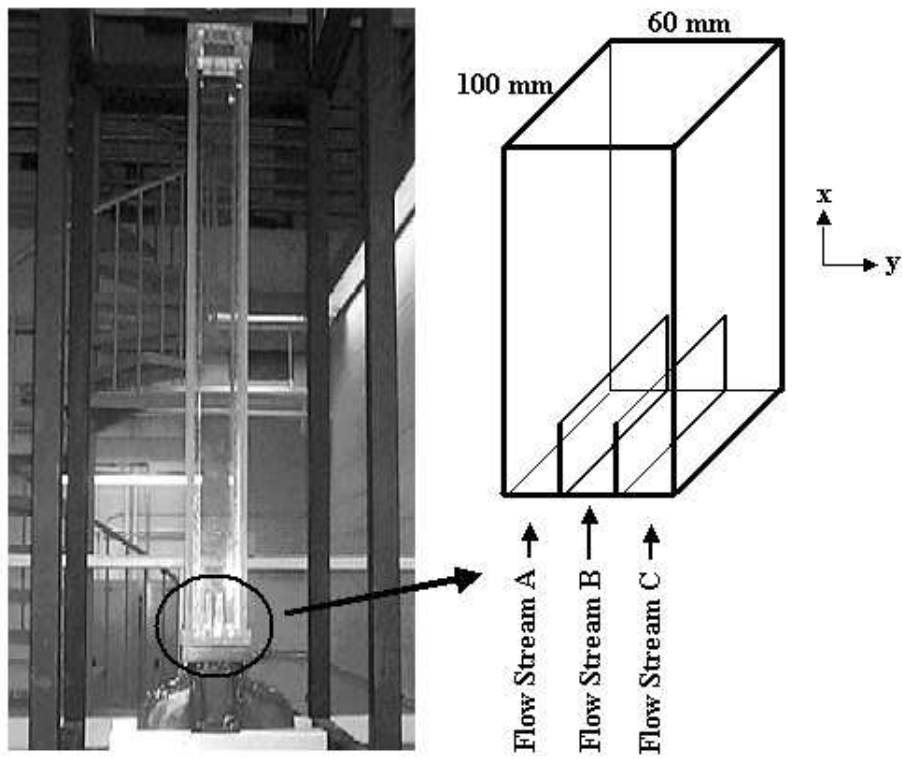
Figure 1.1   Photograph and schematic of confined rectangular jet reactor.
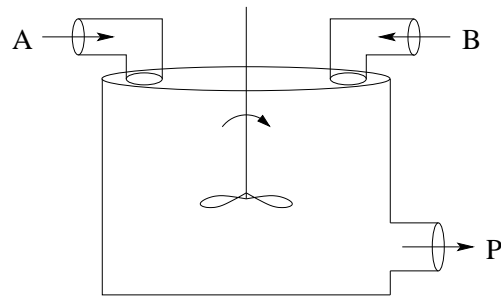
Figure 1.2   Schematic of a continuously stirred tank reactor with non–premixed feeds.
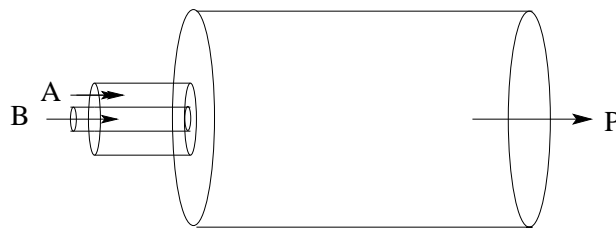
Figure 1.3   Schematic of a coaxial jet stirred tubular reactor.
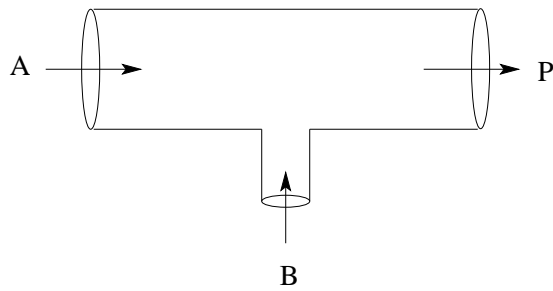
Figure 1.4   Schematic of a mixing–tee reactor.

and planar laser induced fluorescence (PLIF) techniques for the concentration field (Feng et al. 2005).

Given the scope and extent of the research required for model validation of liquid-phase reacting flows, the present work aims at the following:

1. Develop a stable LES solver and test the performance of the numerical scheme and the subgrid model.

2. Implement message passing interface (MPI) routines into the LES solver and couple an external parallel linear equation solver for the pressure solution.

3. Implement an inflow turbulence generation technique to mimic experimental conditions.

4. Implement and study the effect of different subgrid models on LES solutions and validate with PIV measurements.

5. Implement a numerical scheme that preserves scalar boundedness for non-reacting scalar transport and validate solutions with PLIF measurements.

1.2 Thesis organization

A summary of literature on the study of mixing layers and LES is presented in chapter 2. In chapter 3, details of the numerical scheme and LES subgrid models are presented. Chapter 4 illustrates benchmark simulation results that validate the numerical solution procedure, the subgrid model and performance study of the parallel solver. Chapters 5 and 6 present LES solutions for the reactor configuration for the momentum and scalar transport, respectively. Validation of one-point and two-point velocity and scalar statistics are performed using experimental data. Summary and future work of the project are presented in chapter 7.

CHAPTER 2.   LITERATURE REVIEW

In this chapter, past studies on mixing layers and subgrid models are reviewed. The increase in computational power in the last thirty years has been a motivating factor in building and improving models to describe turbulent flows. Some of these LES models are discussed in the context of the present study.

2.1   The mixing layer

Turbulent mixing has been the focus of research for over three decades. A mixing layer is formed when two fluids of unequal velocity flow parallel to each other and interact. Turbulent mixing layers have been the subject of extensive experimental, numerical and theoretical studies due to their common occurrence and significant importance in mixing processes, often combined with chemical reactions and combustion.

The classical picture of turbulence was one of chaos and was therefore surprising when shadow graphs of flow forming a shear layer revealed the presence of well-defined large structures with the appearance of rollers or vortices (Winant and Browand, 1974; Brown and Roshko, 1974; Roshko, 1976; Browand and Weidman, 1976; Dimotakis and Brown, 1976; Ho and Huang, 1982; Browand and Ho, 1983; Dimotakis, 1986; Koochesfahani and Dimotakis, 1986; Slessor et al., 1998). The mean flow is controlled by these large and organized structures, which are not affected by the small-scale turbulence appearing at high Reynolds numbers. The measured mean properties of the flow, velocity and density profiles, spreading rate, etc. do not vary much over a wide range of Reynolds numbers. The vortex size and spacing are related to the thickness of the mixing layer. Pairing is the dominant mode of vortex interaction and the principal mechanism of growth. In pairing, neighboring vortices rotate around each other and coalesce into a larger structure (Roshko, 1976). A fundamental property of turbulent shear flows is entrainment:

8

the incorporation of non-turbulent, irrotational fluid into the turbulent region. Continuous repetition of the pairing process is responsible for the entrainment of the surrounding fluid, controlling the growth of the mixing layer (Browand and Weidman, 1976). The structures derive energy directly from the velocity difference between the two streams and pairing is a result of the instability of vortical structures (Winant and Browand, 1974). Existence of vortical structures for Reynolds numbers as high as 3×10^6 proves that the structures persist at high Reynolds number flows and are not just at transition from the well-defined periodicity of the laminar instability region (Dimotakis and Brown, 1976). Reynolds-stress production is associated with the pairing interaction of vortices (Browand and Weidman, 1976) and half of the turbulent kinetic energy is associated with the vortices (Browand and Ho, 1983). Vortex interactions are thus responsible for the cross-stream momentum transfer. An important feature of the mixing layer that was discovered is asymmetric mixing of the two fluids in the mixing layer (Koochesfahani et al., 1983; Mungal and Dimotakis, 1984; Grinstein et al., 1985; Koochesfahani and Dimotakis, 1986; Masutani and Bowman, 1986), that is, there is more high-speed fluid than low-speed fluid entrained and mixed in the coherent structures.

In addition to the primary two-dimensional vortical structures, it has been observed that the plane free shear layer also contains a well organized array of streamwise vortices that superimpose onto spanwise eddies (Bernal and Roshko, 1986; Lasheras et al., 1986). Results have shown that the streamwise structures first form in the braided region, a region connecting adjacent spanwise vortices that lacks significant spanwise vorticity and are dominated by large-scale strain (Bernal and Roshko, 1986; Lasheras et al., 1986; Rogers and Moser, 1992). The existence of counter-rotating streamwise vortices connecting the primary spanwise rollers were found. Lasheras et al. (1986) provide an explanation for the qualitative evolution of the layer. The most extensive set of direct numerical simulations of temporally evolving mixing layers have been reported by Rogers and Moser (Rogers and Moser, 1992; Moser and Rogers, 1993). These simulations have yielded complete details of the mixing layer structure and dynamics, starting from the formation of the initial spanwise vortex rollup leading into the evolution of the mixing layer up to the third pairing.

The bulk of research effort on the mixing layer has been primarily experimental. The

progress in computational power, such as memory and high-speed processors, has provided greater opportunities to investigate high Reynolds number turbulent flows using direct numerical simulations and large eddy simulations. Some methods used to simulate the mixing layer are outlined to demonstrate the progress in this area.

1. Flux-Corrected Transport (FCT), a nonlinear, monotone, finite-difference technique is used for solving the governing equations (Grinstein et al., 1985). FCT adds linear velocity-dependent diffusion to a high-order algorithm during convective transport. Fourth-order accuracy is maintained by subtracting out the added diffusion during a second nonlinear anti-diffusion stage.

2. A high-order, finite-element spectral method was used by Korczak and Wessel (1989). Functions are represented as tensor-product Lagrangian interpolants through Gauss-Lobatto-Chebyshev collocating points. An explicit method with third-order Adams-Bashforth is used for the nonlinear terms. The pressure and viscous parts are solved implicitly with variational projection operators based on Chebyshev polynomial expansions. The solver is either a direct matrix inversion or an iterative conjugate gradient method.

3. Direct lagrangian simulations (DLS) using a "transport-element" method was used to simulate an inviscid mixing layer (Battaglia and Givi, 1993). The Lagrangian simulation is a "grid free" discretization of the transport equations for the vorticity and for the gradients of the mixture fraction. A beta density model was used to calculate the probability distribution of an appropriately defined Shvab-Zel'dovich variable. A gradient diffusion model was used to account for the effects of turbulent convective fluxes.

4. A methodology named the filtered mass density function (FMDF) was developed and implemented for large eddy simulations of variable-density chemically reacting turbulent flows at low mach numbers (Jaberi et al., 1999). The FMDF represents the joint probability density function of the subgrid-scale (SGS) scalar quantities and is obtained by solving a model transport equation. The chemical reaction source term appears in a closed form

and the influences of SGS mixing and convection are modeled. The equations are solved via a lagrangian Monte Carlo scheme.

5. The evolution of a temporal mixing layer was studied by Vreman et al.(1997) at high Reynolds numbers to study the effect of different subgrid models on the solution. Finite differencing was used with up to fourth-order discretization. They found the dynamic model to give the best approximation to a self-similar state.

2.2   Large eddy simulations

Large eddy simulations directly solve the large scale resolvable flow field and incorporate the small scale turbulent behavior using models. LES can provide closure data for lower–level turbulence models at high Reynolds numbers and for complex geometries beyond the reach of DNS (Piomelli, 1999). Since LES is the choice of methodology adopted in the present study, detailed formulation of equations is given in chapter 3. Here, various models are discussed with respect to the SGS stresses. An analogous procedure is applicable to the turbulent scalar flux. The effect of the unresolved scales appears through the SGS term,

$$\tau_{ij} = (\overline{u_i u_j} - \overline{u}_i \overline{u}_j) = l_{ij} + c_{ij} + r_{ij}$$

where

$$
\begin{aligned}
l_{ij} &= \left(\overline{\overline{u}_i \overline{u}_j} - \overline{u}_i \overline{u}_j\right) \\
c_{ij} &= \left(\overline{\overline{u}_i u_j''} + \overline{u_i'' \overline{u}_j}\right) \\
r_{ij} &= \left(\overline{u_i'' u_j''}\right)
\end{aligned}
$$

The turbulent velocity field u_i is represented by the resolved field, $\overline{u}_i$ and the unresolved field, u_i'' and l_{ij} are the Leonard stresses (Leonard, 1974), c_{ij} are the cross terms and r_{ij} are the SGS Reynolds stresses. The Leonard stresses represent interactions between resolved scales that result in subgrid scale contributions and can be explicitly calculated. The cross terms represent interactions between the resolved and unresolved scales and the SGS Reynolds stresses represent the interaction between the unresolved scales. While the Reynolds stresses are Galilean

invariant, l_{ij} and c_{ij} are not (Pope, 2000) and hence, the term τ_{ij} is modeled instead of each term separately. In LES, the dissipative scales are either resolved poorly, or not at all and it is the subgrid model which removes energy from the resolved scales, mimicking the drain associated with the energy cascade. Thus, most subgrid scale models are eddy viscosity models of the form

$$\tau_{ij} - \frac{1}{3}\tau_{kk}\delta_{ij} = -2\nu_t \overline{S}_{ij}$$

where ν_t is the eddy-viscosity, δ_{ij} is the Kronecker delta function, and the filtered rate of strain tensor is

$$\overline{S}_{ij} = \frac{1}{2}\left(\frac{\partial \overline{u}_i}{\partial x_j} + \frac{\partial \overline{u}_j}{\partial x_i}\right)$$

A simple algebraic model was proposed by Smagorinsky (1963) and is still being used for many engineering flows.

$$\nu_t = \left(C_s \overline{\Delta}\right)^2 |\overline{S}|$$

where,

$$|\overline{S}| = \sqrt{2\overline{S}_{ij}\overline{S}_{ij}}$$

For isotropic turbulence, a value of C_s between 0.18 and 0.23 has been found to be satisfactory. For channel flows, due to the presence of solid boundaries, a lower constant has to be used. The length scales reduce near boundaries and functions such as the van Driest damping function (van Driest, 1956) must be used. Thus, a major drawback of the Smagorinsky model is its inability to correctly represent different kinds of flows with a single universal constant.

In 1991, Germano et al. presented a novel idea in which the model coefficient is computed dynamically as the calculation progresses. The dynamic model was a major development in the area of LES and subsequently, the model was applied to compressible turbulent flows and scalar transport (Moin et al., 1991). A modification to the Germano model was proposed by Lilly (1992) to minimize the difference between the closure assumption and the resolved stresses, and proved to be more amenable to numerical solutions. The dynamic model and its variants have been widely used and validated for various complex engineering flows. A feature common to all the dynamic models is that the model is unstable unless some kind of averaging is performed. The dynamic models were first tested for flows with at least one homogeneous direction and

hence the averaging was carried out over planes of directional homogeneity. For dynamic models to be applicable for inhomogeneous flows, a variety of averaging techniques have been proposed. Examples of currently recognized models were developed by Zang et al. (1993) and Piomelli and Liu (1995) using local spatial averaging. Ghosal et al.(1995) solved an integral equation where the solution yields the model coefficient as a function of space and time. Meneveau et al.(1996) used a Lagrangian dynamic model to accumulate the required averages over flow pathlines. Models based on a second-order velocity structure function (structure function model and filtered structure function model) were proposed (Métais and Lesieur, 1992; Ducros et al., 1996). The models are based on the local kinetic energy spectrum and take into account the local intermittency of turbulence. Unless modeled, information about the subgrid kinetic energy (K_{sgs}) is not available in an LES simulation. K_{sgs} is defined as $\frac{1}{2}\left(\overline{u_i u_i} - \overline{u}_i \overline{u}_i\right)$ and can be used to provide velocity scale information for the eddy viscosity (analogous to the k-equation in RANS model). A transport equation thus needs to be solved for K_{sgs}. Variations of this model can be found in literature (Menon et al., 1996; Ghosal et al., 1995).

The eddy viscosity models are able to represent the dissipative effects satisfactorily. However for transitional flows where energy is transferred to and fro between the large and the small scales, eddy viscosity models have not been able to reproduce the stresses accurately (Liu et al., 1994). Scale–similar and mixed models are able to account for this energy transfer and are based on the assumption that the largest subgrid scales interact with the smallest resolved scales (Bardina et al., 1980). Germano (1986) suggested a form of decomposition in which each component of the residual stress is Galilean invariant.

$$\tau_{ij} = l_{ij}^0 + c_{ij}^0 + r_{ij}^0$$

where

$$
\begin{aligned}
l_{ij}^0 &= \left(\overline{\overline{u}_i \overline{u}_j} - \overline{\overline{u}}_i \overline{\overline{u}}_j\right) \\
c_{ij}^0 &= \left(\overline{\overline{u}_i u_j''} + \overline{u_i'' \overline{u}_j} - \overline{\overline{u}}_i \overline{u''}_j - \overline{u''}_i \overline{\overline{u}}_j\right) \\
r_{ij}^0 &= \left(\overline{u_i'' u_j''}\right)
\end{aligned}
$$

The SGS stress can then be written as

$$\tau_{ij} = -2\nu_T \overline{S}_{ij} + \left(\overline{\overline{u}_i \overline{u}_j} - \overline{\overline{u}}_i \overline{\overline{u}}_j\right)$$

where the last term in brackets is the scale–similarity model and the eddy viscosity term provides the dissipation that is underestimated by the scale–similar part alone. Together they are called mixed models. Models based on a "deconvolution" method where an approximation of the turbulent field is obtained by operating an inverse filter on the resolved field have been proposed (Guerts, 1997; Stolz and Adams, 1999; von Kaenel et al., 2002). Detailed reviews on the development of LES are provided by Rogallo and Moin (1985), Galperin and Orszag (1993), Lesieur and Métais (1996), Piomelli (1999), Meneveau and Katz (2000), Piomelli and Balaras (2002) and Berselli et al. (2006).

With so many models available in literature, a natural question follows, "which is the *best* LES model?" and the answer probably is "there is no universally best LES model" which is perhaps why there are so many models in the first place. With the advent of fast processors and parallel computing, the complexity and accuracy of subgrid models have been increasing. However, the models must to be tested to find the best model for a particular application. The present study aims at understanding the effect of a selective set of subgrid models on the resolved scales in a complex flow configuration. Validation of the numerical algorithm and subgrid model is made by comparing solutions with DNS and experimental results in literature. A thorough validation of the flow in confined jet reactor is made with experimentally measured data for the velocity and scalar field, including two-point spatial correlations that represent length scales in the flow. With access to parallel clusters, the study makes extensive use of high performance computing to obtain solutions in a reasonable amount of time. The present work is a part of study which aims to validate computational models for turbulent reacting flows. Fast computations are therefore necessary if reacting scalars are to be solved, since reacting flows involve solutions of transport equations for multiple species.

CHAPTER 3.   NUMERICAL SOLUTION OF LARGE EDDY SIMULATION

Numerical solutions to the incompressible Navier–Stokes equations have been documented since the early 20th century (Thom A., 1933). Mathematically, the incompressible flow equations present unique issues with satisfying the incompressibility requirement. In an incompressible medium, pressure information travels at infinite speed, which is the root cause of all problems. In literature, two distinct approaches for satisfying this incompressibility constraint have been documented, and the differences in the solution procedure stem from the choice of the method. In "pressure-based" methods, the incompressibility constraint is satisfied directly by decoupling pressure from the momentum equations and then solving the pressure Poisson equation (Chorin, 1968, Harlow and Welch, 1965). The second method closely mimics the compressible flow formulation, where momentum and continuity equations are coupled through density and incompressibility is recovered in a limiting sense. This class of method is referred to as a "density-based" method and is coupled with the artificial compressibility formulation (Chorin, 1967, Merkle, 1994).

Pressure-based methods solve the elliptic pressure Poisson equation where a sparse matrix is inverted every time step. In the density-based method, a time derivative of the pressure term is added to the continuity equation. The governing equations are iterated in "pseudo-time" until convergence, which is done for every time step. Efficient algorithms (e.g., preconditioning techniques) are often employed to obtain fast convergence. Both methods have been used by researchers and there is no evidence of the superiority of one method over another. Occasionally, instead of pressure and velocity, variables such as vorticity and stream function have been used. However, the use of the vorticity-stream function approach has been limited due to increased computational costs for three-dimensional calculations. Over the years, the CFD community

has seen improvements in numerical algorithms, in terms of both speed and accuracy, and the ability to obtain solutions for complex geometries and systems, all due to tremendous improvements in computing power. This is especially important for turbulent flow calculations, which encompass a wide range of length and time scales. High grid resolution and small time steps lead to long calculation times, and what takes weeks on a single computer can now be completed in a matter of hours on a supercomputer.

In the present work, a partial staggered variable arrangement with a pressure-based scheme is used for solving the governing equations. Finite differencing is used for discretization of the filtered Navier–Stokes equations. In the following sections, the governing equations, numerical schemes, subgrid models and solution methodology are described in detail.

3.1 Governing Equations

The motion of a constant density fluid is governed by the incompressible Navier-Stokes equations. Direct numerical simulations (DNS) are the only means of solving these equations exactly. However, for complex flows, the present day computing facilities are not enough to obtain solutions in a reasonable time. Large eddy simulations (LES) are a methodology where solutions are obtained on a coarse grid (compared to DNS). Thus the underlying philosophy of LES is to compute only the important, large-scale motions of the flow and model the effect of the small scale motions on the evolution of the large scales. In order to separate the large scales from the small scales, a filtering operation is performed. Filtering is represented mathematically in physical space as a convolution operation. The resolved (filtered) part denoted by $\overline{f}(x_i)$ is defined by the relation,

$$\overline{f}(x_i) = \int_D f(\xi_i) G(x_i - \xi_i; \overline{\Delta}) d\xi_i$$

where f is a generic variable, and convolution kernel G is a filter function associated with the cut-off scales in space $\overline{\Delta}$ and satisfies the property $\int_{-\infty}^{+\infty} G(x_i; \overline{\Delta}) dx_i = 1$. The space vectors are represented by x_i and ξ_i, and D represents the entire domain. The following properties also hold for the filtering operation:

  1. $f(x_i) = \overline{f}(x_i) + f''(x_i)$

2. $\overline{cf(x_i)} = c\overline{f}(x_i)$, where c is a constant

3. $\overline{f(x_i) + g(x_i)} = \overline{f}(x_i) + \overline{g}(x_i)$

4. $\overline{f''}(x_i) \neq 0$

5. $\overline{\overline{f}}(x_i) \neq \overline{f}(x_i)$

6. $\overline{\frac{\partial f(x_i)}{\partial x}} = \frac{\partial \overline{f}(x_i)}{\partial x}$

Some common filters (G) are,

1. Top-hat or box filter: $G(x_i, \overline{\Delta}_i) = \begin{cases} 1/\overline{\Delta}_i & : \quad |x| \leq \overline{\Delta}_i/2 \\ \\ 0 & : \quad \text{otherwise} \end{cases}$

2. Gaussian filter: $G(x_i, \overline{\Delta}_i) = \sqrt{\frac{6}{\pi\overline{\Delta}_i}}^3 \exp\left(\frac{-6x_i^2}{\overline{\Delta}_i^2}\right)$

3. Cut-off filter: $G(x_i, \overline{\Delta}_i) = 2\left(\frac{\sin(\pi x_i/\overline{\Delta}_i)}{\pi x_i}\right)$

Applying the filter to the Navier–Stokes equations yields a non-dimensional filtered set of equations given by,

$$\frac{\partial \overline{u}_i}{\partial x_i} = 0 \tag{3.1}$$

$$\frac{\partial \overline{u}_i}{\partial t} + \frac{\partial \overline{u}_i \overline{u}_j}{\partial x_j} = -\frac{\partial \overline{p}}{\partial x_i} + \frac{1}{Re}\frac{\partial}{\partial x_j}\left(\frac{\partial \overline{u}_i}{\partial x_j}\right) - \frac{\partial \tau_{ij}}{\partial x_j} \tag{3.2}$$

where the turbulent subgrid scale stress (SGS) tensor that requires modeling is given by,

$$\tau_{ij} = \overline{u_i u_j} - \overline{u}_i \overline{u}_j$$

and t represents time, $\overline{u}_i$ is the filtered velocity field, $\overline{p}$ is the pressure and Re is the Reynolds number.

3.2 Numerical Solution: Finite difference methods

3.2.1 Variable arrangement

A key issue during discretization is to select points in the domain at which the values of the unknown dependent primitive variables are to be computed. In literature, three such arrangements are found, and will be discussed next.
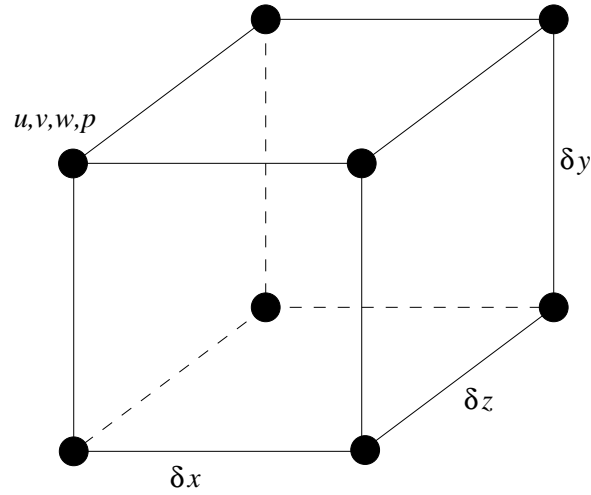
Figure 3.1   Non-staggered primitive variable arrangement for a grid cell defined at each node. δx, δy and δz are the grid point displacements along x, y and z directions, respectively.

3.2.1.1   Non-staggered arrangement

The non-staggered grid arrangement (Chorin, 1967), defines both pressure and velocities at the grid nodes (Fig. 3.1). The non-staggered arrangement has advantages because of its simplicity and the fact that velocity is defined on the boundary where it is generally prescribed. This arrangement has advantages in complex geometries and situations where unstructured grids are often used. However, the main disadvantage of a non-staggered grid arrangement is that pressure is also defined on the boundary. The resulting discretized system of equations for a node has no direct coupling between the pressure and velocities, resulting in what is known as odd-even splitting. Non-staggered central difference schemes are known to suffer because of pressure-velocity decoupling, which make the schemes unstable especially for high Reynolds number turbulent flows (Patankar, 1980). To prevent spurious pressure fluctuations, a remedy is to introduce "artificial diffusion" which provides a stable solution (Sotiropoulos et al. 1991). This method requires the specification of ad-hoc constants which determine the amount of extra diffusion introduced.
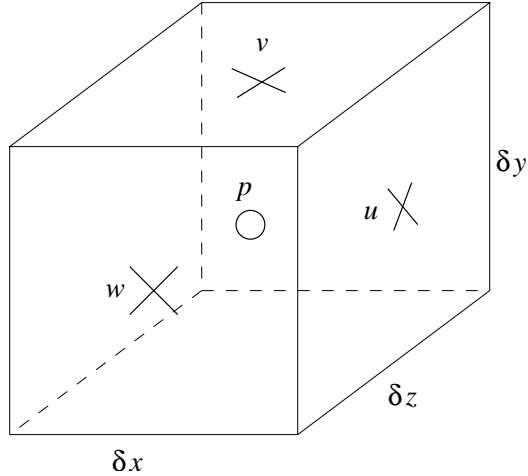
Figure 3.2   Complete staggered arrangement where velocities are defined at the cell face centers and pressure is defined at the cell volume center.

3.2.1.2   Complete Staggered Arrangement

The staggered grid arrangement (Fig. 3.2) introduced by Harlow and Welch (1965) offers advantages over the non-staggered arrangement. For a staggered grid, velocities are defined at the cell faces, while pressure is defined at the cell center. The biggest advantage of the staggered arrangement is the strong coupling between the velocities and pressure, which alleviates convergence problems and oscillations in the pressure and velocity fields (Patankar, 1980). On the other hand, a disadvantage of this arrangement is that only one of the velocity components is defined on each side of the domain boundary. Hence it is necessary to employ ghost cells outside the domain to enforce boundary conditions.

3.2.1.3   Partial Staggered Arrangement

A partial staggered arrangement (Fortin et al. 1971) defines velocities at the grid nodes (Fig. 3.3) similar to the non-staggered arrangement while pressure is staggered to the cell center. The grid points are displaced by δx, δy and δz in the x, y and z directions respectively. The arrangement has the advantage that pressure is staggered with respect to velocity and the pressure-velocity decoupling is avoided (as in the completely staggered case). Moreover, the domain passes through all the velocity points (as in the non-staggered case) and hence no ghost
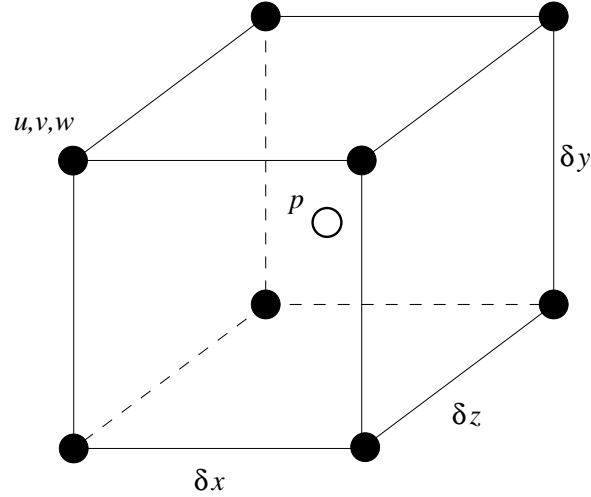
Figure 3.3   Partial staggered arrangement in which velocities are defined at
the grid nodes and pressure is defined at the cell center.

cells are required outside the domain.

3.2.1.4   Selection of grid variable arrangement

Numerical simulations were performed using the non-staggered and the partial staggered arrangements to compare the stability of the two configurations. The divergence of the velocity field ($\nabla \cdot \mathbf{u}$) gives an indication if the incompressibility constraint is satisfied by a particular numerical scheme and this criterion was used to compare the two arrangements. Two-dimensional Poiseuille flow (200×48 cells) and three-dimensional duct flow simulations ($200 \times 48 \times 48$ cells), for which analytical solutions exist, were performed. The order of $\nabla \cdot \mathbf{u}$ on the non-staggered grid was 10^{-4}, whereas, on the partial staggered grid a value of 10^{-5} was obtained. Thus for a simple laminar flow, an order difference in magnitude was observed for the divergence of the velocity field. Moreover, the simulation on the non-staggered grid led to an instability in the solution due to the decoupled nature of the variable arrangement. The cause of decoupling is illustrated next.

On the non-staggered grid, the pressure gradient using a central–difference formulation has the form

$$\frac{\partial \overline{p}_m^n}{\partial x} = \frac{\overline{p}_{m+1}^n - \overline{p}_{m-1}^n}{2\delta x}$$

where m represents a grid index and n is the time level. The Laplacian operator can be written

as:

$$
\begin{aligned}
\frac{\partial}{\partial x}\frac{\partial \overline{p}_m^n}{\partial x} &= \frac{\partial}{\partial x}\left(\frac{\overline{p}_{m+1}^n - \overline{p}_{m-1}^n}{2\delta x}\right) \\
&= \frac{\partial \overline{p}_{m+1}^n/\partial x - \partial \overline{p}_{m-1}^n/\partial x}{2\delta x} \\
&= \frac{\left(\overline{p}_{m+2}^n - \overline{p}_m^n\right)/2\delta x - \left(\overline{p}_m^n - \overline{p}_{m-2}^n\right)/2\delta x}{2\delta x} \\
&= \frac{\overline{p}_{m+2}^n - 2\overline{p}_m^n + \overline{p}_{m-2}^n}{(2\delta x)^2}
\end{aligned}
\tag{3.3}
$$

However, directly discretizing the Laplacian of pressure using a second–order central difference scheme has the form:

$$
\frac{\partial^2 \overline{p}_m^n}{\partial x^2} = \frac{\overline{p}_{m+1}^n - 2\overline{p}_m^n + \overline{p}_{m-1}^n}{(\delta x)^2}
\tag{3.4}
$$

which is not consistent with Eqn. (3.3). If the disretization represented by Eqn. (3.4) is used, $\nabla \cdot \mathbf{u}$ is not satisfied. If instead, Eqn. (3.3) is used to represent the Laplacian of pressure, the formulation leads to pressure–velocity decoupling. The splitting is caused by the fact that the numerator of Eqn. (3.3) requires discrete pressure values at locations relative to $\overline{p}_m$ separated by $2\delta x$, causing the pressure solution to oscillate. In contrast, Eqn. (3.4) only uses adjacent pressure values at δx. To prevent odd–even splitting, some form of dissipation is added, e.g. (Sotiropoulos et al. 1991),

$$
\frac{\partial}{\partial x}\frac{\partial \overline{p}_m^n}{\partial x} = \frac{\overline{p}_{m+2}^n - 2\overline{p}_m^n + \overline{p}_{m-2}^n}{4(\delta x)^2} - \frac{\epsilon}{4}(\delta x)^2\frac{\partial^4 \overline{p}_m^n}{\partial x^4}
$$

where ϵ is a constant whose value lies between 0 and 1. A value of 0 gives the discretized Eqn. (3.3) whereas a value of 1 gives the form shown in Eqn. (3.4). The present study is intended for LES, therefore artificially introducing numerical dissipation must be avoided. Thus, a partial staggered grid is adopted in this study, and a description of the arrangement is presented next.

A two-dimensional schematic is shown in Fig. 3.4 representing index notation on a partially staggered grid. The velocities are represented by filled circles and pressure by hollow circles. The subscripts for pressure indicate that they are displaced $\frac{1}{2}\delta x$ from the velocity nodes. Unlike the non-staggered approach, the divergence and gradient operators on u and p, respectively, for the partially staggered scheme are defined differently. The divergence operator is defined at the cell center $(m + 1/2)$, while the gradient operator is defined at the cell face (m). The discrete
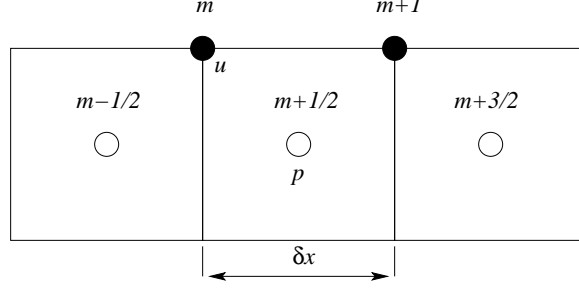
Figure 3.4 Index notation for the variables on partially staggered grid.

forms of the divergence of velocity and the pressure gradient are shown for time level n:

$$\left.\frac{\partial \overline{u}^n}{\partial x}\right|_{m+1/2} = \frac{\overline{u}^n_{m+1} - \overline{u}^n_m}{2\left(\delta x/2\right)}$$

$$\left.\frac{\partial \overline{p}^n}{\partial x}\right|_m = \frac{\overline{p}^n_{m+1/2} - \overline{p}^n_{m-1/2}}{2\left(\delta x/2\right)}$$

The Laplacian of pressure at $m + 1/2$ can then be expanded as follows:

$$
\begin{aligned}
\left.\frac{\partial}{\partial x}\frac{\partial \overline{p}^n}{\partial x}\right|_{m+1/2} &= \frac{\partial \overline{p}^n/\partial x|_{m+1} - \partial \overline{p}^n/\partial x|_m}{(2\delta x/2)}\\
&= \frac{\left(\overline{p}^n_{m+3/2} - \overline{p}^n_{m+1/2}\right)/(2\delta x/2) - \left(\overline{p}^n_{m+1/2} - \overline{p}^n_{m-1/2}\right)/(2\delta x/2)}{(2\delta x/2)}\\
&= \frac{\overline{p}^n_{m+3/2} - 2\overline{p}^n_{m+1/2} + \overline{p}^n_{m-1/2}}{(\delta x)^2}
\end{aligned}
$$

This discretization of the Laplacian operator is consistent with that of the discrete pressure gradient and divergence operator, and thus eliminates the odd-even splitting of the pressure solution. On the partial staggered grid, the pressure gradients obtained on the cell faces have to be interpolated back on to the grid points, leading to an added computational effort. First-order interpolations are used for the purpose.

3.2.2 Spatial and temporal discretizations

LES models are dissipative in nature, hence, it is important to use non-dissipative discretization schemes. For the spatial discretizations shown in this section, only one direction will be shown for simplicity (subscript represents grid index m).

3.2.2.1 Second-order central difference scheme

The first- and second-order derivatives for a general function $f(x)$ are, respectively,

$$\frac{\partial f_m}{\partial x} = f'_m = \frac{f_{m+1} - f_{m-1}}{2\delta x}$$

$$\frac{\partial^2 f_m}{\partial x^2} = f''_m = \frac{f_{m+1} - 2f_m + f_{m-1}}{(\delta x)^2}$$

At the boundaries, one-sided approximations are used with second-order accuracy. For example at a left boundary,

$$f'_m = \frac{-3f_m + 4f_{m+1} - f_{m+2}}{2\delta x}$$

$$f''_m = \frac{2f_m - 5f_{m+1} + 4f_{m+2} - f_{m+3}}{(\delta x)^2}$$

3.2.2.2 Sixth-order compact scheme

A higher-order scheme can resolve a larger range of wave numbers as compared to a second-order scheme on the same grid. In other words, a higher-order scheme requires fewer grid points to resolve the same scales. A sixth-order low dispersive scheme proposed by Lele (1992) is used here. The approximation for a first-order derivative is

$$f'_m + \alpha(f'_{m+1} + f'_{m-1}) = \frac{a}{2\delta x}(f_{m+1} - f_{m-1}) + \frac{b}{4\delta x}(f_{m+2} - f_{m-2})$$

with the constraint $a + 2^4 b = \frac{5!}{4!}(2\alpha)$ and $\alpha = 1/3$, $a = \frac{1}{3}(4 + 2\alpha)$, $b = \frac{1}{3}(4\alpha - 1)$. The formulation is sixth-order accurate at the internal nodes. At the boundaries however, the accuracy is reduced, where

$$f'_m + \alpha f'_{m+1} = \frac{1}{\delta x}(af_m + bf_{m+1} + cf_{m+2})$$

with $\alpha = 2$, $a = -5/2$, $b = 2$ and $c = 1/2$. The scheme is third-order accurate at the boundary and fourth-order accurate at points adjacent to the boundary.

The approximation of a second-order derivative is

$$f''_m + \alpha(f''_{m+1} + f''_{m-1}) = \frac{a}{(\delta x)^2}(f_{m+1} - 2f_m + f_{m-1}) + \frac{b}{4(\delta x)^2}(f_{m+2} - 2f_m + f_{m-2})$$

with the constraint $a + 2^4 b = \frac{6!}{4!}\alpha$ and $\alpha = 2/11$, $a = \frac{4}{3}(1 - \alpha)$, $b = \frac{1}{3}(10\alpha - 1)$ for sixth-order accuracy. At boundaries,

$$f''_m + \alpha f''_{m+1} = \frac{1}{(\delta x)^2}(af_m + bf_{m+1} + cf_{m+2} + df_{m+3})$$

with $\alpha = 11$, $a = 13$, $b = -27$ and $c = 15$ and $d = -1$. These schemes are computationally expensive and a matrix inversion (of a tridiagonal matrix) is required to calculate the derivatives. A Thomas algorithm is used to invert the matrix.

3.2.2.3 Time integration

A compact third-order Runge–Kutta method is used to march the solution in time (Wray, 1990). The compact scheme requires minimum storage during a simulation. For the ordinary differential equation, $dx/dt = f(x, t)$, the four stages are

$$
\begin{aligned}
x^* &= x^n + \frac{1}{4} f\left(x^n, t^n\right) \delta_t^n \\
x^{**} &= x^n + \frac{8}{15} f\left(x^n, t^n\right) \delta_t^n \\
x^{***} &= x^* + \frac{5}{12} f\left(x^{**}, t^{**}\right) \delta_t^n \\
x^{n+1} &= x^* + \frac{3}{4} f\left(x^{***}, t^{***}\right) \delta_t^n
\end{aligned}
$$

with

$$
\begin{aligned}
t^* &= t^n + \frac{1}{4} \delta_t^n \\
t^{**} &= t^n + \frac{8}{15} \delta_t^n \\
t^{***} &= t^n + \frac{2}{3} \delta_t^n \\
t^{n+1} &= t^n + \delta_t^n
\end{aligned}
$$

3.2.3 Numerical solution and the pressure Poisson equation

Beginning with the initial conditions, an elliptic pressure Poisson equation is obtained by decoupling pressure from the momentum equations (Harlow and Welch, 1965). Equation (3.2) can be rewritten as,

$$
\frac{\partial \overline{u}_i}{\partial t} = -\frac{\partial \overline{p}}{\partial x_i} + \mathcal{F}_i
$$

where $\mathcal{F}_i$ represents the filtered convective, viscous and SGS stress terms. Discretizing the time term (one step of the Runge–Kutta scheme),

$$
\frac{\overline{u}_i^{n+1} - \overline{u}_i^n}{\delta t} = -\frac{\partial \overline{p}^n}{\partial x_i} + \mathcal{F}_i^n \tag{3.5}
$$

where n and $n + 1$ are the current and next time levels, respectively, and δt is the time step. The continuity condition is enforced at $n + 1$, whereby:

$$\frac{\partial \overline{u}_i^{n+1}}{\partial x_i} = 0 \qquad (3.6)$$

and maintains incompressibility at time level $n + 1$. Now taking the divergence of Eqn. (3.5) and using Eqn. (3.6), the pressure Poisson equation is obtained,

$$\frac{\partial}{\partial x_i} \frac{\partial \overline{p}^n}{\partial x_i} = \frac{\partial}{\partial x_i} \left[\frac{\overline{u}_i^n}{\delta t} + \mathcal{F}_i^n \right] \qquad (3.7)$$

The pressure solution of the Poisson equation ensures that incompressibility is maintained from time n to $n + 1$. Once pressure is known, the velocity field at $n + 1$ can be computed from Eqn. (3.5). Note that this formulation follows that of Harlow and Welch (1965) and obviates the need for intermediate boundary conditions necessary in the fractional-step method (Kim and Moin, 1985). The pressure solution is obtained using an iterative solver and is discussed later in chapter 4. Since explicit methods are used to discretize the equations, time-step restrictions based on the CFL (convective scale) and Von-Neumann (diffusive scale) criteria must be followed.

3.2.4 Comments on filter commutation

Near boundaries, a non-uniform mesh is used in order to reduce grid resolution (as compared to using a uniform mesh throughout the domain). A mapping function based on a Jacobian transformation is then used to obtain the spatial derivatives on the non-uniform mesh. It is known that on a non-uniform mesh, the filtering operation does not commute, i.e. $\overline{\partial u / \partial x} \neq \partial \overline{u} / \partial x$ and the error can be quantified as (Ghosal, 1996),

$$\overline{\frac{\partial u}{\partial x}} = \frac{\partial \overline{u}}{\partial x} - \alpha \overline{\Delta}^2 \left(\frac{\overline{\Delta}'}{\overline{\Delta}} \right) \frac{\partial^2 \overline{u}}{\partial x^2} + O \left(\overline{\Delta} \right)^4$$

where $\alpha = \int \zeta^2 G(\zeta) d\zeta$. The pressure Poisson discretization is second-order, irrespective of the scheme used for convection and diffusion terms, and the overall accuracy of the solution is second-order. Therefore, the finite difference error is on the same order as the commutation error and can be ignored. In general, for higher-order schemes, the second-order derivative term must be included (Ghosal et al., 1995). Another way to avoid the commutation error

is to use high-order filters. High-order discrete filters have been constructed, which have zero lower-order moments, e.g. $\alpha = 0$ on the non-uniform mesh (Vasilyev et al. 1998).

3.2.5 Boundary conditions

The velocity points are defined on the domain boundary, hence no-slip conditions can be directly enforced. For an inflow boundary, a known velocity field can be prescribed. For an outflow boundary, a convective outflow boundary condition is used (Ferziger and Perić, 2002):

$$\frac{\partial u_i}{\partial t} + \mathcal{U}\frac{\partial u_i}{\partial x_i} = 0$$

where $\mathcal{U}$ is a constant velocity calculated from the inflow, so as to conserve the mass flow rate. For the pressure Poisson equation, at the inflow boundary and on the no-slip walls, a zero normal pressure gradient is specified, $\partial \overline{p}/\partial n = 0$, and at the outflow boundary zero gage pressure is specified. For the inflow boundary , generally, the velocity is prescribed. For simulations of the rectangular jet, a special technique is used to mimic the experimental conditions. Details of the procedure are given in chapter 5.

3.3   Subgrid stress models

In this section, the subgrid stress models that will be used for the rectangular jet application are described.

3.3.1 Smagorinsky model

The Smagorinsky model is an eddy-viscosity type model, which represents the effect of the subgrid scales purely as an enhanced diffusivity for the large-scale flow (Smagorinsky, 1963). The SGS stress tensor is modeled as,

$$\tau_{ij} - \frac{1}{3}\tau_{kk}\delta_{ij} = -2\nu_t\overline{S}_{ij}$$

where ν_t is the turbulent eddy-viscosity, δ_{ij} is the Kronecker delta function, and the filtered rate of the deformation tensor is

$$\overline{S}_{ij} = \frac{1}{2}\left(\frac{\partial \overline{u}_i}{\partial x_j} + \frac{\partial \overline{u}_j}{\partial x_i}\right)$$

The turbulent eddy-viscosity is parameterized by equating the subgrid scale energy production and dissipation to obtain

$$\nu_t = \left(C_s \overline{\Delta}\right)^2 |\overline{S}|$$

where,

$$|\overline{S}| = \sqrt{2\overline{S}_{ij}\overline{S}_{ij}}$$

and C_s is the Smagorinsky coefficient to be specified. The effective filter width $\overline{\Delta}$ is a function of the grid resolution and is defined as $\overline{\Delta} = (\Delta_1 \Delta_2 \Delta_3)^{1/3}$, where Δ_1, Δ_2 and Δ_3 represent the filter widths in x, y and z directions, respectively. For near wall regions, a damping function is applied (van Driest, 1956) to decrease the eddy viscosity.

The dynamic model (Germano et al. 1991) differs from the Smagorinsky model in that the model constant C_s is calculated "dynamically" using information from two different length scales already part of the resolved solution. The procedure is generic and can be applied to any model. The coefficient C_s is a function of space and time and has been shown to be compatible with the local flow physics. Also, with the dynamic model, the eddy-viscosity asymptotically approaches zero near solid walls and in regimes where the flow is laminar. The model however requires a new filtering operation to be performed within a test filter volume, where the test filter width $\widehat{\Delta}$ is assumed to be greater than the grid filter width $\overline{\Delta}$. An overbar, '⁻' denotes grid filtering (subgrid scales) and a caret, '^' denotes test filtering (sub–test scales). For the test-filter operation, a Gaussian filter is used, represented by,

$$G(x_i - \xi_i) = \left[\frac{\sqrt{6/\pi}}{\widehat{\Delta}}\right]^3 \exp\left(-\left[\frac{\sqrt{6}}{\widehat{\Delta}}\right]^3 (x_i - \xi_i)^2\right)$$

Applying the test filter to the Navier–Stokes equations (Eqns. 3.2), the sub–test scale stress tensor, T_{ij}, is obtained as:

$$T_{ij} = \widehat{\overline{u_i u_j}} - \widehat{\overline{u}}_i \widehat{\overline{u}}_j$$

The quantities τ_{ij} and T_{ij} are related by the following identity given by Germano (Germano et al. 1991),

$$L_{ij} = T_{ij} - \widehat{\tau}_{ij} = \widehat{\overline{u_i u_j}} - \widehat{\overline{u}}_i \widehat{\overline{u}}_j$$

where L_{ij} is the resolved turbulent stress that can be explicitly calculated. The term T_{ij} is also modeled similar to the subgrid scale turbulent stress τ_{ij} using the Smagorinsky model with the same model constant C_s,

$$\tau_{ij} - \frac{1}{3}\tau_{kk}\delta_{ij} = -2C_s^2\overline{\Delta}^2|\overline{S}|\overline{S}_{ij}$$

$$T_{ij} - \frac{1}{3}T_{kk}\delta_{ij} = -2C_s^2\widehat{\Delta}^2|\widehat{\overline{S}}|\widehat{\overline{S}}_{ij}$$

$$L_{ij} - \frac{1}{3}L_{kk}\delta_{ij} = C_s^2 M_{ij}$$

where

$$M_{ij} = 2\overline{\Delta}^2\left(\widehat{|\overline{S}|\overline{S}_{ij}} - \frac{\widehat{\Delta}^2}{\overline{\Delta}^2}|\widehat{\overline{S}}|\widehat{\overline{S}}_{ij}\right)$$

Using a least squares approach (Lilly, 1992), the coefficient C_s^2 is evaluated as

$$C_s^2 = \frac{\langle L_{ij}M_{ij}\rangle}{\langle M_{ij}M_{ij}\rangle} \tag{3.8}$$

where angled brackets denote averaging over the test filter volume.

3.3.2 Scale dependent dynamic Smagorinsky model

An assumption or simplification in the dynamic model is that the model coefficient is scale invariant ($C_s(\overline{\Delta}) = C_s(\widehat{\Delta})$). For certain applications, e.g., in atmospheric boundary layer flows, near the boundary the scales are outside the inertial range and the invariance is broken. Portè-Agel et al. (2000) proposed a scale dependent model in which a new unknown $\beta = C_s^2(\widehat{\Delta})/C_s^2(\overline{\Delta})$ is introduced, and to solve for β, a second-test filtering operation is performed at the scale $\widetilde{\Delta} = 4\overline{\Delta}$. The Germano identity between scales $\overline{\Delta}$ and $\widetilde{\Delta}$ can be written as,

$$Q_{ij} - \frac{1}{3}Q_{kk}\delta_{ij} = C_s^2 N_{ij}$$

where

$$Q_{ij} = \widetilde{\overline{u_i}\overline{u}_j} - \widetilde{\overline{u}}_i\widetilde{\overline{u}}_j$$

and

$$N_{ij} = 2\overline{\Delta}^2\left(\widetilde{|\overline{S}|\overline{S}_{ij}} - \frac{\widetilde{\Delta}^2}{\overline{\Delta}^2}|\widetilde{\overline{S}}|\widetilde{\overline{S}}_{ij}\right)$$

Using least squares procedure as before, yields another equation for C_s^2,

$$C_s^2 = \frac{\langle Q_{ij}N_{ij}\rangle}{\langle N_{ij}N_{ij}\rangle} \tag{3.9}$$

Since Eqns. 3.8 and 3.9 represent the same variable, equating them results in the equation,

$$\langle L_{ij}M_{ij}\rangle\langle N_{ij}N_{ij}\rangle - \langle Q_{ij}N_{ij}\rangle\langle M_{ij}M_{ij}\rangle = 0 \tag{3.10}$$

The terms in Eq. 3.10 are given by,

$$\langle L_{ij}M_{ij}\rangle = a_1\beta - b_1$$

$$\langle M_{ij}M_{ij}\rangle = c_1 + d_1\beta^2 - e_1\beta$$

$$\langle Q_{ij}N_{ij}\rangle = a_2\theta - b_2$$

$$\langle N_{ij}N_{ij}\rangle = c_2 + d_2\theta^2 - e_2\theta$$

where

$$a_1 = -2\overline{\Delta}^2 4\langle|\widehat{\overline{S}}|\widehat{\overline{S}}_{ij}L_{ij}\rangle$$

$$b_1 = -2\overline{\Delta}^2 \langle\widehat{|\overline{S}|\overline{S}}_{ij}L_{ij}\rangle$$

$$c_1 = \left(2\overline{\Delta}^2\right)^2 \langle\widehat{|\overline{S}|\overline{S}}_{ij}\widehat{|\overline{S}|\overline{S}}_{ij}\rangle$$

$$d_1 = \left(2\overline{\Delta}^2\right)^2 (4)^2 \langle|\widehat{\overline{S}}|^2\widehat{\overline{S}}_{ij}\widehat{\overline{S}}_{ij}\rangle$$

$$e_1 = 2\left(2\overline{\Delta}^2\right)^2 4\langle|\widehat{\overline{S}}|\widehat{\overline{S}}_{ij}\widehat{|\overline{S}|\overline{S}}_{ij}\rangle$$

$$a_2 = -2\overline{\Delta}^2 4^2 \langle|\widetilde{\overline{S}}|\widetilde{\overline{S}}_{ij}Q_{ij}\rangle$$

$$b_2 = -2\overline{\Delta}^2 \langle\widetilde{|\overline{S}|\overline{S}}_{ij}Q_{ij}\rangle$$

$$c_2 = \left(2\overline{\Delta}^2\right)^2 \langle\widetilde{|\overline{S}|\overline{S}}_{ij}\widetilde{|\overline{S}|\overline{S}}_{ij}\rangle$$

$$d_2 = \left(2\overline{\Delta}^2\right)^2 (4^2)^2 \langle|\widetilde{\overline{S}}|^2\widetilde{\overline{S}}_{ij}\widetilde{\overline{S}}_{ij}\rangle$$

$$e_2 = 2\left(2\overline{\Delta}^2\right)^2 (4)^2 \langle|\widetilde{\overline{S}}|\widetilde{\overline{S}}_{ij}\widetilde{|\overline{S}|\overline{S}}_{ij}\rangle$$

where $\beta = C_s^2(\widehat{\Delta})/C_s^2(\overline{\Delta})$ and $\theta = C_s^2(\widetilde{\Delta})/C_s^2(\overline{\Delta})$. A power law behavior is assumed for C_s over the range between scales $\overline{\Delta}$ and $\widetilde{\Delta}$. Therefore, $C_s^2(2\overline{\Delta})/C_s^2(\overline{\Delta}) = C_s^2(4\overline{\Delta})/C_s^2(2\overline{\Delta}) = \beta$, and, $\theta = C_s^2(4\overline{\Delta})/C_s^2(\overline{\Delta}) = \beta^2$. Substituting these relations into Eqn. 3.10 gives the form:

$$A_0 + A_1\beta + A_2\beta^2 + A_3\beta^3 + A_4\beta^4 + A_5\beta^5 = 0 \tag{3.11}$$

where,

$$A_0 = b_2 c_1 - b_1 c_2$$

$$A_1 = a_1 c_2 - b_2 e_1$$

$$A_2 = b_2 d_1 + b_1 e_2 - a_2 c_1$$

$$A_3 = a_2 e_1 - a_1 e_2$$

$$A_4 = -a_2 d_1 - b_1 d_2$$

$$A_5 = a_1 d_2$$

Eqn. (3.11) has five roots of which only the largest positive root is meaningful and chosen as the solution. For the standard dynamic Smagorinsky model, $\beta = 1$. Using the scale dependent dynamic model, values of β less than 1 in the boundary layer are obtained (Porté–Agel et al., 2000).

3.3.3 Structure function model

The structure function model was originally formulated in spectral space and then applied to physical space (Mètais and Lesieur, 1992). The eddy-viscosity is based on the local kinetic energy spectrum, calculated in terms of the second-order velocity structure function of the filtered field and takes into account the local intermittency of turbulence. The second-order structure function is evaluated in physical space as (Lesieur and Métais, 1996),

$$F_2(\mathbf{x},\overline{\Delta},t) = \frac{1}{6}\sum_{i=1}^{3}\left[||\overline{\mathbf{u}}(\mathbf{x},t) - \overline{\mathbf{u}}(\mathbf{x}+\Delta x_i \mathbf{e}_i, t)||^2 + ||\overline{\mathbf{u}}(\mathbf{x},t) - \overline{\mathbf{u}}(\mathbf{x}-\Delta x_i \mathbf{e}_i, t)||^2\right]\left(\frac{\overline{\Delta}}{\Delta x_i}\right)^{2/3}$$

where, $\overline{\mathbf{u}}$ and $\mathbf{x}$ represent the velocity and displacement vectors. The eddy-viscosity is given by,

$$\nu_t = 0.105\, C_K^{-3/2}\, \overline{\Delta}\, F_2^{1/2}$$

where $C_K = 1.5$ is the Kolmogorov constant.

3.3.4 One-equation subgrid kinetic energy model

The subgrid kinetic energy is defined as, $k_{sgs} = \frac{1}{2}(\overline{u_i u_i} - \overline{u}_i \overline{u}_i)$, and represents the kinetic energy of the unresolved scales of motion. The k_{sgs} can therefore be used as a velocity scale

in the SGS stress term. However, since there is no direct representation of the unresolved scales in LES, a transport equation is solved. The one-equation subgrid kinetic energy model has shown good results at lower grid resolutions as compared to the dynamic Smagorinsky model (Menon et al. 1996). In this model, no assumption of local equilibrium is made between energy production and dissipation rate. A transport equation can be derived for k_{sgs} from the Navier–Stokes equations which has unclosed terms. The model equation for $k \equiv k_{sgs}$ is given by,

$$\frac{\partial k}{\partial t} + \frac{\partial \overline{u}_i k}{\partial x_i} = -\tau_{ij}\frac{\partial \overline{u}_i}{\partial x_i} + \frac{\partial}{\partial x_i}\left(\nu_t\frac{\partial k}{\partial x_i}\right) - C_\varepsilon\frac{k^{3/2}}{\overline{\Delta}}$$

The terms on the right hand side represent the production, transport and dissipation of the subgrid kinetic energy, respectively. The subgrid stresses τ_{ij} are modeled in terms of the SGS eddy viscosity ν_t as:

$$\tau_{ij} = -2\nu_t\overline{S}_{ij} + \frac{2}{3}k\delta_{ij}$$

where the SGS eddy viscosity $\nu_t = C_k\overline{\Delta}\sqrt{k}$. The variables C_k and C_ε can be chosen as constants or evaluated based on the dynamic procedure.

In the following chapter, validation of the numerics and the subgrid stress model is described. The parallelization of the solver using message passing interface and performance studies on an Iowa State University cluster are demonstrated.

CHAPTER 4.   BENCHMARKING AND PARALLELIZATION

To ascertain the accuracy of the numerical scheme as well as the SGS stress model, benchmark cases are simulated for laminar and turbulent flows using the partial staggered grid. Solutions for lid driven cavity flow and flow over a backward facing step ensures that the scheme is correctly implemented. For testing the LES model, a turbulent channel flow simulation is performed. For high Reynolds number flows where grid resolution requirements increase, multiple processors are used to obtain solutions using message passing interface (MPI). Performance curves are shown upto 256 processors on an AMD Opteron cluster at Iowa State University.

4.1   Lid driven square cavity flow

A square cavity flow driven by a moving lid has been studied extensively in CFD research and is often used as a standard benchmark problem to validate numerical solution algorithms. A two-dimensional schematic is shown in Fig. 4.1. The geometry consists of four planes enclosing a square cavity and the the top plane is moving at a constant velocity U. Momentum is transferred by viscous forces and the flow develops downward, reaching steady state forming a primary recirculation zone. With increasing Reynolds number (defined as $Re = LU/\nu$), secondary recirculation zones appear near the bottom corners of the cavity. The dimension L is chosen as the height of the cavity. Here the results are compared with those obtained by Ghia et al. (1982) and Kim and Moin (1985) at a Reynolds number of 5000. Ghia et al. use the vorticity-stream function approach to solve the Navier–Stokes equations using an implicit multigrid method on a mesh of size 256×256 cells, while Kim et al. use a fractional time-stepping scheme in conjunction with an approximate factorization technique to solve the problem on a mesh of size 96×96 cells. The grid size used in this work is also 96×96 cells. Figure 4.2 shows $u-$ and $v-$ velocity profiles along the vertical and horizontal centerlines of the cavity,

respectively. The current simulations deviate from that of Ghia et al. only near the cavity walls and this is due to a lower resolution of the present simulation. The non-dimensional vorticity at the center of the primary vortex is -1.821 (refer to Fig. 4.3) and is in close agreement with the values obtained by Ghia et al. (-1.860) and Kim and Moin (-1.812).

Extensions of two-dimensional driven cavity flows were conducted to study Taylor–Görtler vortex structures that are found in three-dimensional cavity flow experiments by Koseff et al. (1982). Koseff et al., however, failed to reproduce this three-dimensional structure in their numerical simulations. Kim and Moin (1985) were able to capture the longitudinal Taylor–Görtler vortex structures in their simulations (for Reynolds numbers greater than 900) and benchmark this case as a test for their numerical scheme. To check whether the partial staggered scheme is able to capture these vortex structures, a three-dimensional driven cavity simulation was performed on a coarse grid ($32 \times 32 \times 32$ cells) for a Reynolds number of 1500. To initialize the calculation, small random disturbances in the spanwise direction (z) were added. Periodic boundary conditions were used in the spanwise direction. Velocity vectors in a $y - z$ plane through the geometric center ($x = 0.5$) of the cubic cavity are shown in Fig. 4.4. Although no quantitative measurements were reported in their paper, vortex structures similar to those reported by Kim and Moin are observed in the present simulations.

4.2 Flow over a backward facing step

The flow over a backward-facing step in a channel is a good test case for the numerical method because a dissipative scheme will not predict the correct reattachment length of the recirculation zone downstream of the step. A two-dimensional schematic of the backward facing step of height h is shown in Fig. 4.5. The flow expands downstream of the step and reattaches at x_r forming a recirculation zone. A two-dimensional simulation of laminar flow over the step is performed for a Reynolds number of 400. At the inflow boundary, located above the step, a parabolic velocity profile is prescribed. The downstream boundary is located at $x = 30h$ and 256×32 cells are used for the simulation. Figure 4.6 shows velocity vectors in the domain, colored by streamwise velocity contours. Streamlines are also shown and the reattachment length $x_r/h = 8.7$. Kim and Moin (1985) report a reattachment length of 8.6

in their simulations, while experimental results at $Re = 400$ show a reattachment length of 8.4 (Armaly et al. 1983).

4.3   Turbulent channel flow

The driven cavity flow and flow over a backward facing step proved the correctness of the finite difference scheme and the numerical solution procedure. To test the efficacy of the subgrid model on turbulent flow solutions, simulations of flow in a turbulent channel are performed. The turbulent channel flow problem is a standard benchmark case to test turbulence models. Here, the dynamic Smagorinsky model (Lilly, 1992) is tested for the partially staggered formulation, since it does not use any ad-hoc constants. The flow geometry is shown in Fig. 4.7. The channel is bounded only in the normal (y) direction and extends to infinity in x and z. The streamwise (x) and spanwise (z) directions are homogeneous with periodic boundary conditions and the normal direction is bounded by no-slip walls. For the initial condition, analytical expressions for the three velocity components are used for $Re_\tau = 180$ (based on wall stress τ_w) (Kim et al. 1987):

$$
\begin{aligned}
u(x, y, z) &= C(1 - y^8) + \epsilon\, 2\pi\, \sin(\pi y)\cos(x)\sin(z) \\
v(x, y, z) &= -\epsilon(1 + \cos(\pi y))\sin(x)\sin(z) \\
w(x, y, z) &= -\epsilon\, \pi\, \sin(x)\sin(\pi y)\cos(z)
\end{aligned}
$$

where $C = 7.764\, Re_\tau^{1/7}$ is the centerline velocity and $\epsilon = 0.1C$. This initial condition satisfies boundary conditions and is divergence free. Essentially it represents a three-dimensional disturbance superimposed on a two-dimensional mean flow. In addition, a mean streamwise pressure gradient term is added to the streamwise momentum equation ($F\delta_{i1}$). This is required to maintain the mass flow rate in the system to its initial value. The streamwise pressure gradient is adjusted at each time step (Benocci and Pinelli, 1990) to provide the desired mass flow rate as:

$$
F^{n+1} = F^n - \frac{1}{\Delta t}\left[\left(\frac{\dot{m}}{A_c}\right)^0 - 2\left(\frac{\dot{m}}{A_c}\right)^n + \left(\frac{\dot{m}}{A_c}\right)^{n-1}\right]
$$

where $\dot{m}^n$ is the average mass flow rate at time level n, Δt is the physical time step, and A_c is the cross-flow area of the channel. The average mass flow rate is given by:

$$\frac{\dot{m}}{A_c} = \frac{1}{L_y L_z} \int_{-1}^{1} \langle \rho u \rangle_{x,z} \, dy$$

where $\langle \ \rangle_{x,z}$ denotes an ensemble average in the x and z directions. The desired mass flow rate is $\left(\frac{\dot{m}}{A_c} \right)^0$, where 0 indicates the initial mass flow rate in the channel.

The non-dimensional channel dimensions (with respect to channel half-width) are $4\pi \times 2 \times 2\pi$. Uniform grid cells are used in x and z, while stretched grid cells are used in the y-direction. The domain is divided into $96 \times 64 \times 80$ cells in x, y and z directions, respectively. For the subgrid model, the dynamic Smagorinsky model is used with a test filter-to-grid filter ratio of 2.0

The velocity statistics are compared to the DNS results of Kim et al. (1987) and the experimental results of Niederschulte et al. (1990). The DNS study employed about 4×10^6 grid points ($192 \times 129 \times 160$ in x, y, z) and used pseudospectral methods. The experiments of Niederschulte were performed specifically to examine the accuracy of Kim et al.'s DNS results. Good, but not exact agreement was found between the experimental and DNS results. The mean streamwise profile is shown in wall coordinates in Fig. 4.8. The mean profile was obtained by averaging in the homogeneous directions (x and z) and in time. The velocity is normalized by the friction velocity as $u^+ = u/u_\tau$, where $u_\tau = \sqrt{\tau_w/\rho}$. The dashed line and the dash-dot line represent the law of the wall and the log law, respectively. The LES agree well with the DNS and experimental data. A value of $u_\tau = 0.98$ was obtained in the LES calculations making the effective $Re_\tau = 176.4$. The normalized rms velocity fluctuations are shown in Fig. 4.9. The rms velocities are underpredicted, and this is not completely unexpected, since, the LES data represent resolved scale intensities in which the small scale contribution in not included. The Reynolds shear stress is shown in Fig. 4.10 and compares well with the data. In general, the LES results match well with the DNS data, thus providing confidence in the application of the model to other general flows.

4.4   Parallel Computing

As the dimensionality of system and complexity of the problem increases, the need for obtaining quick solutions becomes a priority. Computing time becomes a bottleneck for simulations of turbulent flows that require high grid resolutions. In the present case the computation of pressure is an expensive part of the numerical solution procedure since pressure in the entire domain has to be solved simultaneously due to the nature of the elliptic Poisson equation. The incompressibility condition must be satisfied at every time step, i.e., each stage of the Runge–Kutta time integration scheme, hence, the Poisson equation has to be solved four times in each time step. These factors lead to the necessity of parallel computing.

Message passing interface (MPI) is a programming standard used on parallel computers with distributed memory (Snir et al. 2001). The main idea is to use domain decomposition to break up the geometry into parts such that every processor gets its own share of calculations. A schematic of a simple two-dimensional domain is shown in Fig. 4.11. The geometry is divided such that two processors share the computational domain, each having 16 grid points for its own calculations (small filled circles for processor 0 and small unfilled circles for processor 1). The interprocessor boundary is shown in the figure with a double line. Two layers of grid points (represented by large circles concentric to the small circles) adjacent to the interprocessor boundary represent the points over which communication is required. The MPI library provides routines for communication between processors.

Solutions to the first- and second-order derivatives for the sixth-order compact finite difference scheme are obtained by solving the Thomas algorithm. It is a direct method and the solution is obtained in two steps, forward elimination and backward substitution (Tannehill et al. 1997). Due to the substitution procedures of the algorithm, it is not scalable on a parallel machine. However, since many such forward and backward steps are required along a particular direction (e.g. x-direction) during a calculation, an overlap can be achieved in each stage to reduce the overall computational time. This technique is known as *pipelining*. Details about the procedure can be found in Stoessel et al. (1996). For the second-order central difference schemes, only one layer of cells is required for communication.

To solve the linear system of equations for the Poisson equation on a three-dimensional domain, a hepta-diagonal sparse matrix must be inverted. For this purpose, an efficient parallel program, *Aztec*, developed at the Sandia National Laboratory is coupled with the finite difference solver (Tuminaro et al. 1999). Aztec is an iterative library for solving a system of linear equations and is designed especially for distributed memory parallel machines. It offers a variety of preconditioned Krylov solvers. The bi-conjugate gradient method with stabilization and least squares preconditioning is used for the present calculations. Aztec is coupled with the LES solver such that solutions can be obtained on multiple processors. The input/output (I/O) is performed individually by each processor.

4.5 Parallel performance

The parallel code is tested on an AMD Opteron cluster which has 376 processor cores (94 nodes) with 8 GBytes of memory per node. Each node is a dual processor, dual core 2.4 GHz AMD 280 Opteron with 1 MB on-chip cache. The nodes are interconnected with a high performance InfiniPath HTX communication network for MPI communication and a Gigabit Ethernet switch for I/O. Each test utilized at least 1 hour of CPU time. Due to time limitations per processor on the cluster, the test was divided into two parts: one using 4 to 64 processors and another using 64 to 256 processors. Speed-up on n processors is defined as the ratio of time taken by a single processor calculation to the time taken by the n-processor calculation. For the tests using 4-64 processors, speed-up is based on 4 processors as a reference, and tests using 64-256 processors use a reference of 64 processors. Figures 4.12 and 4.13 show the performance curves, where symbols represent simulation data and the solid line represents the ideal case. Overall, the code performed well on multiple processors, and a few cases show better than ideal or super-linear speed-up, which may be attributed to an efficient cache utilization for those calculations.
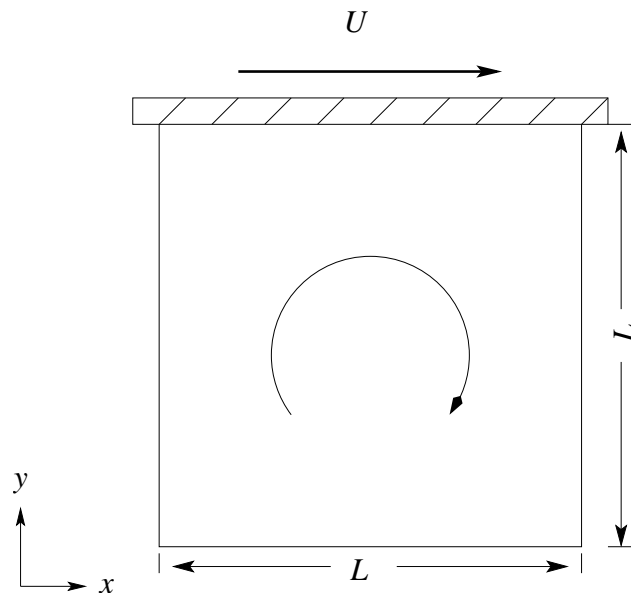
Figure 4.1   Two–dimensional schematic of a lid driven square cavity flow.

(a)
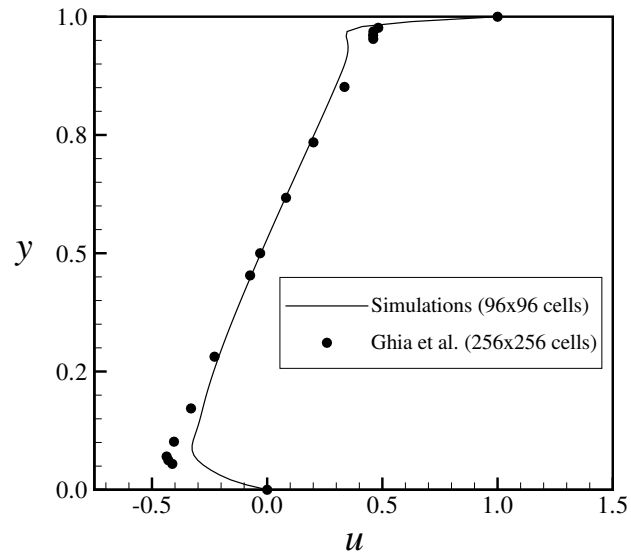
(b)
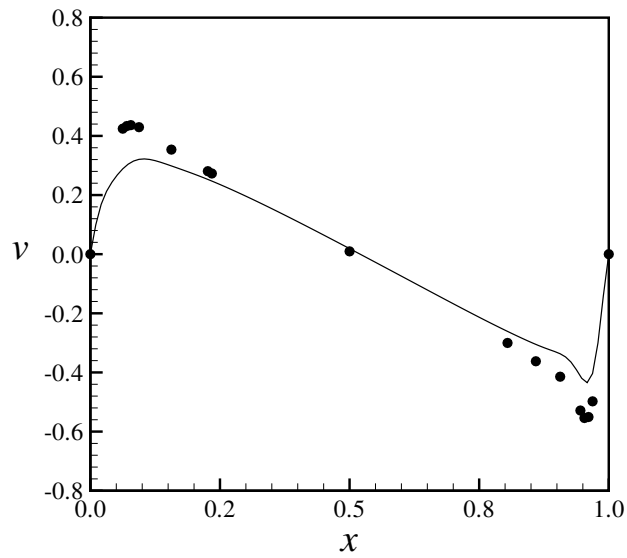
Figure 4.2   Figure shows (a) $u-$ velocity along the vertical centerline and
(b) $v-$ velocity along the horizontal centerline. Lines represent
present work and symbols are results by Ghia et al. (1982).

Figure 4.3   Two–dimensional solution of spanwise vorticity for driven cavity
flow on a square domain with 96×96 cells at $Re = 5000$.

Figure 4.4   Taylor–Görtler vortex structure: Velocity vectors in a $(y - z)$
plane through the geometric center of the cubic cavity $(x = 0.5)$
for three–dimensional driven cavity flow at $Re = 1500$.
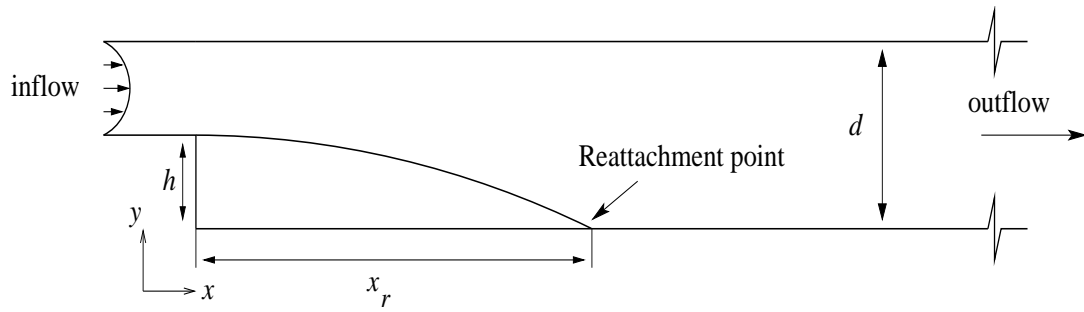
Figure 4.5   Flow over a backward facing step with expansion ratio $d/h = 2$.
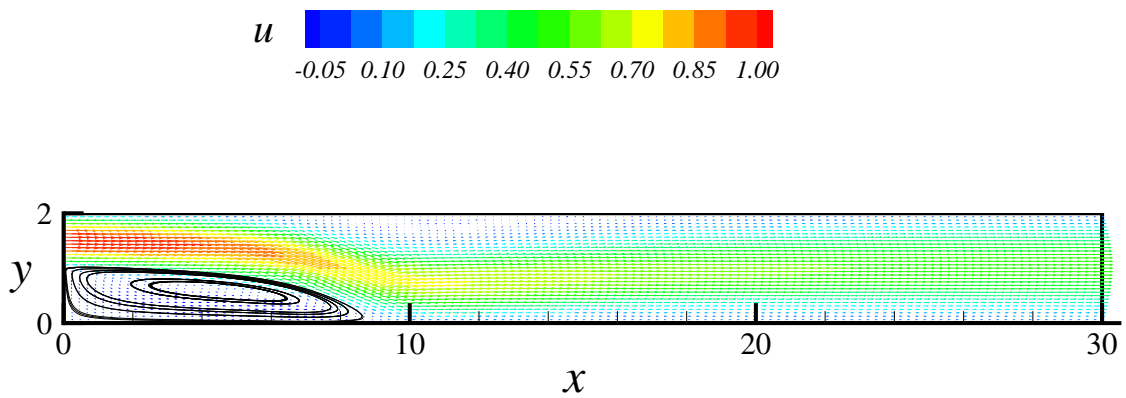
Figure 4.6   Velocity vectors superimposed with $u-$ velocity contours and streamlines at $Re = 400$.
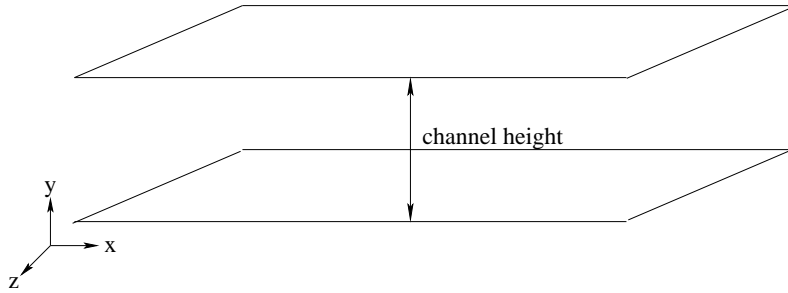
Figure 4.7   Schematic of turbulent channel flow. Walls at the top and bottom extend to infinity in the x and z directions.
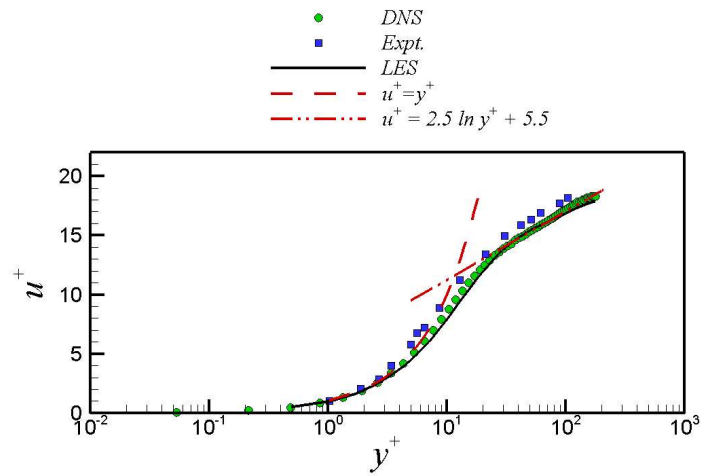
Figure 4.8   Mean streamwise velocity profile in wall coordinates.
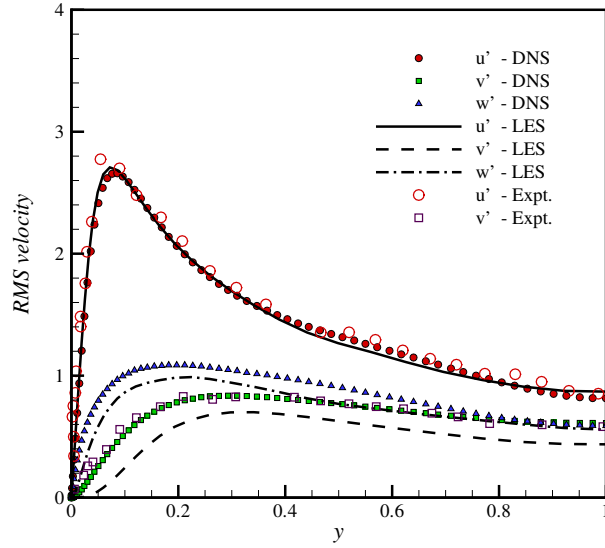
Figure 4.9   Root-mean-square of velocity fluctuations normalized by wall
friction velocity.
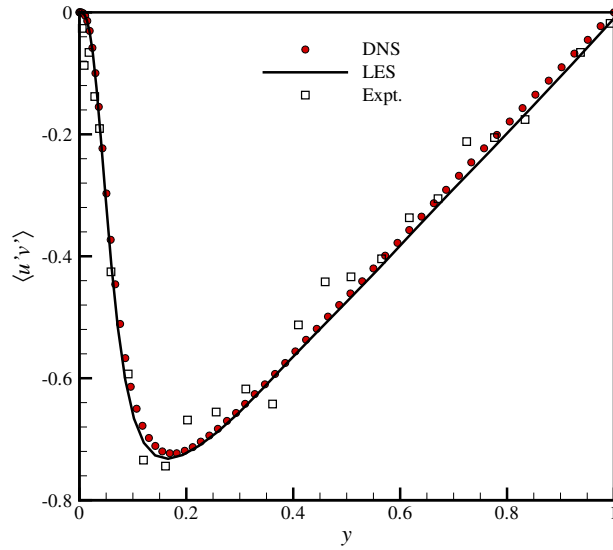
Figure 4.10   Normalized Reynolds shear stress.
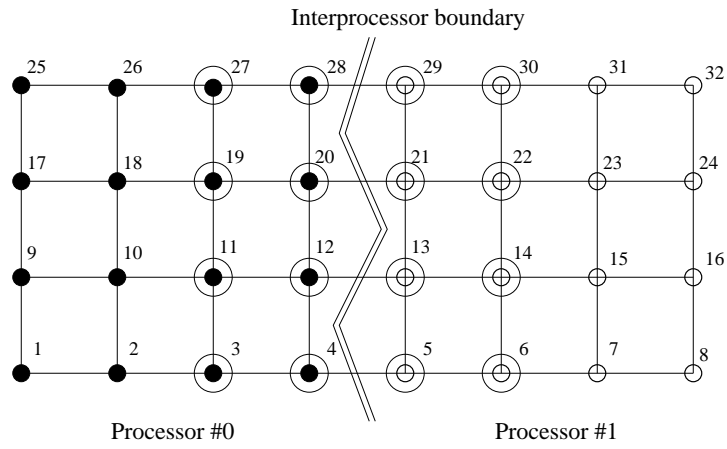
Figure 4.11   Partitioning of a finite difference grid for parallel computing.
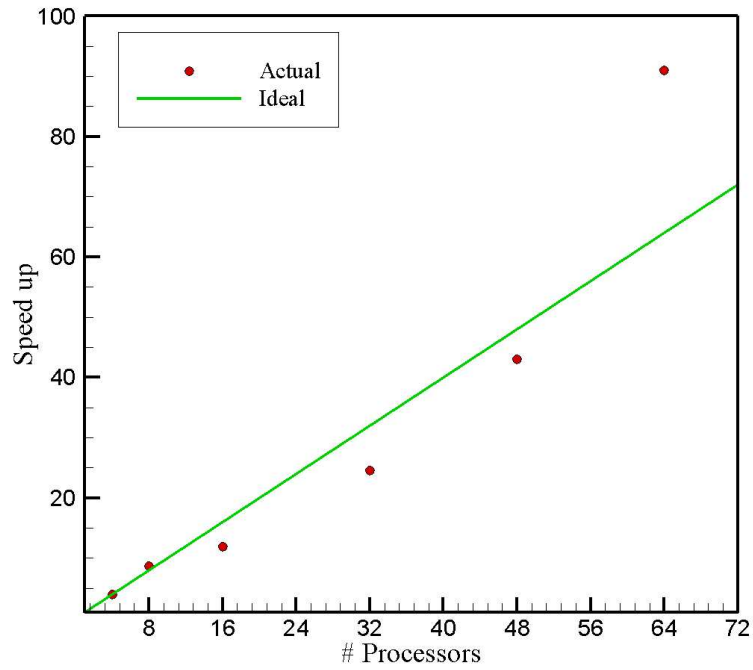
Figure 4.12   Performance on AMD Opteron cluster from 4 to 64 processors.
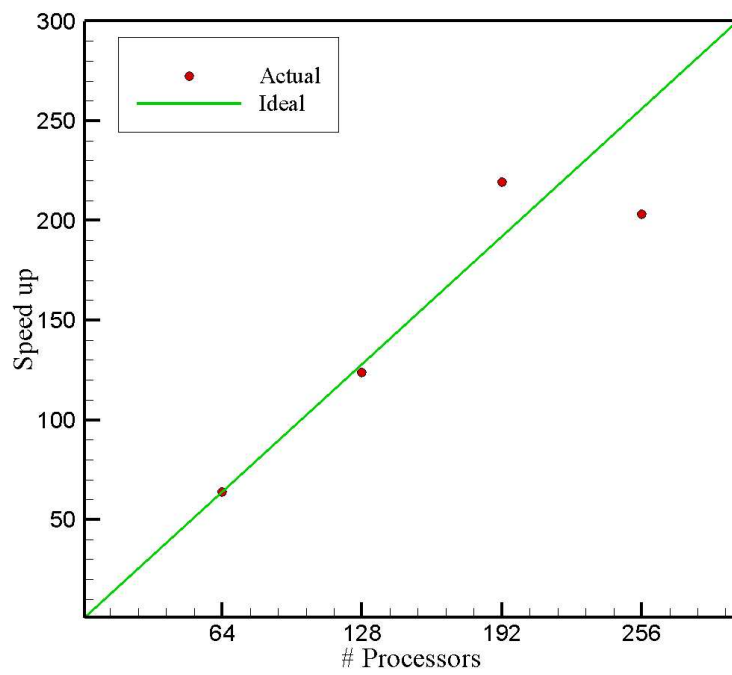
Figure 4.13   Performance on AMD Opteron cluster from 64 to 256 processors.

CHAPTER 5.   LARGE EDDY SIMULATIONS OF A RECTANGULAR JET: MOMENTUM TRANSPORT

In this chapter, large eddy simulations are performed for a confined rectangular jet with co-flowing fluid. The numerical procedure and subgrid models described in chapters 3 and 4 are used to obtain solutions. The effects of grid resolution, numerical schemes and subgrid models on the LES are studied. Validation is performed by comparing LES statistics with those obtained from particle image velocimetry (PIV) measurements. One-point statistics such as the mean and the root mean square (rms) velocity, shear stress, correlation coefficient, skewness and flatness compare well the experimental data. Two-point spatial correlations based on the velocity field are computed and compare very well with experimental data. The chapter ends with a discussion on closures for RANS models based on the eddy viscosity hypothesis and anisotropy invariant mapping of turbulence.

5.1   Confined rectangular jet configuration

Large eddy simulations are performed for a confined planar jet. The schematic of the geometry is shown in Fig. 5.1 with channel dimensions of $0.3 \times 0.06 \times 0.1$ m (x, y, z respectively). There are 3 inlet streams at the inflow boundary, each separated by splitter plates and the flow is bounded by walls in the y- and z- directions. The volumetric flow rates in the two outer streams are 0.4 L/s and in the inner co-flowing stream is 0.8 L/s, and the resulting average velocity in the channel is U_{avg} =0.267 m/s. The Reynolds number based on the average velocity and hydraulic diameter is 2×10^4. The flow is complex due to the presence of gradients in the two shear layers and at the walls. For validation purposes, the results from LES are compared with experimental PIV data. Details of the experimental setup can be found in Feng et al. (2006).

In order to validate the LES with experimental data, inflow conditions that are similar to

those in the experiments are required to justify that there is a one-to-one comparison. For this purpose, the inflow conditioning technique of Klein et al. (2003) is used. The method generates inflow velocity signals that have statistical properties similar to those in the experiments. The inflow velocities are given by

$$\overline{u}_i = \langle u_i \rangle + a_{ij}\mathscr{U}_j$$

where $\langle u_i \rangle$ is the mean inflow velocity from experiments, $\mathscr{U}_j$ is obtained from a random field with a prescribed two point statistic (also obtained from experiments), and

$$(a_{ij}) = \begin{pmatrix} (R_{11})^{1/2} & 0 & 0 \\ R_{21}/a_{11} & \left(R_{22} - a_{21}^2\right)^{1/2} & 0 \\ R_{31}/a_{11} & \left(R_{32} - a_{21}a_{31}\right)/a_{22} & \left(R_{33} - a_{31}^2 - a_{32}^2\right)^{1/2} \end{pmatrix}$$

where R_{ij} is the correlation tensor known from experiments. The advantage of this method is that inflow conditions are obtained as the simulation progresses, unlike methods where prior computations are required specifically to generate and store inflow velocities. PIV measurements are available in the $x - y$ plane at $z = 0.05$ m. For the LES velocity inflow boundary, experimental data obtained at a location 1 cm downstream of the trailing edge of the splitter plates are used. This location is denoted as $x = 0$ cm (refer to Fig. 5.1) and henceforth, all other positions are relative to this location. Moreover, the third velocity component in the spanwise direction is not measured in the experiments and an approximation of $R_{33} = R_{22}$ is made, implying the fluctuations of $\overline{v}$ and $\overline{w}$ velocity components are of equal magnitude, and all other correlations involving the spanwise velocity fluctuation are made zero.

At the walls, a no-slip boundary condition is applied, and at the exit a convective outflow boundary condition is used (Ferziger and Perić, 2002). For the pressure Poisson equation, a zero normal gradient condition is used at the inflow and at the walls. At the outflow boundary zero gage pressure is specified.

5.2 Grid resolution study

In this test, the dynamic SGS model is used (refer to Section 3.3.2) and finite differences are employed using the sixth-order compact finite-difference scheme. The effect of increasing grid

Table 5.1   Grid resolution study parameters for LES: Number of cells used
for the three cases.

	x-direction	y-direction	z-direction
1	160	64	64
2	224	96	96
3	320	134	114

resolution from about 0.5 million to 5 million cells is investigated. It is important to note that the grid size cannot be changed independently of the filter length scale because the filtering is performed implicitly by the grid. The study is performed to obtain a grid resolution sufficient to capture the essential physics of the flow. Non-uniform grids were used with clustering at the wall boundaries and in the shear layers. The aspect ratio $\Delta x/\Delta y$ and $\Delta z/\Delta y$ were maintained between 1 and 3 and the grid sizes used are summarized in Table 5.1   Figure. 5.2 compares the resolved mean streamwise velocity profiles for the LES (lines) with that obtained from PIV measurements (symbols) at streamwise location $x = 7$ cm. The highest resolution grid is able to match the near-wall profile closely with experiments. This is essential since no wall models are used to account for stresses in the developing boundary layers. Figure 5.3 shows the streamwise rms velocity at the same location. Again near-wall behavior is better at the highest resolution. In the shear layers (near $y = 0.04$ m and $y = 0.06$ m), the peaks are similar for the three grid resolutions. The proportion of energy resident in the resolved scales is higher at higher grid resolutions and this explains the overall increase in the intensity for the simulation using 5 million cells. It should be noted that the effective filter width for the highest grid resolution is very close to the resolution of the PIV measurements. Thus the next two studies involving numerical schemes and SGS models are performed with the highest grid resolution ($320 \times 134 \times 114$ cells).

5.2.1   Comment on near wall resolution

It is well known that LES works well away from the walls. Near walls the resolution of LES is comparable to that of a DNS (Pope, 2000). Wall models provide analytical treatment

for the near wall stresses which can otherwise only be resolved by using fine resolution at the wall. Using wall models is tricky, especially if recirculation zones or heat transfer effects are being resolved. In the present research, no wall models are used and the near wall resolution using the highest grid resolution described in the preceding section was enough to capture the slope at the wall accurately. An estimation of the near wall resolution requirement based on analytical treatment is given next.

In order to approximate the near wall resolution, the friction velocity u_τ and wall stress τ_w are required. These characteristic turbulent parameters can be calculated based on correlations for the coefficient of friction C_f:

$$C_f = \frac{f}{4} = \frac{\tau_w}{\frac{1}{2}\rho U_{avg}^2} \tag{5.1}$$

where f is the friction factor, ρ is the fluid density and U_{avg} is the mean velocity. The theoretical friction factor for turbulent flow can be approximated as $f = 0.316 \times Re^{-1/4}$, and for the present flow, $f = 0.0266$. Based on Eq. 5.1, the wall shear stress is $\tau_w = 0.2362$ N/m^2. The friction velocity can be found, where $u_\tau = \sqrt{\frac{\tau_w}{\rho}} = 0.0154$ m/s. The near wall resolution is commonly expressed in terms of non-dimensional units of $y^+ = \frac{y \times u_\tau}{\nu}$ and for the highest grid resolution case (5 million cells), a $y^+ \approx 5$ is obtained for the first off-wall grid point.

5.3   Effect of numerical schemes

The effect of a second-order central difference (FD2), third-order QUICK (FD3) and sixth-order compact (FD6) schemes on the solutions are investigated using 5 million cells and the structure function model. Figures 5.4 and 5.5 show the mean streamwise and the streamwise rms velocity, respectively. The mean profiles match very well with the PIV data for all three schemes. For the rms profiles, all three schemes predict similar peaks in the shear layers near $y = 0.02$ and $y = 0.04$ m. A slight difference in magnitude, however, is seen at $y = 0.03$ m, and the FD2 scheme shows higher rms than the FD3 and FD6 schemes. It could be inferred that the third-order convective scheme (FD3) provides some stabilization as compared to the FD2 scheme, resulting in lower u-rms at $y = 0.03$ m. It is often argued that a dissipative scheme should not be used for LES since it is difficult to differentiate between the numerical dissipation and the SGS dissipation. A calculation was therefore carried out on the same grid

for the FD3 scheme without the SGS model to check the dissipative nature of the scheme. The simulation, however, was unstable leading to a premature end of the calculation. In summary, all three schemes show good comparison with the experiments. Since non-dissipative schemes are preferred for LES, the sixth-order central difference scheme (FD6) is adopted here for further studies.

5.4   Effect of Subgrid models

Four SGS models: constant Smagorinsky, dynamic Smagorinsky, dynamic scale dependent and the structure function model are used to compare the effect of SGS dissipation on the resolved scale solution. A grid size of $320 \times 134 \times 114$ cells and the FD6 scheme is used for all simulations. For the constant Smagorinsky model, $C_s = 0.17$ is chosen (Pope, 2000). A van Driest wall function (van Driest, 1956) is used to reduce the SGS viscosity to zero near wall boundaries. Figures 5.6 and 5.7 show the mean streamwise and the streamwise rms velocities, respectively. The mean profiles compare well for all four SGS models and the peak u-rms values in the shear layers are also resolved. In addition, all four models compare well with the resolved scale statistics of the PIV measurements. Interestingly, the constant Smagorinsky model appears to perform just as well as the dynamic Smagorinsky model in the present case without the need for any coefficient adjustment. The calculation of the dynamic models is more expensive than the structure function model, however.

5.5   One-point velocity statistics

In this section, additional results from the resolved scale simulations are presented. Comparisons with PIV measurements are shown at four streamwise location of $x = 0$, $x = 7$, $x = 13$, and $x = 22$ cm. LES statistics at $x = 0$ cm compare exactly with PIV data since this is the inflow boundary provided for the calculations. LES are obtained with 5 million cells using the FD6 scheme and the structure function model. Although no error bars are shown for the variation in experimental measurements, an error of about 5% is present for measurements using PIV techniques (Hua Feng, 2006) and the experimental errors are slightly larger for near wall measurements.

The mean streamwise velocity profile at the four locations is shown in Fig. 5.8, depicting the growth of the mixing layer. PIV data are represented by symbols and LES by a line. Vorticity is shed at the trailing edge of the splitter plates and the instability mechanism is known as the Kelvin–Helmholtz instability. With increasing downstream distance, the steep gradients in the shear layers are quickly diffused by turbulence. The mean profiles compare very well with experiments for all four locations. At $x = 22$ cm, the peak mean streamwise velocity is slightly underpredicted by the LES. Steep gradients at the wall boundaries are resolved by the grid without resorting to use of wall models.

The streamwise rms velocity is shown in Fig. 5.9. The peaks are seen in the shear layer where the high and low speed fluids mix. At location $x = 0$, in the shear layers, two small sharp peaks are observed, caused by the growing boundary layers on the two sides of the splitter plates. As the steep velocity gradients decrease, the peaks also reduce. The wall normal rms velocity is shown in Fig. 5.10. Note that a similar trend is observed, although the peak intensities for the wall normal rms are slightly lower than the streamwise rms peaks. This trend has been observed by researchers where PIV measured wall normal intensities are slightly lower than their true values (Hua Feng, 2006), and could explain the discrepancy between the LES resolved and the measured values at $x = 7$ and $x = 13$ cm. Another possible explanation for the observed differences is that the effective LES filter width is very close to the interrogation window length scale in the PIV measurements. It is therefore possible that the energetic scales resolved by the two techniques are different. In LES, all information regarding the subgrid scale contribution to the turbulent intensities is lost. The SGS kinetic energy is a measure of the unresolved energy and must be estimated in order to obtain the obtain the total turbulent kinetic energy. This is typically estimated by solving a transport equation for the evolution of the SGS kinetic energy, $\frac{1}{2}\left(\overline{u_i u_i} - \overline{u}_i \overline{u}_i\right)$ (Kim and Menon, 1999). Figure 5.11 shows the spanwise w-rms velocity along the normal direction at the four streamwise locations, however PIV measurements are unavailable for the spanwise velocity component. Note that the intensity is close to the wall normal rms intensity (refer to Fig. 5.10), and substantiates the assumption used in the inlet turbulence model that $\langle w'w'\rangle = \langle v'v'\rangle$. Furthermore, Feng et al. (2005) use the same assumption to estimate the turbulent kinetic energy necessary to obtain inflow conditions

for the RANS $k - \varepsilon$ turbulence model. The correctness of this assumption is therefore validated by the present LES study.

The resolved shear stress is shown in Fig. 5.12. The previous argument offered for the differences in the resolved length scales can also explain the difference between the resolved and measured values of the peak shear stress at $x = 7$ and $x = 13$ cm. The SGS component τ_{12} is an estimate of the unresolved shear stress, however, this is unavailable in the experiments and a model similar to an SGS model must be utilized to obtain this estimate (Hua Feng, 2006). Figure 5.13 shows profiles of the correlation coefficient ρ_{uv} between the resolved streamwise and normal components of turbulent fluctuations, defined by:

$$\rho_{uv} = \frac{\langle u'v' \rangle}{\sqrt{\langle u'^2 \rangle \langle v'^2 \rangle}}$$

The profiles are in good agreement with the experimental data and provide confidence in the reliability of the SGS model. At $x = 22$ cm, the profile resembles that observed in turbulent channel flow calculations (Moin and Kim, 1982).

The velocity skewness and flatness factors are defined as:

$$S(u_i) = \frac{\langle u_i'^3 \rangle}{\langle u_i'^2 \rangle^{3/2}}$$

$$F(u_i) = \frac{\langle u_i'^4 \rangle}{\langle u_i'^2 \rangle^2}$$

respectively. These high-order one-point statistics are shown in Figs. 5.14, 5.15, and 5.16 at $x = 7$, $x = 13$, and $x = 22$ cm, respectively. Skewness is a measure of asymmetry of a distribution. It can be observed from the streamwise skewness plots that the u-velocity ($S(u)$) distribution is symmetric about the center of the channel at $y = 0.03$ m, and also symmetric about the shear layers, $y = 0.02$ and $y = 0.04$ m. For the normal component ($S(v)$), the v-distribution is approximately symmetric about the shear layers and does not exhibit symmetry about the channel center. Flatness, also known as Kurtosis, is a measure of whether the data distribution is peaked or flat relative to a normal distribution. Data sets with high kurtosis tend to have a distinct peak near the mean, decline rapidly, and have heavy tails. Data with low kurtosis tend to have a flat top near the mean. The kurtosis for a standard normal distribution is 3.0, as reported for channel flows (Moin and Kim, 1982), and is seen here at $x = 22$ cm,

where the flow is fast approaching turbulent flow in a channel. Overall, good agreement is observed between computations and experiments, which is especially encouraging, considering the difficulties associated with the measurements of high-order statistics.

5.6 Two-point velocity statistics

Turbulence theory begins with the concept of energy cascade introduced by Richardson in 1922 (Pope, 2000), in which energy from the large scales in the flow is transferred to the small scales and is eventually dissipated by the viscous length scales. Two-point correlations give useful information about this energy cascade and form the basis of spectral theories. Parameters such as the longitudinal and transverse length scales based on the two-point correlations are often used in literature to give the reader a notion of the eddy sizes involved in the flow. For canonical flows such as isotropic turbulence, in which the two-point correlation is completely determined by the longitudinal length scale, aposteriori testing of closure models often involves the prediction of these length scales (Pope, 2000). For more complex flows with no directional homogeneity, eddy structures of different shapes and sizes are prevalent and two-dimensional plots of spatial correlations give a better idea of the energetic eddy structures in the flow. In order to obtain two-point spatial correlations from experiments, measurements with one fixed probe and one moving probe are simultaneously utilized (Shaw et al., 1995). PIV, however, enables measurement of a complete two-dimensional flow field, and spatial correlations can be computed as part of data post-processing (Hua Feng, 2006). Spatial correlations can also be obtained from LES based on the resolved velocity field to provide information about the characteristic flow patterns.

Two-point spatial correlations of the resolved velocity fluctuations are defined as:

$$R_{u_i' u_j'}(x, y; X_0, Y_0) = \frac{\langle u_i'(x, y) u_j'(X_0, Y_0) \rangle}{\sqrt{\langle u_i'^2(x, y) \rangle \langle u_j'^2(X_0, Y_0) \rangle}}$$

where (X_0, Y_0) are the coordinates of a basis point about which the correlation is measured, and (x, y) are locations around the basis point. Here, the correlations are obtained in the plane $z = 0.05$ m at three streamwise locations of $x = 0.09$, 0.15, and 0.24 m. At each streamwise locations, 5 cross-stream locations are chosen as shown in a schematic in Fig. 5.17.

The circles in the figure illustrate the basis points (X_0, Y_0). Figures 5.18- 5.21 show correlations for $R_{u'u'}$, $R_{v'v'}$, $R_{u'v'}$, and $R_{v'u'}$, respectively, where the experimentally measured values and those obtained from LES are superimposed on each other. PIV obtained data are shown as colored contours, while LES statistics are shown as lines, keeping the same scale. Each figure is shown as a matrix of 15 sub-figures; moving from left to right, the X_0 basis point changes from 0.09 m to 0.15 m to 0.24 m, and moving from top to bottom, Y_0 changes from 0.01 m to 0.05 m.

Figure 5.18 shows the streamwise correlation $R_{u'u'}$ field as an ellipse with the major axis aligned in the streamwise direction and slightly inclined to the horizontal. This has been observed previously for incompressible mixing layers (Olsen and Dutton, 2002). The inclination is more apparent near the walls further downstream (e.g., $x = 0.24$ m), and is caused by the growing boundary layers at the walls. The elliptical shape of the correlation field suggests that the correlation distance is longer in the streamwise direction than in the normal direction, and the structures grow larger in size with increasing downstream distance.

Cross-stream correlation functions $R_{v'v'}$ are shown in Fig. 5.19, and the correlation field is a vertically-oriented ellipse. Clearly the fluctuations are strongly correlated in the y-direction than in the x-direction. For the same y-location, the correlations grow in size with increasing downstream distance. The shear layers grow quickly and the correlations span almost the entire height of the channel (e.g., at $X_0 = 0.24, Y_0 = 0.03$ m).

Figure 5.20 shows the cross-correlation fields for $R_{u'v'}$, which are not as well-defined as the correlation fields for $R_{v'u'}$ shown in Fig. 5.21. The trends, however, are the same, i.e., the size of the ellipses increases with downstream distance, and the ellipses are inclined at 45° angle with the horizontal axis. This is seen more clearly for the correlations at locations of $y = 0.04$ m in both Figs. 5.20 and 5.21. As the basis point changes downstream, the peak value at the basis point increases, and the size of the positively correlated region (solid lines) grows, implying an increase in the size of the structures. Another trend is the growth of positively correlated region displacing a negatively correlated region (dashed lines) with increasing streamwise distance. This is seen in the shear layer at $y = 0.04$ m, and vice-versa at $y = 0.02$ m in Fig. 5.20. Similar features are seen in Fig. 5.21.

5.7   Information for RANS closure models from LES

Data obtained from DNS provide scope for the development of turbulence closure models. Since DNS are not feasible for the current application, information useful for providing closures for RANS equations are obtained from the LES database. Two approaches are discussed next.

5.7.1   Simple closure based on the eddy viscosity hypothesis

According to the turbulent viscosity hypothesis, the scalar coefficient, ν_T, is known as the *turbulent viscosity* or *eddy viscosity* and can be evaluated as,

$$\nu_T = \frac{-\langle u'v' \rangle}{\partial u / \partial y}$$

Turbulent viscosity is calculated from the experiments and compared with those obtained based on the resolved scale LES statistics. Figure 5.22 compares the eddy viscosities at four downstream locations. LES predicts a higher eddy viscosity than the experiments, however, both show a wide variation in the streamwise and the transverse directions. The maximum turbulent viscosity appears in the shear-layer regions between the central jet and the outer streams. In regions near the sidewalls, the coefficient becomes small. These observed trends are consistent with the results reported by Lemione et al. (1999).

5.7.2   Closure based on anisotropy invariant mapping of turbulence

In 1977, Lumley and Newman examined the return to isotropy of homogeneous turbulence, and in their analysis utilized the non-dimensional anisotropic Reynolds stress tensor (Lumley and Newman, 1977),

$$a_{ij} = \frac{\overline{u_i u_j}}{q^2} - \frac{1}{3}\delta_{ij}$$

where $q^2 = \overline{u_k u_k}$. An overline here indicates Reynolds averaging and u the fluctuation. The anisotropy can then be quantified in terms of the invariants of a_{ij}, given by $\text{I}_a = a_{kk} = 0$, $\text{II}_a = a_{ij}a_{ji}$, and $\text{III}_a = a_{ij}a_{jk}a_{ki}$, respectively. The functional dependence between the two independent invariants, II_a and III_a, is bounded for all physically realistic turbulent flows and is shown in Fig. 5.23. The bounded region is also commonly known as the Lumley 'triangle'. The two curves originating from the origin (point of isotropy) represent axisymmetric turbulence.

The right-hand side of the 'triangle' represents axisymmetric expansion, where two eigenvalues of the Reynolds stress tensor are smaller than the third. The left side is axisymmetric contraction, where two eigenvalues are larger than the third. The upper curve corresponds to two-component turbulence where one of the eigenvalues is zero. This result is useful in the development of turbulence closure models (Jovanović, 2004).

In the present case, a considerable amount of turbulent energy is present in the resolved scales and the anisotropic tensor can therefore be similarly constructed from the resolved scale Reynolds stress tensor, $\langle u_i' u_j' \rangle$, to quantify the anisotropy in the flow. The quantity $\mathrm{II}_a^{1/2}$ quantifies the magnitude of the anisotropy, while the 'shape' of the anisotropy is given by the value of $(\mathrm{III}_a^{1/3}, \mathrm{II}_a^{1/2})$. The state of anisotropy is shown in Figs. 5.24 – 5.26 at three streamwise locations of 7, 13, and 22 cm, respectively. In each figure, the scatter plot of the invariants is shown along the normal coordinate direction and is colored based on distance from the lower wall ($y = 0$ cm). The anisotropy is highest near the walls and is lower at the center of the channel. At $x = 7$ and $x = 13$ cm, the anisotropy follows the axisymmetric expansion boundary with a few points lying in the region of axisymmetric contraction. Close to the wall boundaries, the points lie close to the two-component boundary. At $x = 22$ cm, the anisotropy is high near the channel walls and the direction of the anisotropy map changes from the right hand side of the boundary to the left hand side in the two shear layers, with the minimum anisotropy occurring at the center of the channel.

Jovanović derives turbulence closures for flows at or close to the boundaries of the anisotropy invariant map. The anisotropy map is narrow, hence, an attempt could be made to interpolate the closures valid around the boundary of the map to turbulent flows whose anisotropy map resides within these boundaries. Based on the invariant maps shown for the rectangular jet configuration, closures could be attempted for the Reynolds stress transport equations.

5.8 Summary

Large eddy simulations were performed for a confined rectangular jet. The flow is complex because of the presence of two shear layers at the inflow and wall boundaries in the normal and spanwise directions. It is shown that an in situ turbulence generation procedure can represent

the experimental data very well to model the inflow boundary conditions. The effect of grid resolution, numerical schemes and subgrid models were studied on the resolved scale statistics in a systematic manner. Although most LES studies advocate the use of central difference schemes, the third order Quick scheme gave good results in the present study. The constant Smagorinsky model, using the standard value for the constant, was not found to be overly dissipative as is generally observed. In fact, the four models tested show similar resolved scale statistics, which leads to the impression that the grid size used for the study is able to resolve most of the turbulent energy and a simple closure is sufficient to model the subgrid scales. One-point statistics for the mean streamwise velocity, the rms velocities, shear stress and correlation coefficient compare well with experiments. Information regarding the spanwise rms velocity, which is unavailable from the experiments, was used to complement the turbulent kinetic energy information required for RANS models. Third- and fourth-order resolved scale statistics correspond well with experimental values, further validating the LES study. Two-point correlations compared well with experiments, thus proving that LES is able to resolve the eddies in the shear layers and the flow in general. The invariance map was calculated to demonstrate the state of anisotropy of turbulence in the flow in an attempt to provide information for closures for RANS equations.
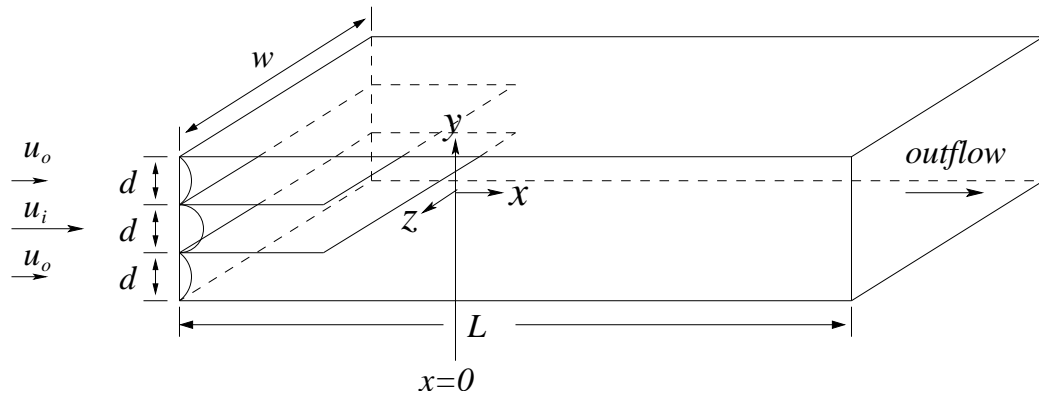
Figure 5.1   Schematic of a confined planar jet.

Figure 5.2   Mean streamwise velocity profile at $x = 7$ cm for three different grid resolutions in the normal direction, with comparisons to experiments.
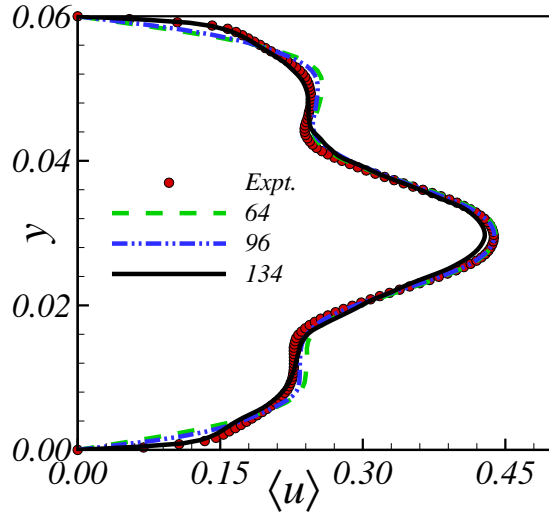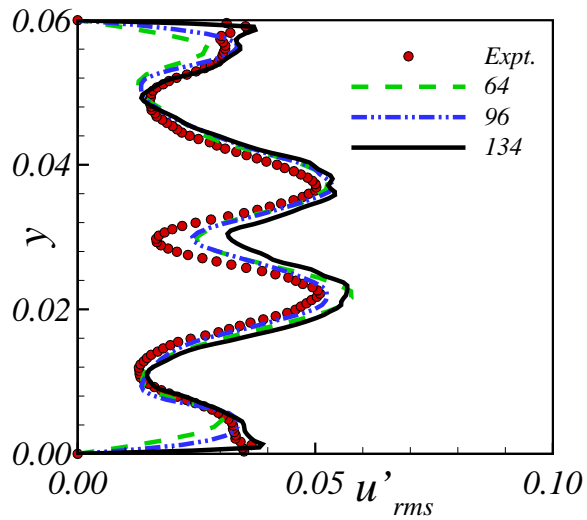

Figure 5.3   Streamwise rms velocity profile at $x = 7$ cm for three different grid resolutions in the normal direction, with comparisons to experiments.
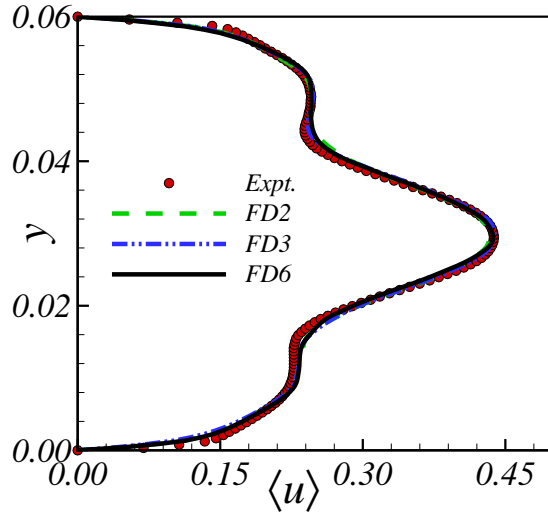
Figure 5.4   Mean streamwise velocity profile at $x = 7$ cm for a second-order central difference (FD2), a third-order Quick (FD3) and a sixth-order compact (FD6) finite difference scheme.
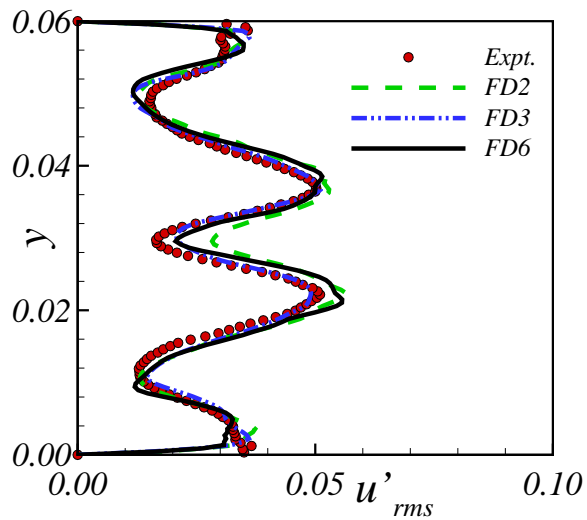
Figure 5.5   Streamwise rms velocity profile at $x = 7$ cm for a second-order central difference (FD2), a third-order Quick (FD3) and a sixth-order compact (FD6) finite difference scheme.
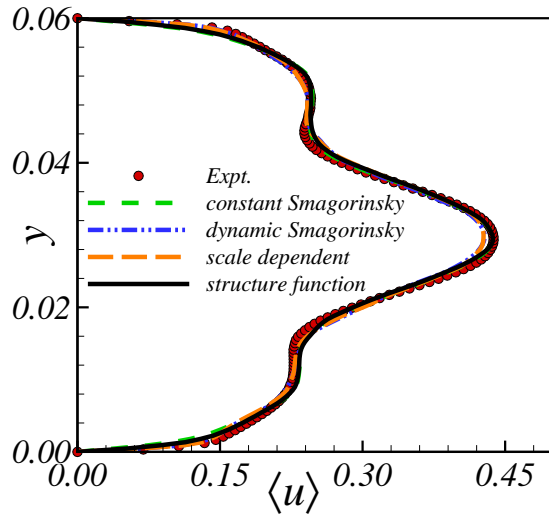
Figure 5.6   Mean streamwise velocity profile at $x = 7$ cm comparing solutions using different subgrid stress models with experiments.
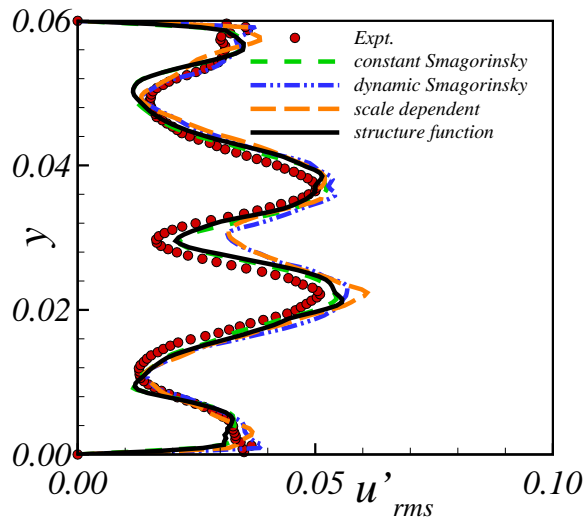
Figure 5.7   Streamwise rms velocity profile at $x = 7$ cm comparing solutions using different subgrid stress models with experiments.
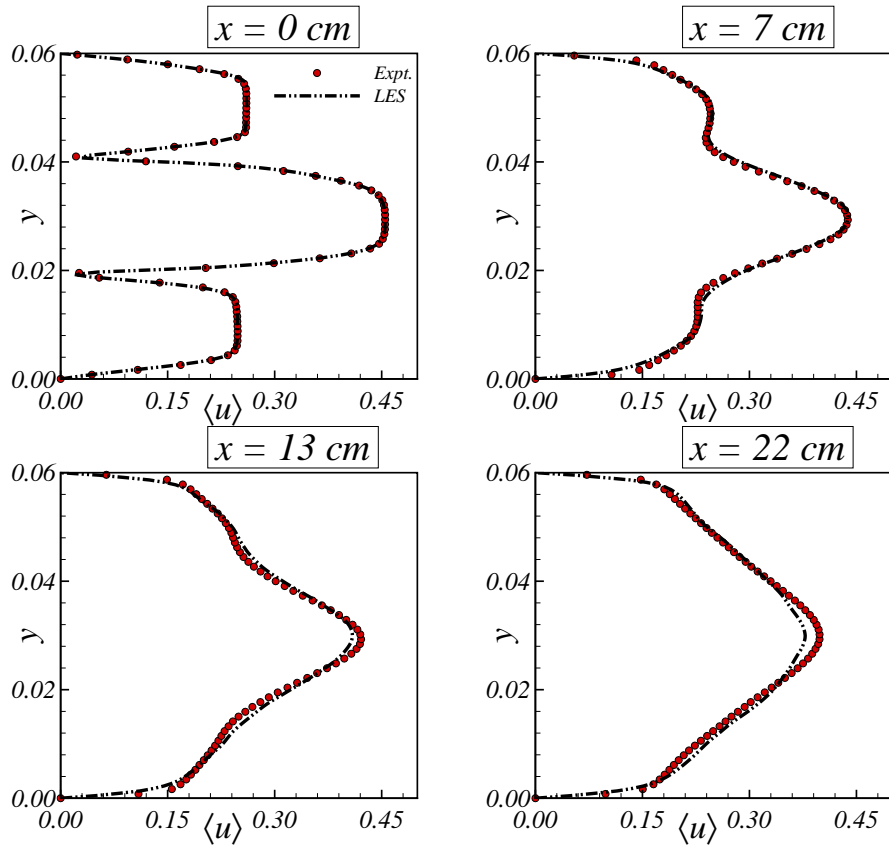
Figure 5.8   Mean streamwise velocity profiles at four streamwise locations
downstream of the splitter plates depicting growth of mixing
layer.
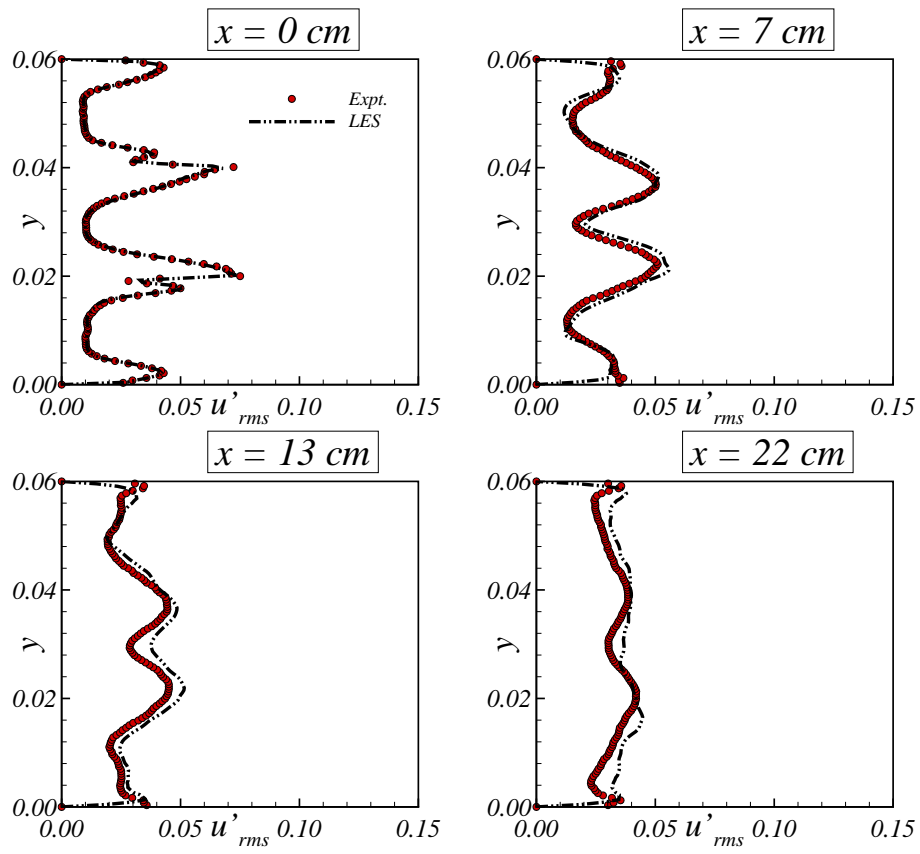
Figure 5.9   Streamwise rms velocity profiles at four streamwise locations downstream of the splitter plates.
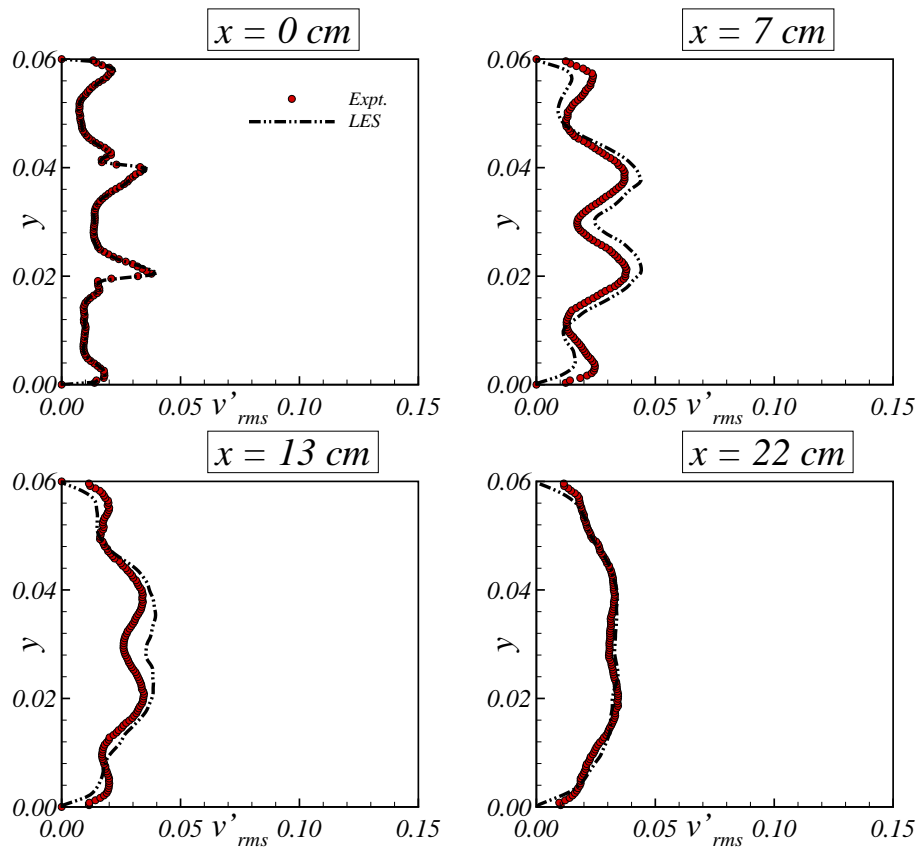
Figure 5.10   Wall normal rms velocity profile at four streamwise locations downstream of the splitter plates.
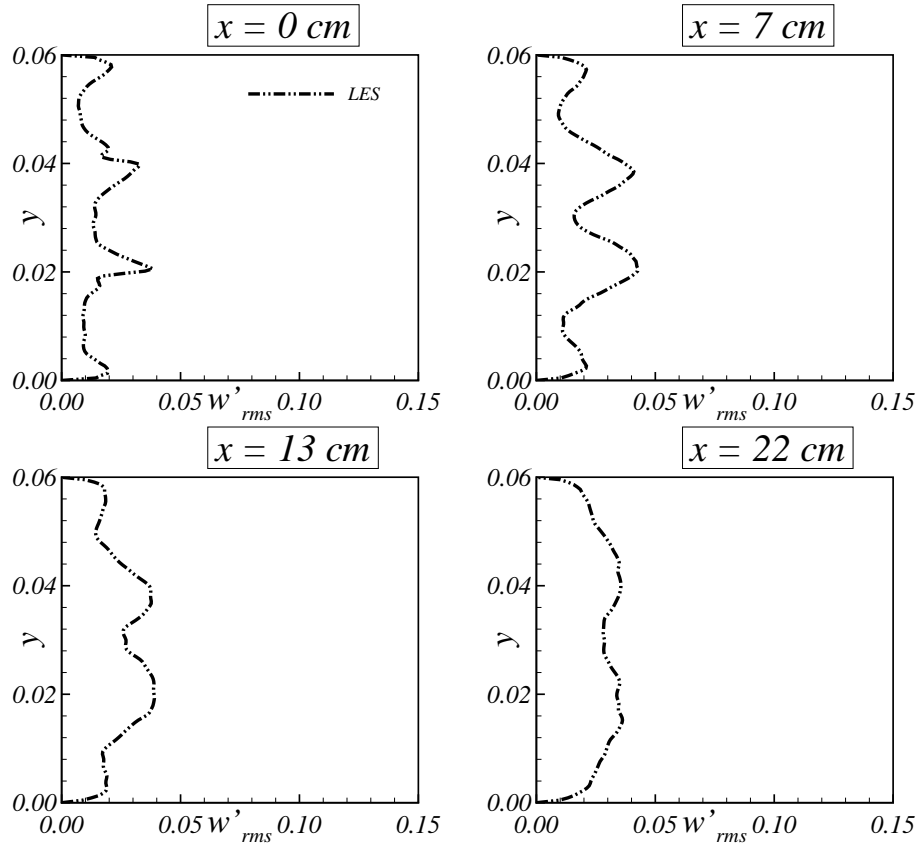
Figure 5.11   Spanwise rms velocity profile at four streamwise locations
downstream of the splitter plates. Note that experimental data
is not available for comparisons.

65
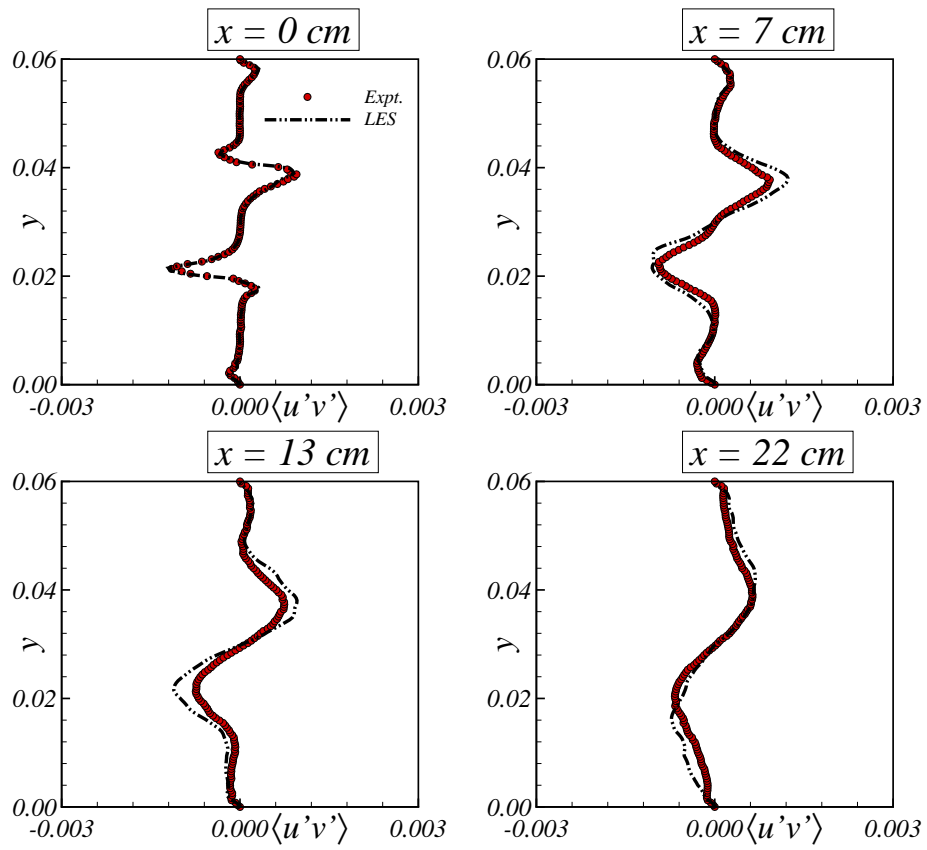
Figure 5.12   Resolved shear stress at four streamwise locations downstream
of the splitter plates.

66
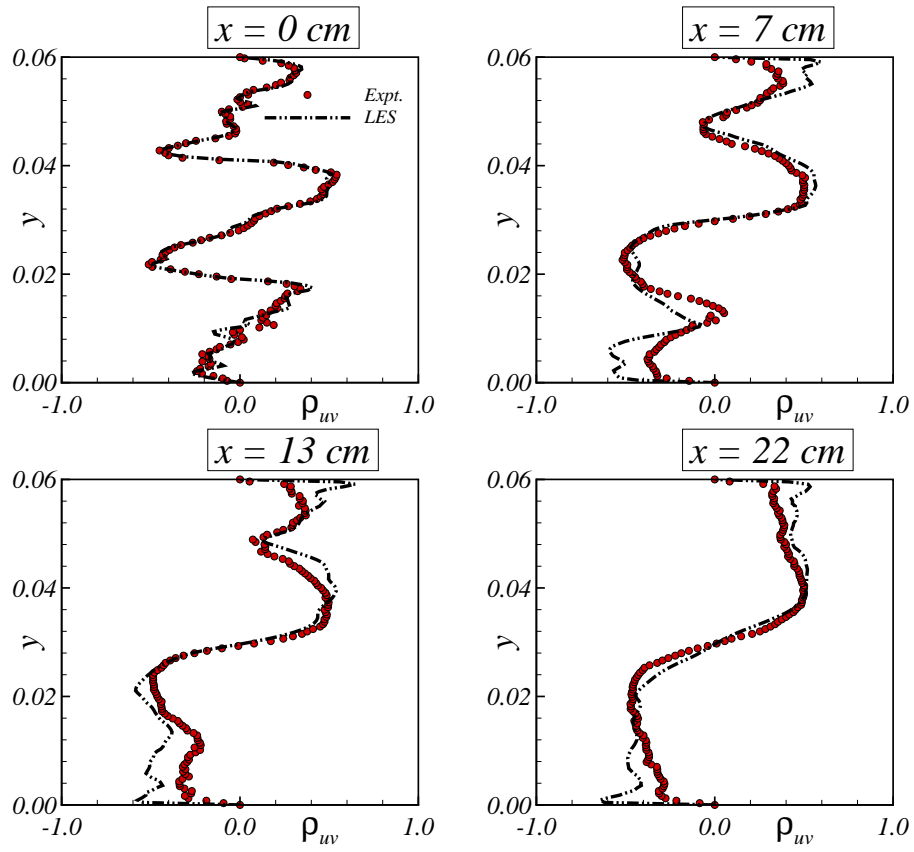
Figure 5.13   Correlation coefficient profiles at four streamwise locations downstream of the splitter plates.
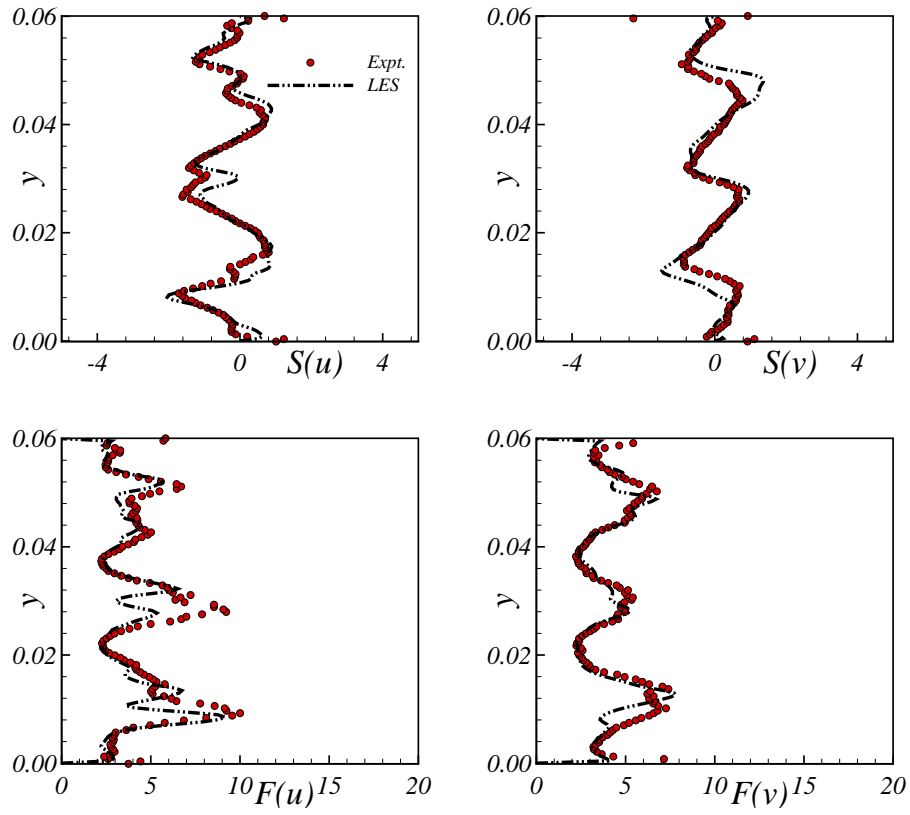
Figure 5.14   Skewness (S) and Kurtosis (F) for u- and v-velocity at $x = 7$ cm.

68
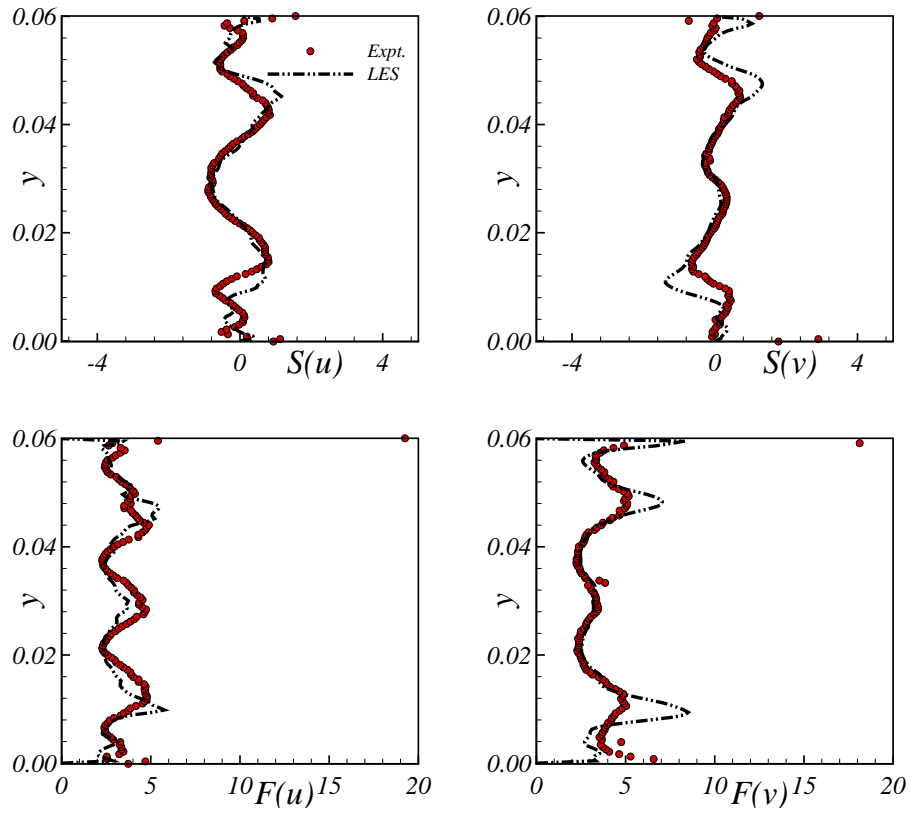
Figure 5.15   Skewness (S) and Kurtosis (F) for u- and v-velocity at $x = 13$ cm.
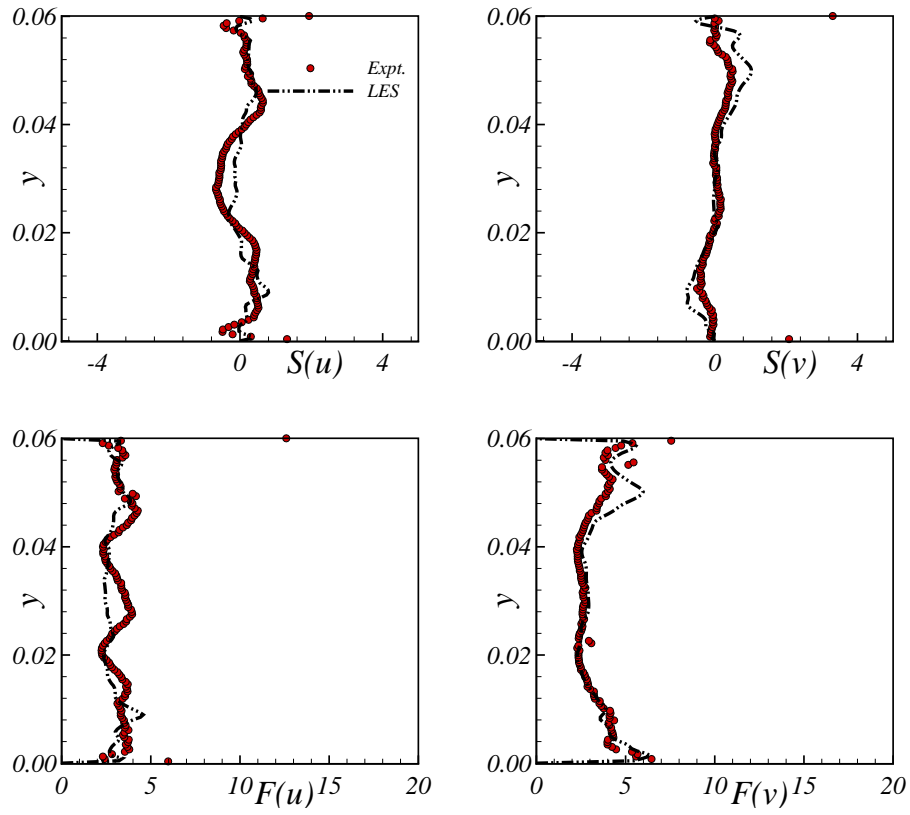
Figure 5.16   Skewness (S) and Kurtosis (F) for u- and v-velocity at $x = 22$ cm.
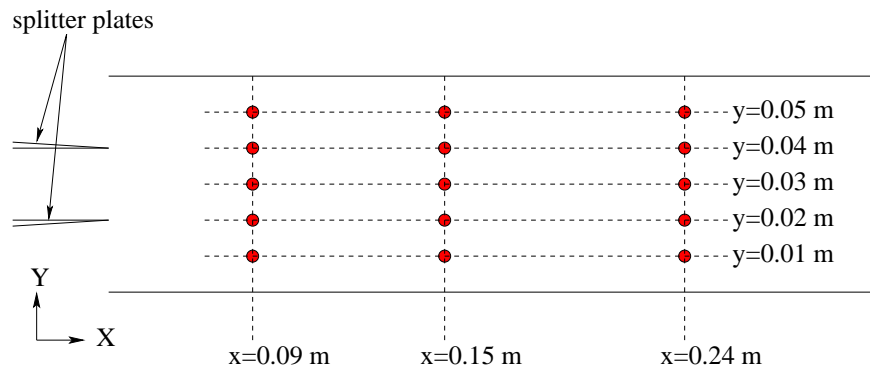
Figure 5.17   Schematic of measurement plane for two-point velocity corre-
lations. Correlations are obtained at 15 points in the plane
shown with circles.
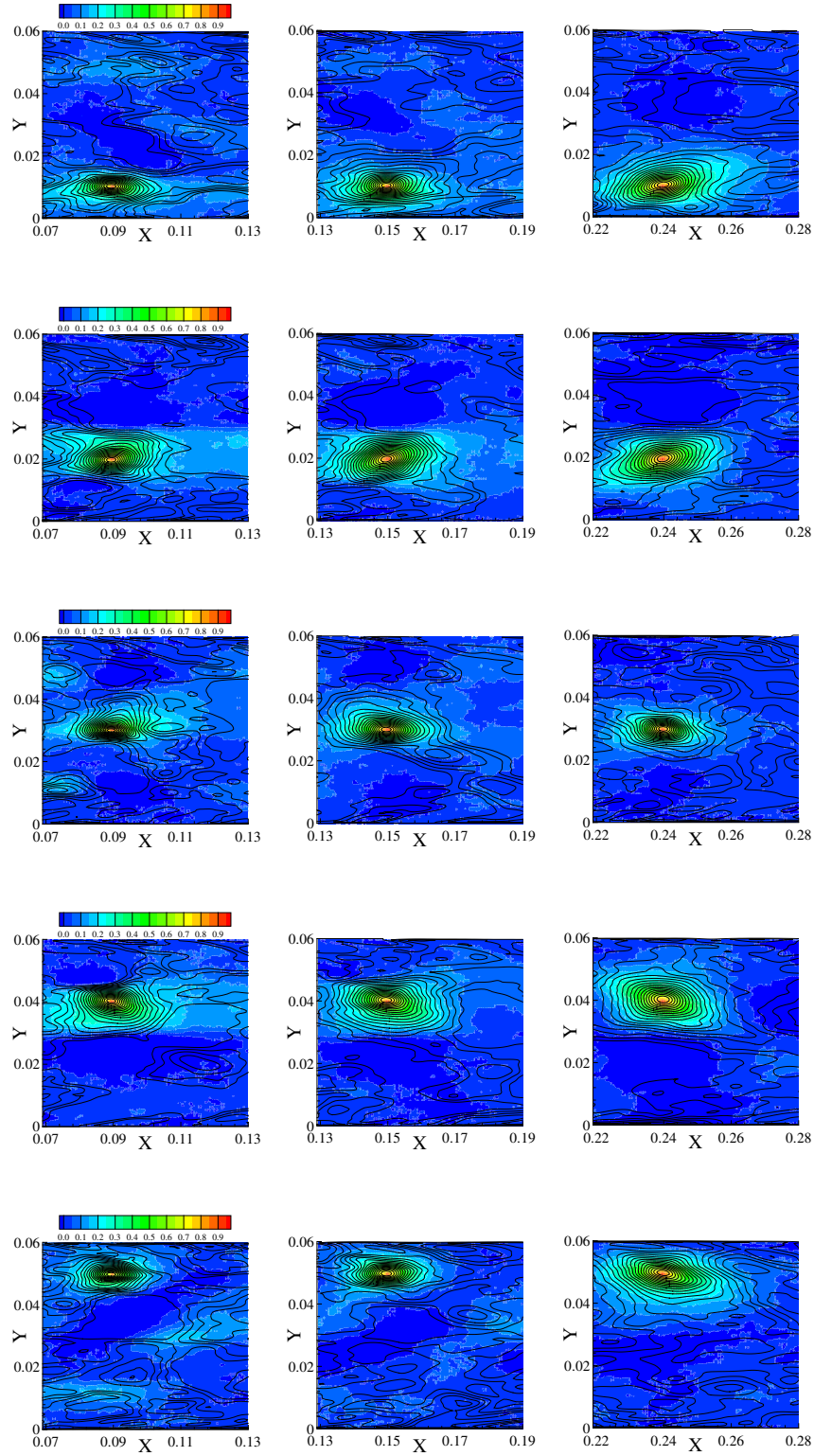
Figure 5.18   Spatial correlations of streamwise velocity $R_{u'u'}$. Left to right column shows correlations at increasing streamwise distance. Top to bottom shows correlations at increasing distance from bottom wall. Experimental data is shown as colored contour and LES solution is superimposed as solid lines. The range is divided into 20 equal intervals for both data.
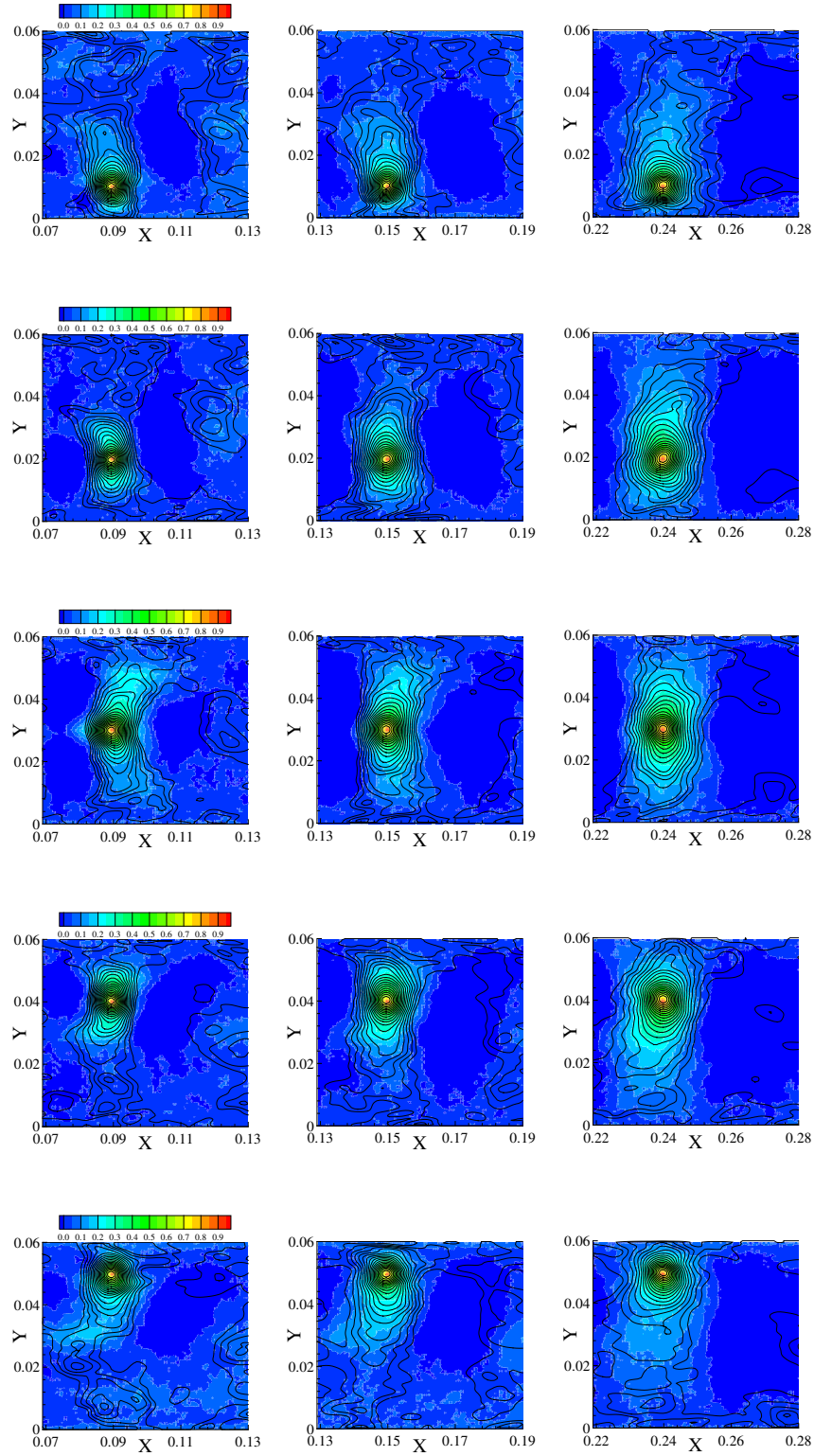
Figure 5.19   Spatial correlations of cross-stream velocity $R_{v'v'}$. Left to right column shows correlations at increasing streamwise distance. Top to bottom shows correlations at increasing distance from bottom wall. Experimental data is shown as colored contour and LES solution is superimposed as solid lines. The range is divided into 20 equal intervals for both data.
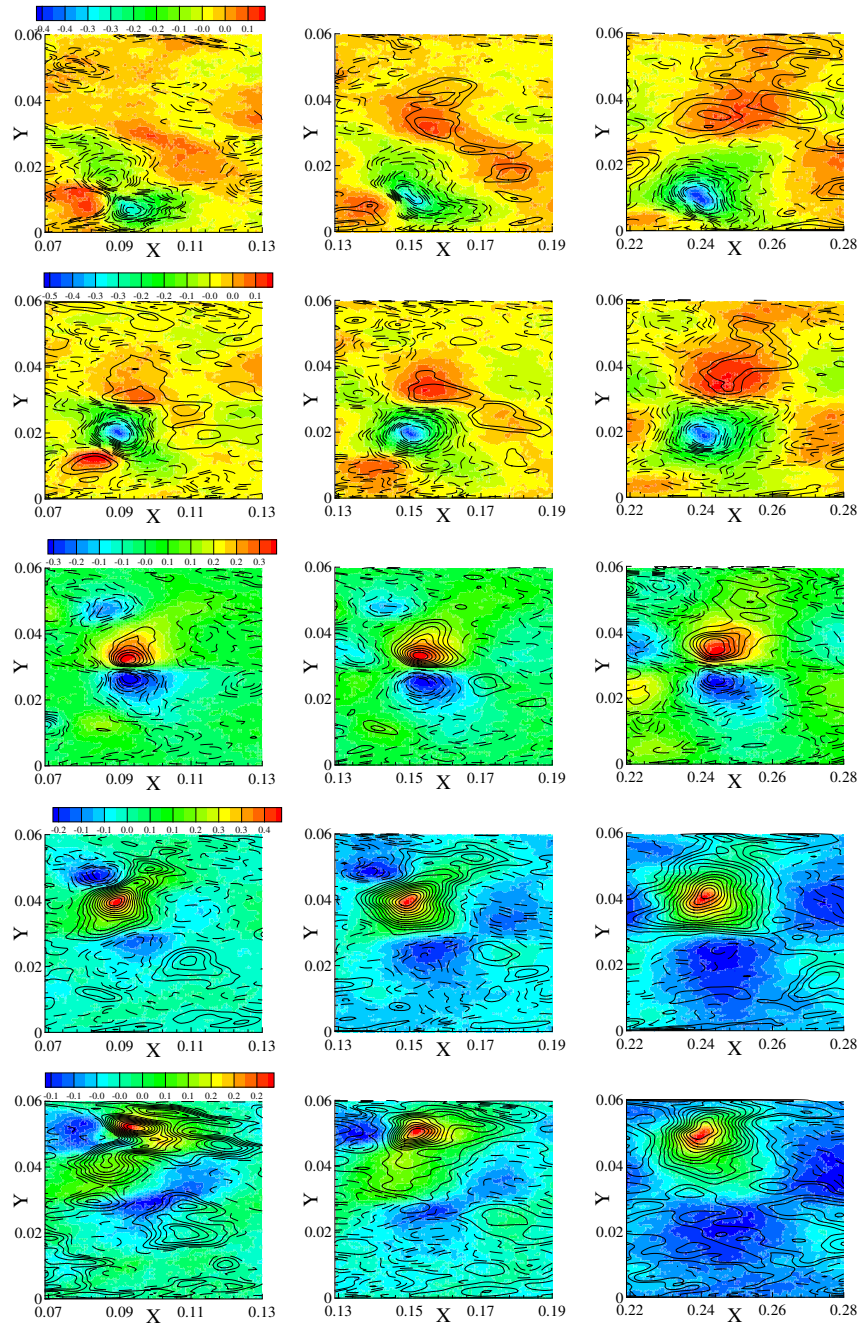
Figure 5.20   Spatial correlations $R_{u'v'}$. Left to right column shows correlations at increasing streamwise distance. Top to bottom shows correlations at increasing distance from bottom wall. Experimental data is shown as colored contour and LES solution is superimposed as solid lines. The range is divided into 20 equal intervals for both data.

74
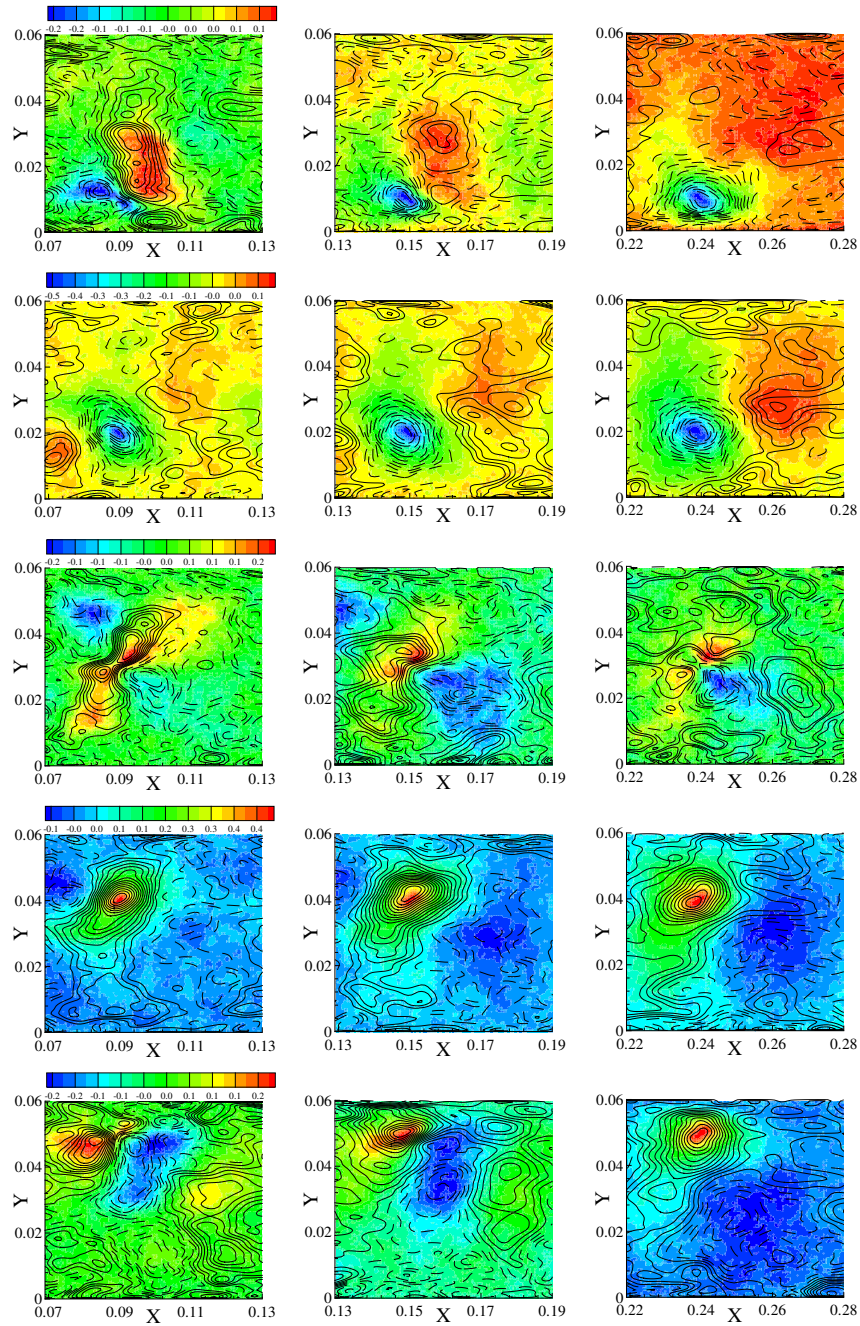
Figure 5.21   Spatial correlations $R_{v'u'}$. Left to right column shows correlations at increasing streamwise distance. Top to bottom shows correlations at increasing distance from bottom wall. Experimental data is shown as colored contour and LES solution is superimposed as solid lines. The range is divided into 20 equal intervals for both data.
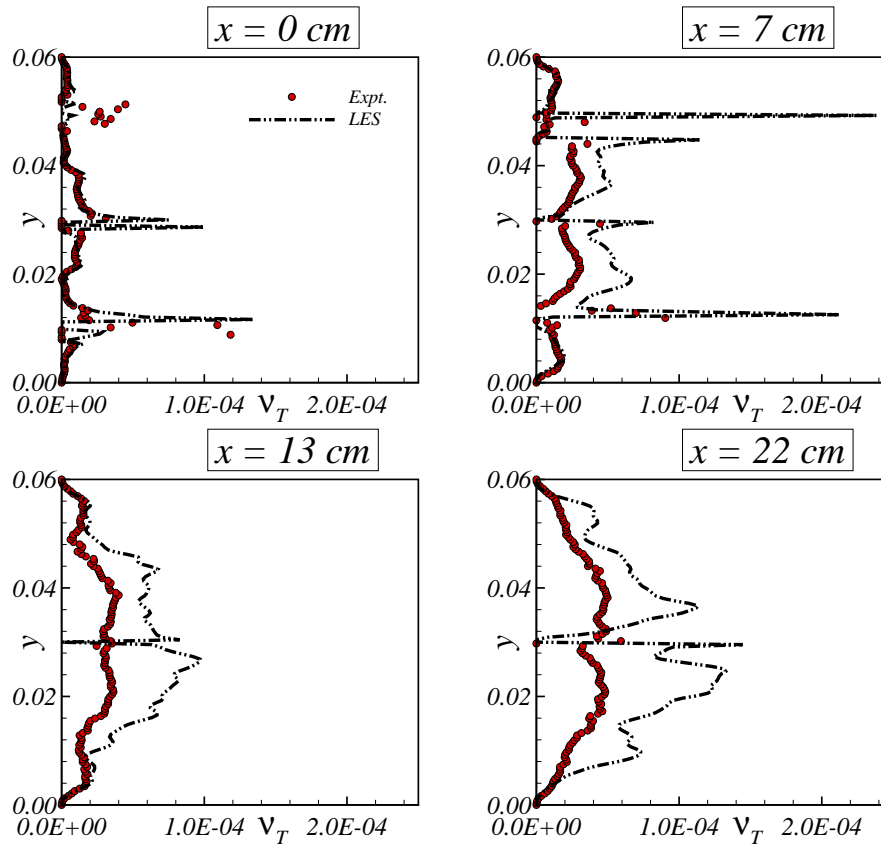
Figure 5.22   Comparisons between LES predicted eddy viscosity and experimentally obtained values at four downstream locations.
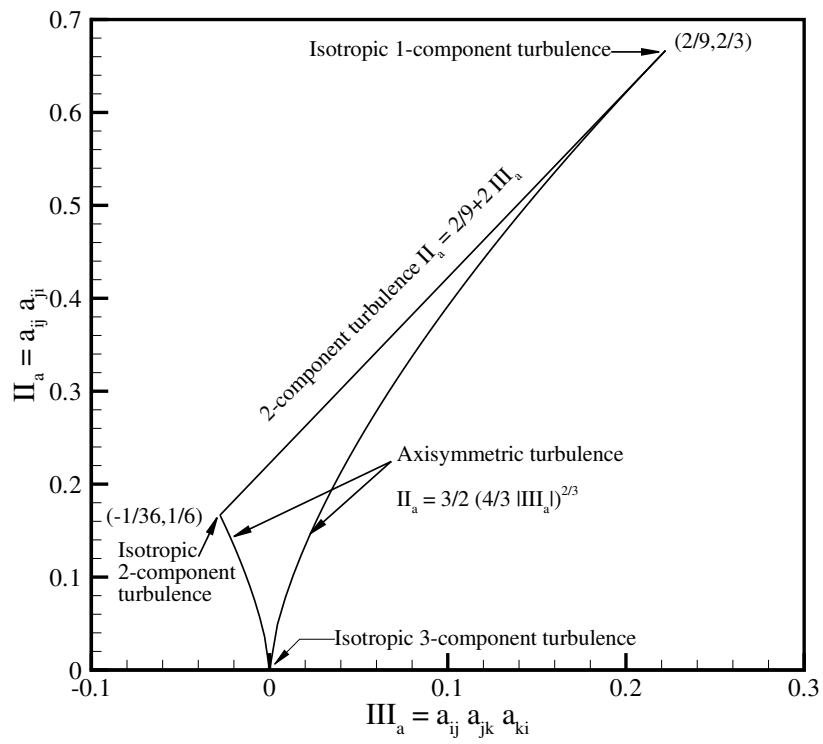
Figure 5.23   Anisotropy invariant map of a_{ij} and the limiting values of II_a and III_a for the different states of turbulence.
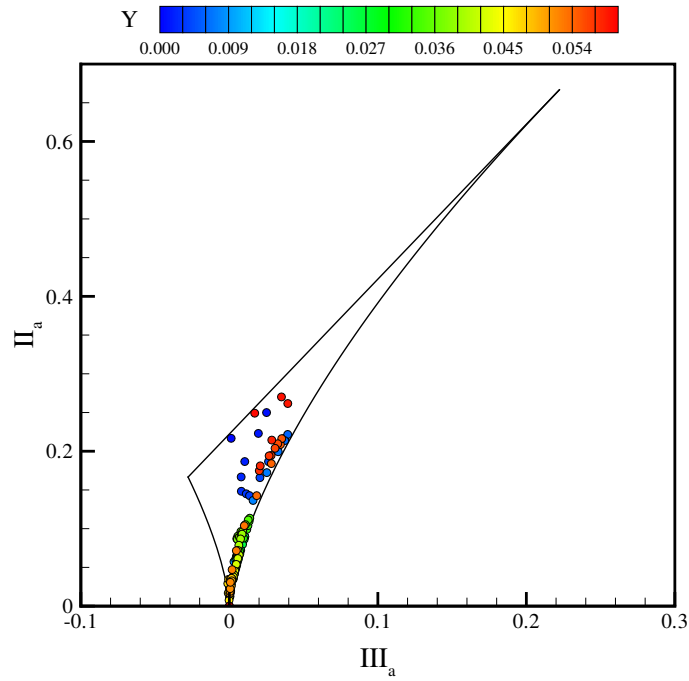
Figure 5.24   The resolved Reynolds stress anisotropy shown using the Lumley invariant map at $x = 7$ cm.
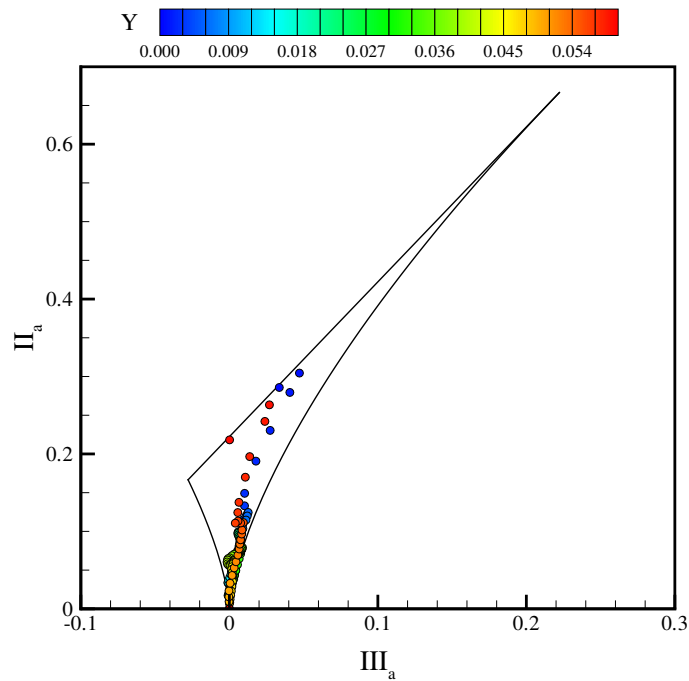
Figure 5.25   The resolved Reynolds stress anisotropy shown using the Lumley invariant map at $x = 13$ cm.
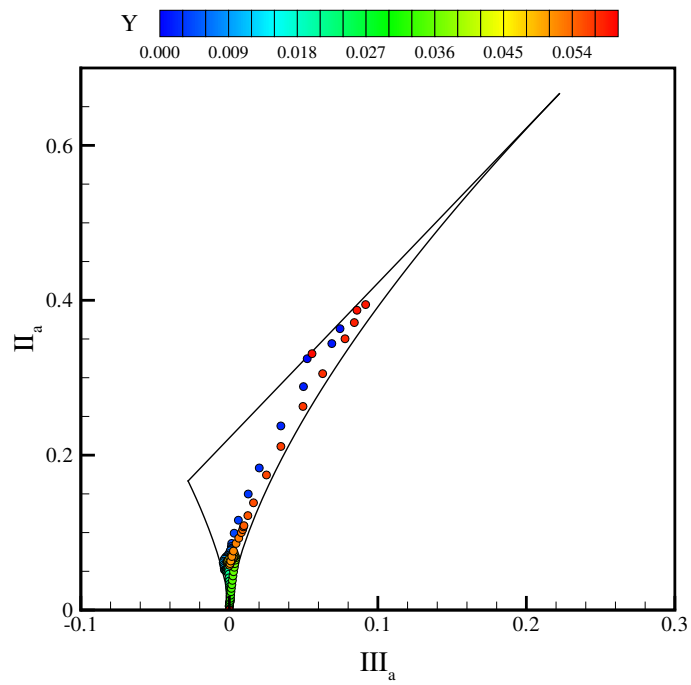
Figure 5.26   The resolved Reynolds stress anisotropy shown using the Lumley invariant map at $x = 22$ cm.

CHAPTER 6.   LARGE EDDY SIMULATIONS OF A RECTANGULAR JET: PASSIVE SCALAR TRANSPORT

In this chapter, large eddy simulations are performed to include the transport of a conserved scalar for the confined rectangular jet with co-flowing fluid streams. The work complements chapter 5 by examining different subgrid scale models for the diffusion of a scalar. In particular, substantial effort went into testing various numerical schemes for the discretization of the scalar transport equation. The choice of numerical scheme is shown to impact the conservation of scalar mass since the grid resolution for LES is low as compared to the DNS requirement. Validation is performed by comparing LES statistics with those obtained from planar laser induced fluorescence (PLIF) experiments. Predictions of the scalar mean, scalar rms and scalar fluxes (obtained from simultaneous PIV and PLIF measurements) compare well with the experimental data. The chapter ends with a summary of the appropriate combination of numerical scheme and subgrid scale model for simulations of a complex flow.

6.1   Scalar transport equations

The mixing of two or more fluids at the molecular level plays an important role in chemically reacting flows. In chemical reactors, often, the objective is to obtain rapid rates of mixing, and hence practical problems generally focus on scalar mixing in turbulent flows. In many applications for reacting flows, it is the processes occurring at the molecular diffusion scales in the scalar field that are crucial in determining the outcome of the mixing process. Such problems are often formulated in terms of an appropriately defined conserved passive scalar quantity known as the mixture fraction. A passive scalar can be thought of as a tracer dye in a fluid flow that is present in such low concentrations that it has no dynamical effect on the fluid motion itself.

Assuming a constant scalar diffusivity, D, the passive scalar field ϕ satisfies the advection-diffusion equation,

$$\left[\frac{\partial}{\partial t} + \mathbf{u} \cdot \nabla - \frac{1}{ReSc} \nabla^2 \right] \phi(\mathbf{x}, t) = 0 \tag{6.1}$$

where, $\mathbf{u}$ is the velocity field advecting the scalar, Re is the Reynolds number and Sc is the Schmidt number. Equation 6.1, although linear in ϕ, involves plenty of dynamics, which can be understood via transport equations for the scalar energy, scalar gradients and scalar dissipation (Buch and Dahm, 1996). To discern the fine structures of mixing, one can define the scalar energy per unit mass $\frac{1}{2}\phi^2(\mathbf{x}, t)$, which is analogous to kinetic energy. The transport equation for scalar energy is given by,

$$\left[\frac{\partial}{\partial t} + \mathbf{u} \cdot \nabla - \frac{1}{ReSc} \nabla^2 \right] \frac{1}{2}\phi^2(\mathbf{x}, t) = -\frac{1}{ReSc} \nabla\phi \cdot \nabla\phi(\mathbf{x}, t) \tag{6.2}$$

The right hand side of Eq. 6.2 gives the local instantaneous rate at which molecular diffusion reduces non-uniformities in the scalar energy field and is called the scalar dissipation. The transport equation for the scalar gradient vector that appears on the right hand side of Eq. 6.2 is,

$$\left[\frac{\partial}{\partial t} + \mathbf{u} \cdot \nabla - \frac{1}{ReSc} \nabla^2 \right] \nabla\phi(\mathbf{x}, t) = -(\nabla\phi \cdot \mathbf{S}) - (\nabla\phi \times \frac{1}{2}\omega) \tag{6.3}$$

The first term on the right hand side of Eq. 6.3 describes the change in magnitude and direction of the scalar gradient vector due to the local strain rate tensor, $\mathbf{S} = \frac{1}{2}(\nabla\mathbf{u} + \nabla\mathbf{u}^T)$ associated with the underlying velocity field. The second term on the right hand side of Eq. 6.3 gives the pure rotation of the scalar gradient vector with the fluid vorticity without any change in the gradient magnitude. The scalar dissipation in Eq. 6.2 is the magnitude squared of the scalar gradient vector in Eq. 6.3, and follows the transport equation,

$$\left[\frac{\partial}{\partial t} + \mathbf{u} \cdot \nabla - \frac{1}{ReSc} \nabla^2 \right] \frac{1}{2}(\nabla\phi \cdot \nabla\phi) = -(\nabla\phi \cdot \mathbf{S} \cdot \nabla\phi) - \frac{1}{ReSc} \nabla(\nabla\phi) : \nabla(\nabla\phi) \tag{6.4}$$

In the first term on the right in Eq. 6.4, the symmetric contraction selects the normal component of the strain rate tensor along the local scalar gradient vector direction, giving $-\mathbf{S}_{\nabla\phi\nabla\phi}(\nabla\phi \cdot \nabla\phi)$. The remaining components of the strain rate tensor act only to change the gradient vector orientation but do not affect the magnitude. This results in a reduction of the scalar gradient magnitude due to extensional straining along the gradient direction or, conversely, the increase

in dissipation resulting from compression of the scalar gradient. The second term on the right in Eq. 6.4 is strictly negative and gives the reduction in dissipation due to diffusional cancellation of gradients in the scalar field.

The role of molecular diffusion in mixing is characterized by the Schmidt number, $Sc = \nu/D$, which is the ratio of the kinematic viscosity of the fluid to the molecular diffusivity. Some examples where $Sc \gg 1$ are the mixing of fine particles such as soot or oil droplets in the atmosphere, the mixing and reaction of aqueous acid-base solutions, or the mixing of various components in a wide range of liquid-phase chemical, pharmaceutical, and industrial processes. Examples when $Sc \approx 1$ include gaseous-phase mixing and combustion and $Sc \ll 1$ for mixing in plasmas. The range of scales present in the scalar field is sensitive to Sc. For $Sc < 1$ the smallest scale is estimated to be the Obukhov–Corrsin scale $\lambda_{oc} \equiv \lambda_\nu Sc^{-3/4}$ while, for $Sc \gg 1$, the smallest scale is the Batchelor scale $\lambda_B \equiv \lambda_\nu Sc^{-1/2}$ (Fox, 2003). A major difficulty in studying turbulent mixing at high Sc is the need to resolve scales of size λ_B, which is much smaller than the smallest scale of the velocity field. This puts stringent demands on the sensitivity of measurement capabilities in experiments as well as grid resolution and consequent CPU expense in DNS.

Insight into the fine structure of the scalar dissipation fields have been provided by experimental measurements of Dahm et al. (1991) and Buch and Dahm (1996, 1998). They found that the scalar dissipation field shows 'spottiness' and has a sheet-like topology, and unlike the vorticity field in turbulent flows, the scalar gradients are concentrated solely on sheet-like small-scale structures. This supports the sheet-like conceptual models of reacting turbulent flows, such as the flamelet models (e.g., Gibson and Libby, 1972). Vedula et al. (2001) obtained a similar 'spottiness' of the dissipation rate in their DNS study where they observed that the scalar dissipation fluctuations are highly intermittent. Eswaran and Pope (1987) found from their DNS simulations ($Sc = 0.7$) that the initial scalar to velocity integral length-scale ratio influences the evolution of scalar fields and the probability density function (PDF) of scalar field becomes Gaussian. It was also found that the shape and evolution of the scalar PDF does not depend on the initial length-scale ratio. DNS have also been performed by Yeung et al. (2002) for $Sc = 64$, Brethouwer et al. (2003) for $Sc = 144$ and Yeung et al. (2004) up to $Sc = 1024$.

The emphasis has been on resolving the viscous-convective range of scales ($\lambda_\nu > l > \lambda_B$) and the Reynolds number is kept low so as to reduce grid resolution requirements. Yeung et al. (2004) found from their study of forced isotropic turbulence with an imposed uniform mean scalar gradient that the scalar spectrum resembles the k^{-1} viscous-convective range as Sc is raised from 64 to 1024. They also found that the scalar variance increases slightly with Sc, but the scalar dissipation rate is independent of Sc.

DNS, however is not possible for most flows of practical importance. LES has shown success in predicting passive scalar transport, e.g., Moin et al. (1991), Ribault et al. (2001), Herrmann et al. (2004), Chumakov et al. (2004). Very few studies have attempted LES of high Schmidt numbers, e.g., Dong et al. (2003) for $Sc = 200$, Burton (2005) for $Sc = 100$. An objection commonly raised against LES is that turbulent mixing requires molecular mixing at the diffusive scales, and therefore LES, which does not directly represent the diffusive scales should not yield accurate predictions. Mahesh et al. (2005) answer this concern by proposing a kinematic model for the scalar fluctuations without detailed knowledge of the diffusive processes. They conclude that any model which accurately captures the energy-containing convective motions, and the approximate thickness of the scalar fronts can yield good predictions for the scalar field. Mahesh et al. (2005) also state that predictions in gas-phase flows, or high Reynolds number flows are likely to be easier than those in liquid-phase, low Reynolds number flows.

6.2   Numerical scheme for scalar transport

Numerical schemes for scalar transport equations are challenging from the viewpoint of stability. Unlike velocity transport, the solution of a conserved scalar transport equation should preserve boundedness. This is especially difficult in LES simulations, where a low spatial resolution causes the filtered scalar field to fluctuate sharply between its minimum and maximum values. It has been shown that the advection equation solved using central difference schemes can lead to oscillations and instabilities (Pierce, 2001). To counter this problem, explicit schemes using an upwind bias, e.g., the quadratic upstream interpolative convective kinematic (QUICK) scheme (Leonard, 1979), can reduce numerical oscillations, however, they can lead to artificial diffusion. In spite of this drawback, upwind schemes are being used due

to their robust numerical stability. Essentially non-oscillatory (ENO) and weighted essentially non-oscillatory (WENO) schemes have been used for advection-type equations involving sharp gradients (Shu, 1997). In the following paragraphs, these schemes are discussed in detail with regard to their discretization.

The velocity and scalar are defined at the grid nodes and the scalar fluxes are evaluated at the interface between two grid nodes to ensure and maintain flux balance. To illustrate how the fluxes are calculated, a 1-D schematic is shown in Fig. 6.1. The flux evaluations are performed at the interface indicated by the vertical lines (f_l indicates flux at left face and f_r indicates flux at right face). The convective term is evaluated as,

$$\frac{\partial u\phi}{\partial x} = \frac{u_r\phi_r - u_l\phi_l}{dx} \tag{6.5}$$

and $f_l = u_l\phi_l$ and $f_r = u_r\phi_r$.

Four schemes are described here: a second-order central difference scheme (CD), a third-order QUICK scheme, a third-order WENO scheme and a fifth-order WENO scheme. For all the schemes, the velocities at the cell faces are interpolated as:

$$
\begin{aligned}
u_l &= \frac{1}{2}\left(u_{i-1} + u_i\right) \\
u_r &= \frac{1}{2}\left(u_i + u_{i+1}\right)
\end{aligned}
$$

For the CD scheme, the right hand side of Eq. 6.5 are defined as:

$$
\begin{aligned}
\phi_l &= \frac{1}{2}\left(\phi_{i-1} + \phi_i\right) \\
\phi_r &= \frac{1}{2}\left(\phi_i + \phi_{i+1}\right)
\end{aligned}
$$

and for the QUICK scheme, the terms in Eq. 6.5 are defined as:

$$
\begin{aligned}
\phi_r &= \frac{6}{8}\phi_{i+1} + \frac{3}{8}\phi_i - \frac{1}{8}\phi_{i+2} \quad (u_r < 0) \\
\phi_r &= \frac{6}{8}\phi_i + \frac{3}{8}\phi_{i+1} - \frac{1}{8}\phi_{i-1} \quad (u_r > 0) \\
\phi_l &= \frac{6}{8}\phi_i + \frac{3}{8}\phi_{i-1} - \frac{1}{8}\phi_{i+1} \quad (u_l < 0) \\
\phi_l &= \frac{6}{8}\phi_{i-1} + \frac{3}{8}\phi_i - \frac{1}{8}\phi_{i-2} \quad (u_l > 0)
\end{aligned}
$$

For the WENO schemes, extra terms need to be defined. The flux definitions are shown for ϕ_r (Jiang and Shu, 1996). The definitions for ϕ_l are straightforward. For the fifth-order WENO scheme, three stencils containing three cells each are associated with every node in the grid (Note: The third-order WENO scheme utilizes two stencils with two cells each. For details, refer to Jiang and Shu, 1996). Each of the three stencils give rise to approximations for the fluxes denoted by ϕ_r^m ($m = 0, 1, 2$):

$$
\begin{aligned}
\phi_r^0 &= \frac{1}{3}\phi_i + \frac{5}{6}\phi_{i+1} - \frac{1}{6}\phi_{i+2} \\
\phi_r^1 &= -\frac{1}{6}\phi_{i-1} + \frac{5}{6}\phi_i + \frac{1}{3}\phi_{i+1} \\
\phi_r^2 &= \frac{1}{3}\phi_{i-2} - \frac{7}{6}\phi_{i-1} + \frac{11}{6}\phi_i
\end{aligned}
$$

Next, positive (w_m) and negative ($\tilde{w}_m$) weights are computed as $w_m = \alpha_m / \sum_{m=0}^{2} \alpha_m$ and $\tilde{w}_m = \tilde{\alpha}_m / \sum_{m=0}^{2} \tilde{\alpha}_m$, where $\alpha_m = d_m/(\epsilon + \beta_m)^2$ and $\tilde{\alpha}_m = \tilde{d}_m/(\epsilon + \beta_m)^2$, with $d_0 = 3/10$, $d_1 = 6/10$, $d_2 = 1/10$, $\tilde{d}_0 = 1/10$, $\tilde{d}_1 = 6/10$, $\tilde{d}_2 = 3/10$, $\epsilon = 10^{-6}$. The expressions for the smooth indicators β_m are given by,

$$
\begin{aligned}
\beta_0 &= \frac{13}{12}(\phi_i - 2\phi_{i+1} + \phi_{i+2})^2 + \frac{1}{4}(3\phi_i - 4\phi_{i+1} + \phi_{i+2})^2 \\
\beta_1 &= \frac{13}{12}(\phi_{i-1} - 2\phi_i + \phi_{i+1})^2 + \frac{1}{4}(\phi_{i-1} - \phi_{i+1})^2 \\
\beta_2 &= \frac{13}{12}(\phi_{i-2} - 2\phi_{i-1} + \phi_i)^2 + \frac{1}{4}(\phi_{i-2} - 4\phi_{i-1} + 3\phi_i)^2
\end{aligned}
$$

The expressions for the positive and negative interpolations at the right cell face are:

$$
\begin{aligned}
\phi_r^+ &= \sum_{m=0}^{k-1} w_m \phi_r^m \\
\phi_r^- &= \sum_{m=0}^{k-1} \tilde{w}_m \phi_r^m
\end{aligned}
$$

The choice between the positive and the negative interpolation is made based on the value of the Roe-speed, $a_r = \frac{f_{i+1} - f_i}{\phi_{i+1} - \phi_i}$. Given the Roe-speed,

$$
\begin{aligned}
\phi_r &= \phi_r^-, \text{ if } a_r >= 0, \\
&= \phi_r^+, \text{ if } a_r < 0
\end{aligned}
$$

To test the predictive capabilities of the schemes just described, a simple 1-D test is conducted with a uniform periodic velocity field. Since scalar profiles in turbulent flows are rarely

smooth and involve strong gradients, a profile that involves a combination of a Gaussian, square wave, sharp triangle wave and half ellipse is used (Jiang and Shu, 1996) across the domain discretized by 256 equidistant cells. The 1-D equation solved is:

$$\frac{\partial \phi}{\partial t} + \frac{\partial u\phi}{\partial x} = 0 \quad (-1 < x < 1)$$

$$u(x,t) = 1 \quad (-1 < x < 1; t \geq 0)$$

using the initial scalar profile:

$$\phi(x,0) = \begin{cases} \frac{1}{6}\left[G(x,\beta,z-\delta) + G(x,\beta,z+\delta) + 4G(x,\beta,z)\right] & : & -0.8 \leq x \leq -0.6 \\ 1 & : & -0.4 \leq x \leq -0.2 \\ 1 - |10(x-0.1)| & : & 0 \leq x \leq 0.2 \\ \frac{1}{6}\left[F(x,\alpha,a-\delta) + F(x,\alpha,a+\delta) + 4F(x,\alpha,a)\right] & : & 0.4 \leq x \leq 0.6 \\ 0 & : & \text{otherwise} \end{cases} \quad (6.6)$$

where,

$$G(x,\beta,z) = \exp(-\beta(x-z)^2)$$

$$F(x,\alpha,a) = \sqrt{\max(1-\alpha^2(x-a)^2,0)}$$

The constants are $a = 0.5$, $z = -0.7$, $\delta = 0.005$, $\alpha = 10$ and $\beta = \log 2/36\delta^2$. A third-order Runge–Kutta method is used to advance the solution in time. The simulation is carried out for four rotations, where each rotation is defined as the time taken for the initial profile to be convected back to its initial location. Figure 6.2 compares results obtained from the four schemes with the initial condition of Eq. 6.6. The CD scheme exhibits the largest oscillations at sharp interfaces and poorly predicts the exact solution. Using the QUICK scheme, most oscillations are damped, however, the scalar values exceed the bounds of the solution. The third-order WENO scheme shows no oscillations, however it does not capture the local extrema of the scalar, which indicates that the scheme might cause damping of the resolved scalar fluctuations. The fifth-order WENO scheme captures the profiles accurately, shows no oscillations and gives the best solution.

As seen from the results, the CD and the QUICK scheme give solutions that grow out of bounds and therefore cannot be used for our purpose. Herrmann et al. (2004) recently proposed a bounded QUICK (BQUICK) scheme, which preserves scalar values within bounds. The BQUICK scheme is based on a predictor-corrector algorithm. The predictor step advances the solution using the QUICK scheme. However, when the predicted scalar value is outside of the bounds, a first-order upwind scheme is used to re-calculate the scalar flux and the corrector step advances the initial scalar field (before the predictor step) in time. Although the method uses a first-order approximation in the corrector step, it has been shown to maintain a third-order accuracy (Herrmann et al., 2004). The steps required for the BQUICK algorithm to maintain scalar boundedness are:

1. March velocity from $u_i^n \rightarrow u_i^{n+1}$.

2. March scalar from $\phi_i^n \rightarrow \phi_i^{n+1}$ based on flux evaluation (f_l, f_r) using QUICK scheme.

3. Check ϕ_i^{n+1} for boundedness. If out of bounds, re-evaluate both f_l and f_r using first-order upwind scheme:

   (a) IF $u_l \geq 0$ THEN $\phi_l = \phi_{i-1}$, ELSE $\phi_l = \phi_i$

   (b) IF $u_r \geq 0$ THEN $\phi_r = \phi_i$, ELSE $\phi_r = \phi_{i+1}$

   (c) Re-evaluate flux f_r for node $i-1$ and f_l for node $i+1$ based on first-order method.

   (d) March ϕ_{i-1}^n, ϕ_i^n, $\phi_{i+1}^n \rightarrow \phi_{i-1}^{n+1}$, ϕ_i^{n+1}, ϕ_{i+1}^{n+1} based on the new fluxes.

Based on the predictor-corrector methodology, a scheme using a second-order central difference method in the predictor step and first-order upwind method in the corrector step is also tested (Muppidi, 2006): the bounded central difference scheme (BCD). Also, a plain first-order upwind scheme is also tested in order to bring out the difference between using a first-order scheme only in the corrector step and using a first-order scheme for the convective term. Fig. 6.3 compares results from the three schemes against the exact solution. The three schemes are able to maintain the scalar values within bounds and the BQUICK scheme shows the best results. The first-order upwind scheme shows results similar to the BCD scheme, leading to the conclusion that the first-order corrector step must have been invoked often for the BCD scheme.

Based on the above tests, the first-order upwind scheme, the BCD scheme, the BQUICK scheme, the third-order WENO scheme and the fifth-order WENO schemes will be tested for the confined rectangular jet.

6.3 Governing equation and subgrid model

In order to couple the scalar transport with the governing equations (3.1) and (3.2), the non-dimensional filtered equation of passive scalar ϕ is given by,

$$\frac{\partial \overline{\phi}}{\partial t} + \frac{\partial \overline{u}_j \overline{\phi}}{\partial x_j} = \frac{1}{ReSc} \frac{\partial}{\partial x_j} \left(\frac{\partial \overline{\phi}}{\partial x_j} \right) - \frac{\partial \lambda_j}{\partial x_j} \tag{6.7}$$

where the turbulent subgrid scalar flux vector that requires modeling is given by,

$$\lambda_j = \overline{u_j \phi} - \overline{u}_j \overline{\phi} = \frac{C_s}{Sc_t} \overline{\Delta}^2 |\overline{S}| \frac{\partial \overline{\phi}}{\partial x_j}$$

A simple closure for the turbulent Schmidt number Sc_t assumes a constant value; here $Sc_t = 0.4$ is used. Closure is also obtained by using a dynamic procedure proposed by Moin et al. (1991). When the test filter is applied to the scalar transport equation, a similar expression is obtained for the subtest scalar flux,

$$\Lambda_j = \widehat{\overline{u_j \phi}} - \widehat{\overline{u}}_j \widehat{\overline{\phi}} = \frac{C_s}{Sc_t} \widehat{\Delta}^2 |\widehat{\overline{S}}| \frac{\partial \widehat{\overline{\phi}}}{\partial x_j}$$

Using the Germano identity,

$$\Lambda_j - \widehat{\lambda}_j = C_{ss} \left(-\frac{\widehat{\Delta}^2}{\overline{\Delta}^2} |\widehat{\overline{S}}| \frac{\partial \widehat{\overline{\phi}}}{\partial x_j} + \widehat{|\overline{S}| \frac{\partial \overline{\phi}}{\partial x_j}} \right)$$

Or,

$$L_j^s = C_{ss} M_j^s$$

where $C_{ss} = \frac{C_s}{Sc_t} \overline{\Delta}^2$. Using the least squares approach, the set of equations is contracted with M_j^s to obtain the value of C_{ss}:

$$C_{ss} = \frac{L_j^s M_j^s}{M_j^s M_j^s} \tag{6.8}$$

In the following sections, the effect of numerical schemes and subgrid flux models on the resolved scalar field are compared against experimental measurements.

6.4 Effect of numerical schemes

Large eddy simulations of momentum and passive scalar transport are performed for a confined rectangular jet at $Re = 20,000$ and $Sc = 1200$ and compared to PIV and PLIF measurements. Numerical schemes for the advection term can have a great effect on the scalar solution. As explained in section 6.2, the first-order upwind, the BCD, the BQUICK and the WENO schemes are used to test the predictive capabilities of the formulations. However, when the WENO schemes were tested for the passive scalar transport in the confined rectangular jet, it was found that the scalars exceeded the bounded values. The solutions also showed ringing similar to Gibb's phenomenon. Therefore, the WENO schemes will not be considered and are a part of future work. For the reactor geometry, the first-order upwind, the BCD and the BQUICK schemes will be used.

The filtered scalar transport equation is solved using these three schemes for the convection term, and a constant turbulent Schmidt number $Sc_t = 0.4$ was used to close the subgrid flux model. Figure 6.4 compares the mean resolved scalar profiles at four locations downstream of the splitter plates. PLIF results are shown as symbols and LES solution as lines. The corrector step in the bounded methods ensures conservation of the scalar mass flow rate since artificial clipping of scalars exceeding physical bounds is avoided. All three schemes are able to capture the mean profile well. At locations $x = 13$ and $x = 22$ cm, the BCD and BQUICK schemes underpredict the maximum scalar value and slightly overpredict values near the wall as compared to the experiment and the first-order upwind scheme. This is due to a higher turbulent scalar-flux transport obtained using the BCD and BQUICK schemes.

Since the scalar field is fixed at the inlet, the scalar rms profiles shown in Fig. 6.5 begin with location $x = 7$ cm. In general, the rms peaks reduce with downstream distance. However, the first-order upwind scheme dissipates the most scalar energy relative to the other schemes resulting in a lower rms, most notably at locations $x = 22$ and $x = 28$ cm. Examination of Fig. 6.5 also reveals that predictions of the scalar rms for the BCD and the BQUICK schemes are comparable. It should be noted that for the PLIF measurements, the resolution in the plane of measurements is higher than the LES filter length scale. However, the resolution in

the out-of-plane direction is coarse, leading to a lower energy in the resolved scales measured by PLIF as compared to LES, and can be seen in the turbulent scalar flux profiles shown in Fig. 6.6. The normalized streamwise and cross-stream turbulent scalar fluxes are shown only at locations of $x = 7$ and $x = 13$ cm. The fluxes resolved by the LES are higher than those measured by simultaneous PIV and PLIF, especially for the BCD and BQUICK schemes as compared to the first-order upwind scheme.

6.5   Effect of subgrid flux model

Based on the scalar results in Section 6.4, it is apparent that the subgrid model must account for the unresolved scalar energy. Simulations using the dynamic procedure (section 6.3, Eq. 6.8) to close the subgrid scalar flux are compared to the previous simulations for $Sc_t = 0.4$. Figures 6.7 and 6.8 compare the scalar mean and rms profiles for the two cases using the BQUICK scheme for the convection terms. Both closure models give an almost identical solution of the resolved scalar field. Thus the constant Sc_t model is sufficient to provide a good solution, thus saving (about 20%) computational effort required for the dynamic calculation.

6.6   Summary

Large eddy simulations were performed for scalar transport in a confined rectangular jet. An important step in obtaining a good solution is using a numerical scheme that can resolve sharp scalar gradients in the shear layer while preserving the scalar boundedness without resorting to artificial clipping. A 1-D test case with sharp initial conditions was studied to investigate the effect of numerical schemes on the scalar solution. The central-difference scheme showed the largest instabilities in the solution. The QUICK scheme reduced most of the oscillations but still exceeded the physical bounds imposed by the scalar initial conditions. The BQUICK scheme with its predictor-corrector steps was able to maintain the scalar bounds. WENO schemes provided good solutions for the 1-D test case, however, numerical instabilities (i.e., Gibb's ringing) developed for simulations of flow in the reactor geometry. The effects of a first-order upwind, the second-order BCD scheme and the third-order BQUICK scheme were studied on the resolved scale statistics for the rectangular jet. Overall, the scalar mean and rms

profiles compared well PLIF measurements. Results using the second- and third-order schemes showed higher turbulent fluxes across the shear layers. The dynamic closure model did not show any significant improvement with accuracy of the solution as compared to the case when a constant turbulent Schmidt number was used. The state of the art PLIF and simultaneous PIV and PLIF measurements of the confined jet reactor are unique and the validation of the filtered scalar transport equation using LES for large Schmidt number flows is an important contribution of this work to the LES literature.
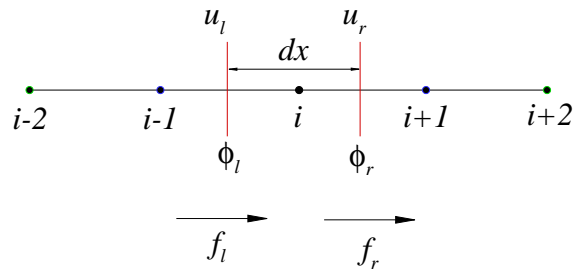
Figure 6.1   A 1-D schematic to illustrate scalar flux evaluation.
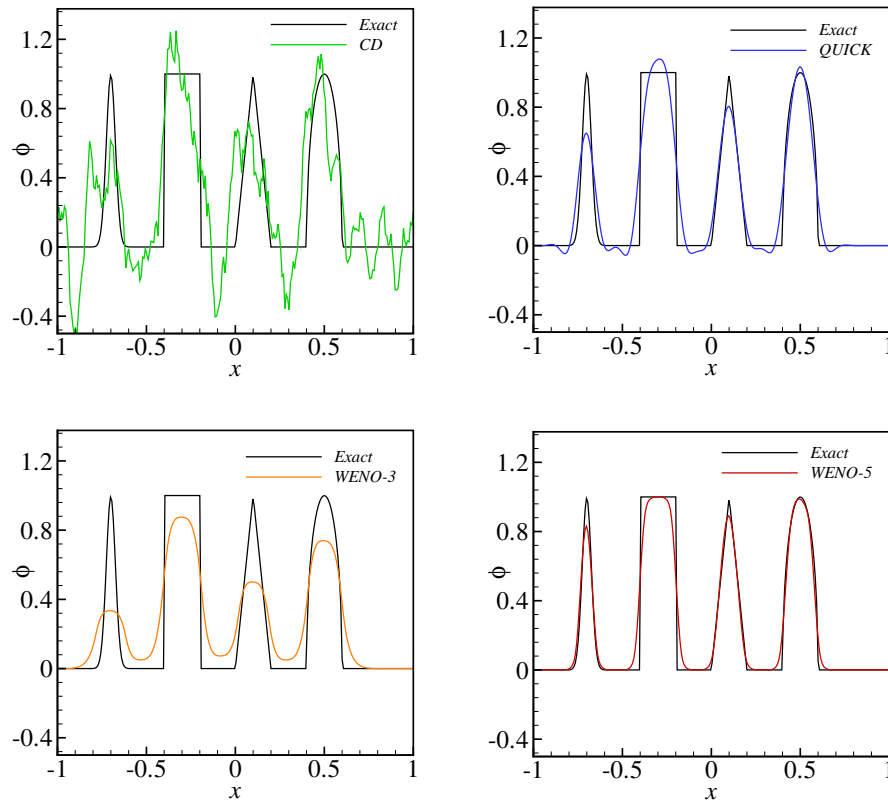
Figure 6.2   1-D convection test case comparing numerical schemes. Exact solution shown in black and numerical solutions are shown as a dotted line.
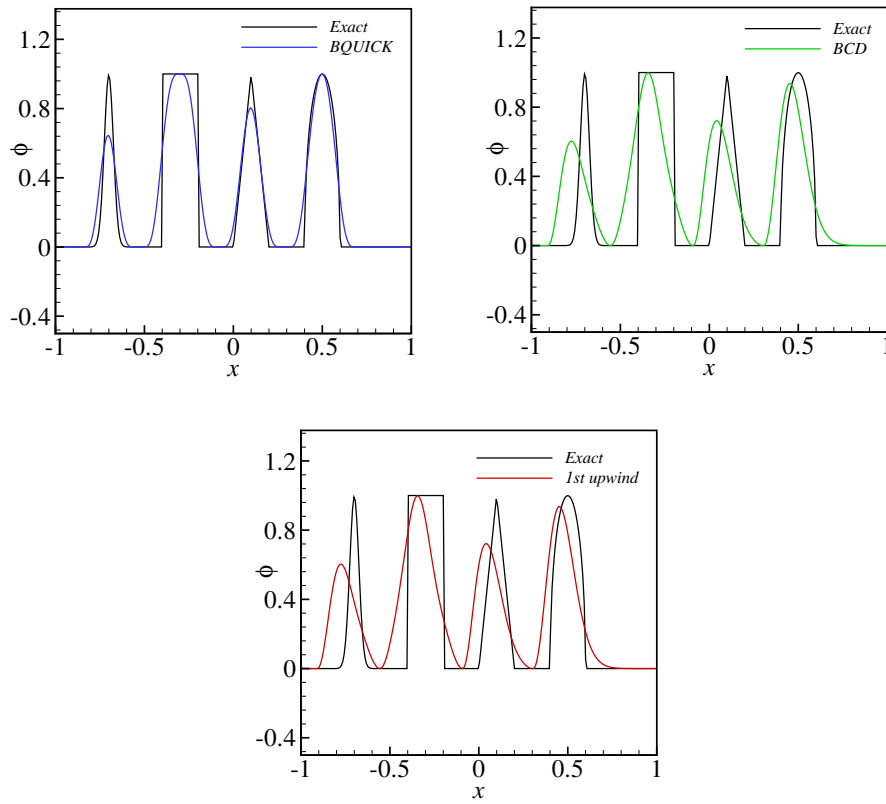
Figure 6.3   1-D convection test case comparing numerical schemes. Exact solution shown in black and numerical solutions are shown as a dotted line.
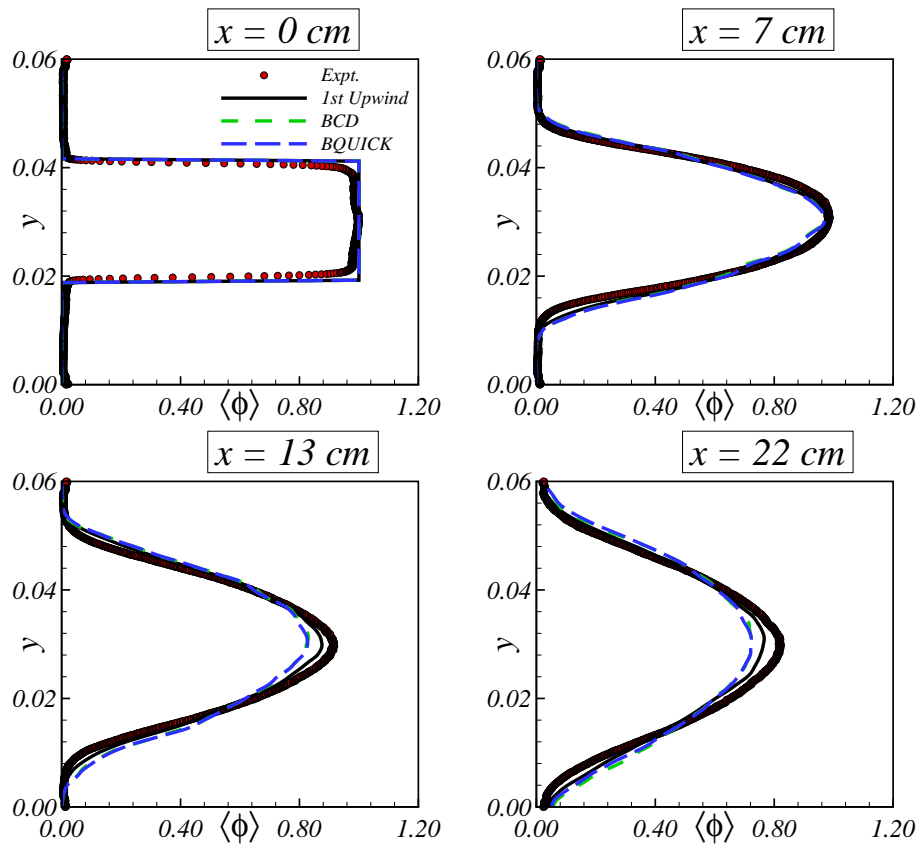
Figure 6.4   Mean scalar profiles at four streamwise locations downstream of
the splitter plates using a constant turbulent Schmidt number.

94
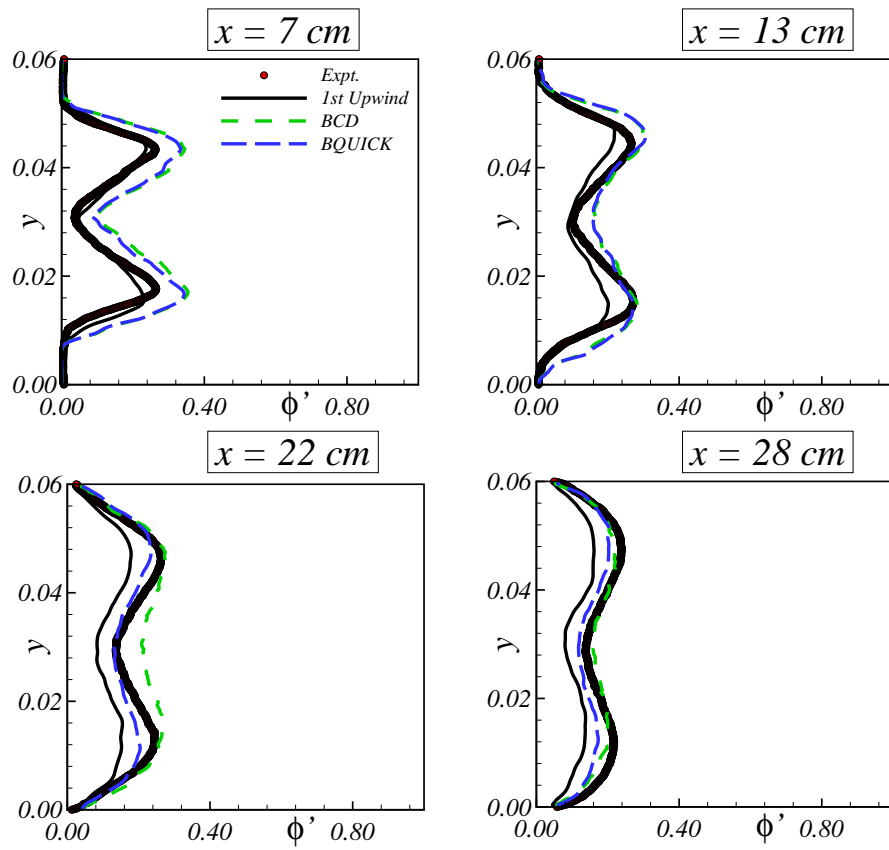
Figure 6.5   Scalar rms profiles at four streamwise locations downstream of
the splitter plates using a constant turbulent Schmidt number.
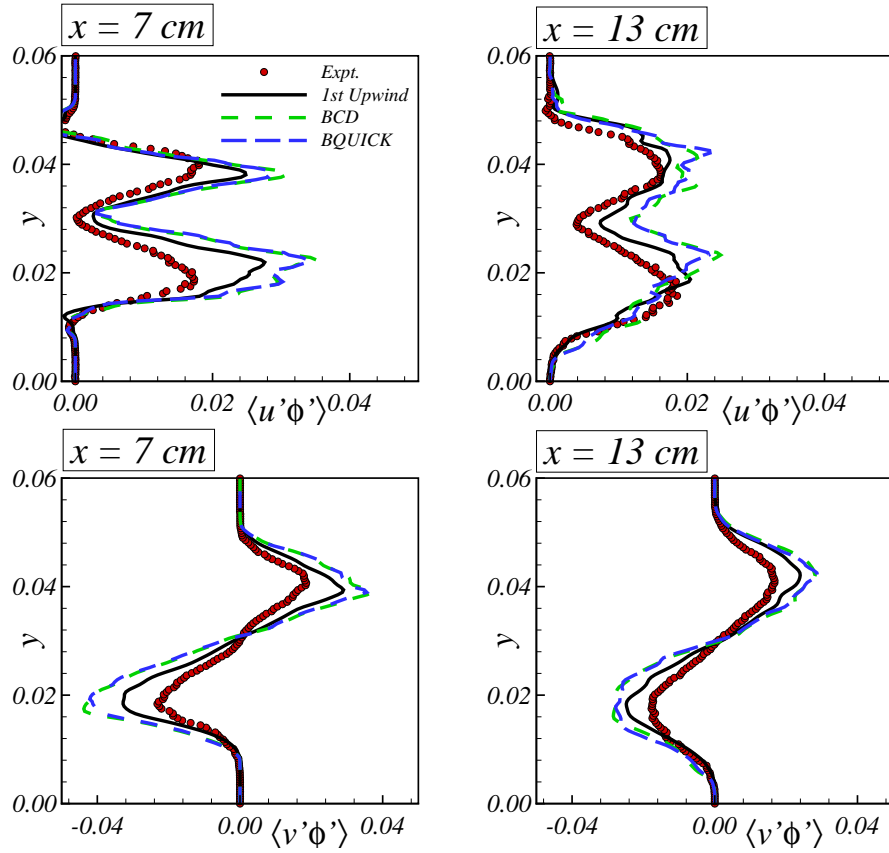
Figure 6.6   Normalized streamwise and cross-stream scalar flux profiles at
            $x = 7$ and $x = 13$ cm using a constant turbulent Schmidt
            number.
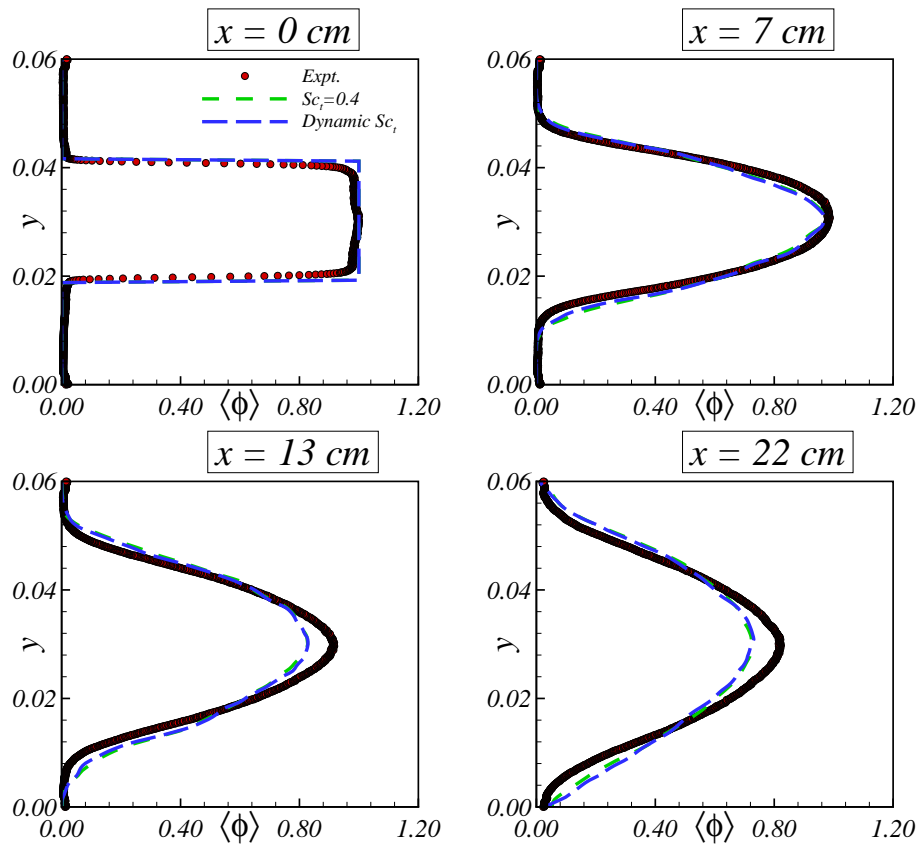
Figure 6.7   Mean scalar profiles at four streamwise locations downstream of the splitter plates.
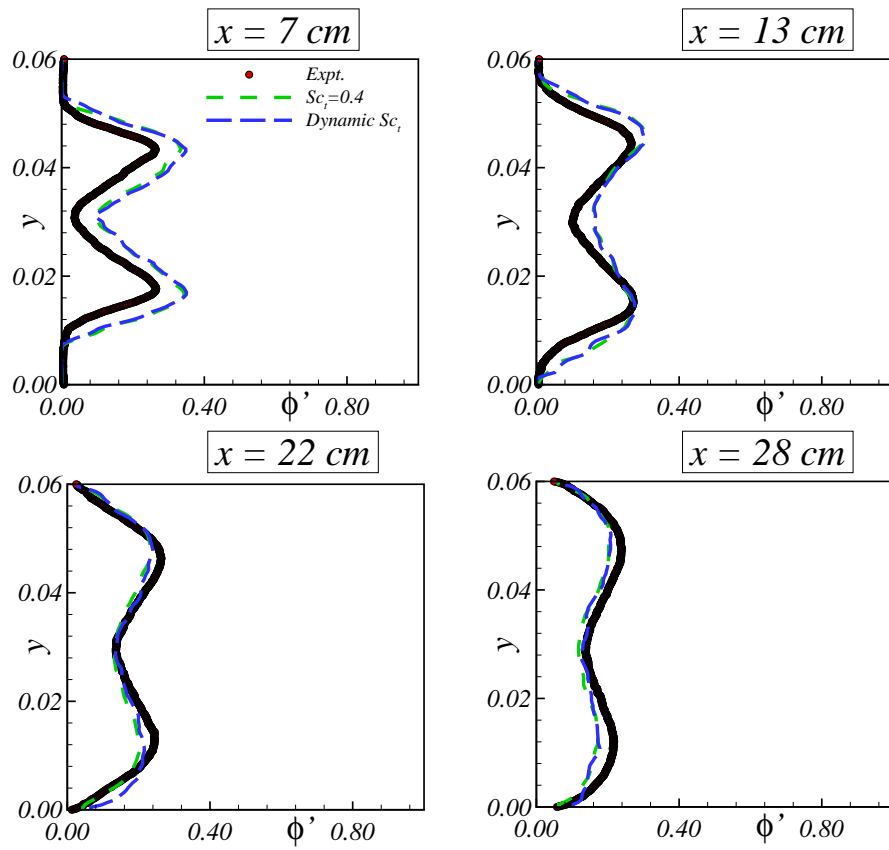
Figure 6.8   Scalar rms profiles at four streamwise locations downstream of the splitter plates.

CHAPTER 7.   CONCLUSIONS AND FUTURE WORK

A robust code for large eddy simulations of turbulent flows with application to the confined jet reactor was developed. A critical step in the stability of the solution was staggering the pressure to the cell center. This work represents the first time that the partial staggered scheme has been used for LES. Another step was making the code amenable to parallel computing utilizing MPI routines and parallel libraries for matrix inversion. A parallel iterative solver, *Aztec*, was used for solving the pressure Poisson equation. Validation of the solution algorithm was performed for driven cavity flows and flow over a backward facing step (both laminar flows). The subgrid scale model validation was performed by simulating a turbulent channel flow and comparing the LES with DNS and experiments that are well documented in the literature. Performance of the code on an Opteron cluster at Iowa State University was performed and a linear speed up was obtained up to 192 processors, indicating the amount of time savings that could be achieved in the numerical computations in this research.

Turbulent mixing in a confined rectangular jet was studied using large eddy simulations and results were validated with PIV and PLIF measurements. The Reynolds number of the jet was 20,000 based on the hydraulic diameter and average velocity at the inlet. The Schmidt number of the fluorescence dye was 1,200. Flow statistics such as mean velocity, rms velocity, Reynolds stresses, correlation coefficients, skewness and kurtosis were calculated and compared with measurements at multiple locations. The effect of grid resolution, numerical schemes and subgrid models were studied on the resolved scale solution. It must be pointed out that since the filter size is not independent of the grid resolution, an accurate grid independence study cannot be performed. However, a resolution necessary to capture the mean profile accurately was chosen. The LES statistics agreed very well with those obtained from PIV measurements. The most notable results from the study were the two-point velocity spatial correlations obtained at

several locations within the domain. LES correctly predicts the length scales and the orientation of the large scale structures. The quantitative and qualitative agreement of these correlations was excellent and such detailed statistics have not been published in literature so far.

LES of the passive scalar transport was also performed for the same geometry and compared with PLIF measurements of resolved scalar statistics and simultaneous PIV and PLIF measurements of the scalar fluxes. The resolution of the PLIF measurements is coarser than the LES filter length scale since the depth of the laser sheet is quite large. Thus the resolved LES scalar field predicted more energy than the measurements. An issue with the numerics was that sharp gradients exist at the inlet and with a low molecular diffusivity, the scalar solution tends to exhibit oscillations similar to the Gibbs ringing effect. Another constraint on the scalar was that it should maintain the boundedness imposed by the initial and the boundary conditions. Several schemes were tested for a 1-D test case, including a bounded scheme based on predictor-corrector steps. The schemes used for the solving scalar transport in the reactor geometry were based on a second-order central difference or a third-order QUICK scheme for the scalar flux in the predictor step and an upwind scheme for the corrector step (BCD and BQUICK, respectively), with the fluxes evaluated at the interface between grid nodes. The schemes maintained scalar boundedness without the need for any artificial clipping. The bounded schemes were used to discretize the convective term in the filtered passive scalar transport equation for the rectangular jet. The first-order upwind scheme, although bounded and conservative, is dissipative in nature and is not suitable with the LES methodology. The resolved scale scalar mean and rms profiles were close to those measured using PLIF. The dynamic subgrid flux model did not show any improvement in accuracy as compared to the case when a constant turbulent Schmidt number was used. The turbulent scalar flux obtained from LES showed higher values since the resolution of the LES was better then the simultaneous PIV and PLIF measurements. Overall, the best scheme was the BQUICK for the convection term with a constant Sc_t because a higher-order accuracy of the solution is maintained and time savings are made by not resorting to the dynamic subgrid scalar flux model.

Future Work

The future direction of this research lies in the validation of models for turbulent reacting flows. The LES methodology breaks down when the rate controlling mechanism occurs at unresolved scales, which is the case with reacting flows at high Schmidt numbers. The resolved scale mixture fraction is known, but the SGS fluctuations are not resolved and information about the SGS mixture fraction PDF is required to compute resolved scale reacting scalar fields. Thus, LES of turbulent reacting flows has closure problems associated with the chemical source term. In the present research, focus is on non-premixed liquid reacting flows, which are characterized by high Schmidt numbers. Such flows are often described by a mixture-fraction variable and a reaction-progress variable (Fox, 2003).

A mixture fraction is obtained from a linear combination of the reacting scalars (Toor, 1975) such that the source term in the mixture–fraction transport equation is null (just like in a non-reacting scalar transport equation). The motivation is that simple forms for the mixture-fraction PDF can be employed to describe the reacting scalars. According to the manner in which the subgrid scale concentration fluctuations are treated in the closure for the chemical source term, the models can be roughly classified into four general categories: moment methods, conditional moment methods, presumed PDF methods and transported PDF methods (Fox, 2003). These methods although well understood, have not been thoroughly validated due to lack of experimental data. The models could be tested in the LES code for simple reaction schemes against PLIF measurements.

For more complex reactions, only a one-point, one-time joint composition PDF can describe the source term completely, however, only DNS is capable of resolving the finest of structures to provide such information, which is feasible only for simple flows (Fox, 2003). The alternative is to use transported PDF methods where a joint PDF is solved for the SGS fluctuations of all concentrations. The method has a distinct advantage in that the chemical source terms appear in closed form and require no modeling. Unlike presumed PDF methods, transported PDF methods do not require apriori knowledge of the joint composition PDF. The methods are the most computationally demanding of all macroscopic models for turbulent reacting flows.

However, they offer the only known solution for treating finite-rate chemistry that is often associated with pollutant information. Although the chemical source term is treated exactly, modeling is required for molecular mixing (micromixing models), which describes the effect of molecular diffusion on the shape of the PDF. A disadvantage of the method is that being a one-point, one-time PDF, no length or time scale information is available from the PDF, hence, the mixing time scales have to be related to turbulence time scales through a model for the scalar dissipation rate (Pope, 1985; Tsai and Fox, 1995; Fox, 1996; Cha and Trouillet, 2003). One such lagrangian PDF code has been developed at Iowa State University and is expressed in terms of a stochastic differential equations for the position and composition of "notional" particles (Raman et al. 2001, 2003, 2004). This code could be coupled with the present LES code for solving complex reactions where solution for the velocity field is obtained from the LES and the PDF code solves for the scalars. Validations can then be performed for micromixing models in literature.

BIBLIOGRAPHY

Armaly, B.F., Durst, F., Pereira, J.C.F. and Schonung, B. (1983). Experimental and theoretical investigation of backward-facing step flow. *Journal of Fluid Mechanics*, *127*, 473–496.

Baldyga, J. and Bourne, J.R. (1999). *Turbulent Mixing and Chemical Reactions*. John Wiley & Sons, Inc., New York.

Baldyga, J. and Henczka, M. (1997). The use of a new model of micromixing for determination of crystal size in precipitation. *Récent Progrès en Génie des Procèdès*, *11*, 341–348.

Bardina, J., Ferziger, J.H. and Reynolds, W.C. (1980). Improved subgrid scale models for large eddy simulation. *AIAA Paper*, *80*, 1357–1366.

Battaglia, F. and Givi, P. (1993). Direct Lagrangian simulations of a mixing layer by the transport-element method. *Journal of Non-Equilibrium Thermodynamics*, *18*, 173–194.

Benocci C. and Pinelli A. (1990). The role of the forcing term in the large eddy simulation of equilibrium channel flow. *Engineering Turbulence Modeling and Experiments, Rodi W, Ganic EN., eds., Elsevier Science Ltd*, New York, 287–296.

Bernal, L.P. and Roshko, A. (1986). Streamwise vortex structure in plane mixing layers. *Journal of Fluid Mechanics 170*, 499–525.

Berselli, L.C., ILiescu, T. and Layton, W.J. (2006). *Mathematics of large eddy simulation of turbulent flows.* Springer

Bilger, R.W. (1993). Conditional moment closure for turbulent reacting flow. *Physics of Fluids A: Fluid Dynamics 5*, 436–444.

Brethouwer, G., Hunt, J.C.R. and Nieuwstadt, F.T.M. (2003). Micro-structure and Lagrangian statistics of the scalar field with a mean gradient in isotropic turbulence. *Journal of Fluid Mechanics*, *474*, 193–225.

Brodkey, R.S. (1974). *Turbulence in mixing operations.* Academic Press, New York.

Browand, F.K. and Ho, C.-M. (1983). The mixing layer: An example of quasi two-dimensional turbulence. *Journal de Mécanique théorique et appliquée Numéro spécial*, 99–120.

Browand, F.K., Weidman, P.D. (1976). Large scales in the developing mixing layer. *Journal of Fluid Mechanics*, *76*, 127–144.

Brown, G.L. and Roshko, A. (1974). On density effects and large structure in turbulent mixing layers. *Journal of Fluid Mechanics*, *64*, 775–816.

Buch, K.A. and Dahm, W.J.A. (1996). Experimental study of the fine-scale structure of conserved scalar mixing in turbulent shear flows. Part 1. $Sc \gg 1$. *Journal of Fluid Mechanics*, *317*, 21–71.

Buch, K.A. and Dahm, W.J.A. (1998). Experimental study of the fine-scale structure of conserved scalar mixing in turbulent shear flows. Part 2. $Sc \approx 1$. *Journal of Fluid Mechanics*, *364*, 1–29.

Burton, C.G. (2005). Large-eddy simulation of passive-scalar mixing using multifractal subgrid-scale modeling. In *Annual Research Briefs*, 211–222. Stanford, CA: Center for Turbulence Research.

Bushe, W.K. and Steiner, H. (1999). Conditional moment closure for large eddy simulation of nonpremixed turbulent reacting flows. *Physics of Fluids 11*, (7), 1896–1906.

Cha, C.M. and Trouillet, P. (2003). A model for the mixing time scale of a turbulent reacting scalar. *Physics of Fluids 15*,

Chakrabarti, M. and Hill, J.C. (1997). First order closure theories for series–parallel reaction simulated homogeneous turbulence. *AICRE Journal 43*, 902–912.

Chorin, A. (1967). A numerical method for solving incompressible viscous flow problems. *Journal of Computational Physics*, *2*, 12–26.

Chorin, A.J. (1968). Numerical solution of the Navier–Stokes equations. *Journal of Mathematical Computation*, *22*, 745–762.

Chumakov, S. (2001). *Large-eddy simulation models for subgrid scalar transport.*, MS thesis, University of Wisconsin - Madison.

Colucci, P.J., Jaberi, F.A., Givi, P. and Pope, S.B. (1998). Filtered density function for large eddy simulation of turbulent reacting flows. *Physics of Fluids 6*, 2868–2870.

Cook, A.W. and Riley, J.J. (1994). A subgrid model for equilibrium chemistry in turbulent flows. *Physics of fluids 6*, (8), 2868–2870.

deBruynKops, S.M. and Riley, J.J. (2001). Mixing models for Large–Eddy Simulation of Non-premixed Turbulent Combustion. *Journal of Fluids Engineering 123*, 341–346.

Dahm, W.J.A., Southerland, K.B. and Buch, K.A. (1991). Direct, high resolution, four-dimensional measurements of the fine scale structure of $Sc \gg 1$ molecular mixing in turbulent flows. *Physics of Fluids A: Fluid Dynamics*, *3*, 1115–1127.

Danckwerts, P.V. (1953). Continuous flow systems: distribution and residence times. *Chemical Engineering Science 2*

Dimotakis, P.E. (1986). Two-Dimensional Shear-Layer Entrainment, *AIAA Journal 24*, (11), 1791–1796.

Dimotakis, P.E. and Brown, G.L. (1976). The mixing layer at high Reynolds number: large–structure dynamics and entrainment. *Journal of Fluid Mechanics*, *78*, 535–560.

Dong, Y-H., Lu, X-Y. and Zhuang, L-X. (2003). Large eddy simulation of turbulent channel flow with mass transfer at high-Schmidt numbers. *International Journal of Heat and Mass Transfer*, *46*, 1529–1539.

Ducros, F., Comte, P. and Lesieur, M. (1996). Large-eddy simulation of transition to turbulence in a boundary layer spatially developing over a flat plate. *Journal of Fluid Mechanics*, *326*, 1–36.

Dutta, A. and Tarbell, J.M. (1989). Closure models for turbulent reacting flows. *AIChE Journal 35*, 2013–2027.

Eswaran V. and Pope S.B. (1987). Direct numerical simulations of the turbulent mixing of a passive scalar. *Physics of Fluids*, *31*, (3), 506–520.

Feng, H., Olsen, M.G., Liu, Y., Fox, R.O. and Hill, J.C. (2005). Investigation of turbulent mixing in a confined planar-jet reactor. *AIChE Journal 51*, (10), 2649–2664.

Ferziger, J.H. and Perić ,M. (2002). *Computational methods for Fluid Dynamics.* New York: Springer.

Forney, L.J., Nafia, N. and Vo, H.X. (1996). Optimum jet injection in a tubular reactor. *AIChE Journal 42*, (11), 3113–3122.

Fortin, M., Peyret, R. and Temam, R. (1971). *Lecture Notes in Physics*, *8*, 337–342. Springer–Verlag, New York.

Fox, R.O. (1996). Computational methods for turbulent reacting flows in chemical process industry. *Revue de l'Instut Français du Pétrole 52*, 215–243.

Fox, R.O. (2003). *Computational Models for Turbulent Reacting Flows.* Cambridge University Press

Galperin, B. and Orszag, S.A. (1993). *Large eddy simulation of complex engineering and geo-physical flows.* Cambridge University Press

Gao, F. and O'Brien, E.E. (1993). A large–eddy simulation scheme for turbulent reacting flows. *Physics of Fluids A 5*, (6), 1282–1284.

Germano, M. (1986). A proposal for a redefinition of the turbulent stresses in the filtered Navier-Stokes equations. *Physics of Fluids*, *29*, 2323–2324.

Germano, M., Piomelli, U., Moin P. and Cabot, W.H. (1991). A dynamic subgrid-scale eddy viscosity model. *Physics of Fluids A*, *3*, (7), 1760–1765.

Geurts, B.J. (1997). Inverse modeling for large-eddy simulation. *Physics of Fluids*, *9*, (12), 3585–3587.

Gibson, C.H. and Libby, P.A. (1972). On turbulent flows with fast chemical reactions. Part II - The distribution of reactants and products near reacting surfaces. *Combust. Sci. Tech.*, *8*, 29–35.

Gicquel, L.Y., Jaberi, F.A., Givi, P. and Pope, S.B. (2002). Velocity filtered density function for large eddy simulation of turbulent flows. *Physics of Fluids 14*, 1196–1213.

Ghia, U., Ghia, K.N. and Shin, C.T. (1982). High-Re solutions for incompressible flow using the Navier-Stokes equations and a multigrid method. *Journal of Computational Physics*, *48*, 387–411.

Ghosal, S., Lund, T., Moin, P. and Akselvoll, K. (1995). A dynamic localization model for large-eddy simulation of turbulent flows. *Journal of Fluid Mechanics*, *286*, 229–255.

Ghosal, S. (1996). An analysis of numerical errors in large–eddy simulations of turbulence. *Journal of Computational Physics*, *125*, 187–206.

Grinstein, F.F., Oran, E.S. and Boris J.P. (1985). Numerical simulations of asymmetric mixing in planar shear flows. *Journal of Fluid Mechanics*, *165*, 201–220.

Harlow, F.H. and Welch, J.E. (1965). Numerical calculation of time-dependent viscous incompressible flow of fluid with free surface. *The Physics of Fluids*, *8*,(12) 2182–2189.

Heeb, T.G. and Brodkey, R.S. (1990). Turbulent mixing with multiple second–order chemical reactions. *AIChE Journal 36*, 1457–1470.

Herrmann, M., Blanquart, G. and Raman, V. (2004). Flux corrected finite-volume scheme for preserving scalar boundedness in reacting large-eddy simulations. In *Annual Research Briefs*, 75–85. Stanford, CA: Center for Turbulence Research.

Hill, J.C. (1976). Homogeneous turbulent mixing with chemical reactions. *Annual Review of Fluid Mechanics 8*, 135–161.

Hua Feng (2006). Experimental study of turbulent mixing in a rectangular reactor. Ph.D. Dissertation, Dept. of Mechanical Engineering, Iowa State University, Ames, IA.

Ho, C.-M. and Huang, L.-S. (1982). Subharmonics and vortex merging in mixing layers, *Journal of Fluid Mechanics 119*, 443–473.

Jaberi, F.A., Colucci, P.J., James, S., Givi, P. and Pope, S.B. (1999). Filtered mass density function for large–eddy simulation of turbulent reacting flows. *Journal of Fluid Mechanics 401*, 85–121.

Jiang, G-S. and Shu, C-W. (1996). Efficient implementation of weighted ENO schemes. *Journal of Computational Physics*, *126*, 202–228.

Jovanović, J. (2004). *The Statistical Dynamics of Turbulence.* Springer

Kim, W.-W. and Menon, S. (1999). An unsteady incompressible Navier–Stokes solver for large eddy simulation of turbulent flows. *International Journal for Numerical Methods in Fluids*, *31*, 983–1017.

Kim, J. and Moin, P. (1985). Application of a fractional–step method to incompressible Navier–Stokes equations. *Journal of Computational Physics*, *59*, 308–323.

Kim, J., Moin, P. and Moser, R.D. (1987). Turbulence statistics in fully–developed channel flow at low Reynolds number. *Journal of Fluid Mechanics*, *177*, 133–166.

Klein, M., Sadiki, A. and Janicka, A. (2003). A digital filter based generation of inflow data for spatially developing direct numerical or large eddy simulations. *Journal of Computational Physics*, *186*, 652–665.

Klimenko, A.Y. (1990). Multicomponent diffusion of various admixtures in turbulent flow. *Fluid Dynamics 25*, 327–334.

Koochesfahani, M.M. and Dimotakis, P.E. (1986). Mixing and chemical reactions in a turbulent liquid mixing layer. *Journal of Fluid Mechanics*, *170*, 83–112.

Koochesfahani, M.M., Dimotakis, P.E. and Broadwell, J.E. (1983). Chemically reacting turbulent shear layers. *AIAA paper*, 83-0475, New York.

Korczak, K.Z. and Wessel, R.A. (1989). Mixing Control in a Plane Shear Layer. *AIAA Journal* *27*, (12), 1744–1751.

Koseff, J.R., Street, R.L., Gresho, P.M., Upson, C.D., Humphrey, J.A. and To, W-M. (1982). A three–dimensional lid–driven cavity flow:experiment and simulation. *Proceedings of the 3rd International Conference on numerical methods in laminar and turbulent flow*, 564–591.

Lasheras, J.C., Cho, J.S. and Maxworthy, T. (1986). On the origin and evolution of streamwise vortical structures in a plane, free shear layer. *Journal of Fluid Mechanics 172*, 231–258.

Lele, S.K. (1992). Compact finite difference schemes with spectral like resolution. *Journal of Computational Physics*, *103*, 16–42.

Leonard, A. (1974). Energy cascade in large eddy simulation of turbulent fluid flow. *Advances in Geophysics 18*, 237–248.

Leonard, B.P. (1979). A stable and accurate convective modelling procedure based on quadratic upstream interpolation. *Computer Methods in Applied Mechanics and Engineering*, *19*, 59–98.

Lesieur, M. and Métais, O. (1996). New trends in large–eddy simulations of turbulence. *Annual Review of Fluid Mechanics*, *28*, 45–82.

Lilly, D.K. (1992). A proposed modification of the Germano subgrid-scale closure method. *Physics of Fluids A*, *4*, (3), 633–635.

Liu, S., Meneveau, C. and Katz, J. (1994). On the properties of similarity subgrid scale models as deduced from measurements in a turbulent jet. *Journal of Fluid Mechanics*, *275*, 83–119.

Lumley, J.L. and Newman, G.R. (1977). The return to isotropy of homogeneous turbulence. *Journal of Fluid Mechanics*, *82*, (1) 161–178.

Mahesh, K., Hou, Y. and Babu, P. (2005). Three problems in the large-eddy simulation of complex turbulent flows. In *Complex Effects in Large Eddy Simulation*. Limassol, September 20-24.

Masutani, S.M. and Bowman, C.T. (1986). The structure of a chemically reacting plane mixing layer. *Journal of Fluid Mechanics 172*, 93–126.

Meneveau, C. and Katz, J. (2000). Scale-invariance and turbulence models for large eddy simulations. *Annual Review of Fluid Mechanics*, *32*, 1–32.

Meneveau, C., Lund, T.S. and Cabot, W.H. (1996). A Lagrangian dynamic subgrid-scale model of turbulence. *Journal of Fluid Mechanics*, *319*, 353–385.

Menon, S., Yeung, P.K. and Kim, W. (1996). Effect of subgrid models on the computed inter-scale energy transfer of isotropic turbulence. *Computers and Fluids*, *25*, (2), 165–180.

Mètais, O. and Lesieur, M. (1992). Spectral large-eddy simulation of isotropic and stably stratified turbulence. *Journal of Fluid Mechanics*, *239*, 157–194.

Merkle, C.L. (1994). Unified time-marching procedure for compressible and incompressible flow. *Proceedings of the International Conference on Hydrodynamics*, Wuxi, China.

Moin, P. and Kim, J. (1982). Numerical investigation of turbulent channel flow. *Journal of Fluid Mechanics*, *118*, 341–377.

Moin, P., Squires, K., Cabot, W. and Lee, S. (1991). A dynamic subgrid-scale model for compressible turbulence and scalar transport. *Physics of Fluids A*, *3*, (11), 2746–2757.

Moser, R.D. and Rogers, M.M. (1993). The three-dimensional evolution of a plane mixing layer: Pairing and transition to turbulence. *Journal of Fluid Mechanics 247*, 275–320.

Mungal, M.G. and Dimotakis, P.E. (1984). Mixing and combustion with low heat release in a turbulent shear layer. *Journal of Fluid Mechanics*, *148*, 349–382.

Muppidi Suman (2006). Direct numerical simulations and modeling of jets in crossflow. Ph.D. Dissertation, Dept. of Mechanical Engineering, The University of Minnesota, MN.

Olsen, M.G. and Dutton, J.C. (2002). Stochastic estimation of large structures in an incompressible mixing layer. *AIAA Journal*, *40*, (12) 2431–2438.

Patankar, S.V. (1980). *Numerical heat transfer and fluid flow.* New York: McGraw-Hill.

Patterson, G.K. (1990). Simulating turbulent–field mixers with multiple second–order chemical reactions. *AIChE Journal*, *36*

Pierce, C.D. (2001). *Progress variable approach for large-eddy simulation of turbulence combustion.*, Ph.D. thesis, Stanford University.

Pierce, C. and Moin, P. (1998). A dynamic model for subgrid–scale variance and dissipation rate of a conserved scalar. *Physics of fluids 10*, (12), 3041–3044.

Piomelli, U. and Balaras, E., (2002). Wall–layer models for large–eddy simulations. *Annual Review of Fluid Mechanics 34*, 349–374.

Piomelli, U. and Liu, J. (1995). Large-eddy simulation of rotating channel flows using a localized dynamic model. *Physics of Fluids*, *4*, 839–848.

Pipino, M. and Fox, R.O. (1994). Reactive mixing in a tubular jet reactor: A comparison of PDF simulations with experimental data. *Chemical Engineering Science*, *49*, 5229–5241.

Pope, S.B. (1985). PDF methods for turbulent reactive flows. *Progress in Energy and Combustion Science. 11*, 119–192.

Pope, S.B. (2000). *Turbulent Flows.* Cambridge University Press

Porté–Agel, F., Meneveau, C. and Parlange, M. (2000). A scale–dependent dynamic model for large–eddy simulation: application to a neutral atmospheric boundary layer. *Journal of Fluid Mechanics*, *415*, 261–284.

Raman, V, Fox, R.O., Harvey A.D. and West, D.H. (2001). CFD analysis of premixed methane chlorination reactors with detailed chemistry. *Industrial and Engineering Chemistry*, *40*, 5170–5176.

Raman, V, Fox, R.O., Harvey A.D. and West, D.H. (2003). Effect of feed-stream configuration on gas-phase chlorination reactor performance. *Industrial and Engineering Chemistry, 42,* 2544–2557.

Raman, V, Fox, R.O., and Harvey A.D. (2004). Hybrid finite-volume/transported PDF simulations of a partially premixed methane-air flame. *Combustion and Flame, 136,* 327–350.

Ranade, V.V. (2002). *Computational Flow Modeling for Chemical Reactor Engineering.* Academic Press.

Réveillon, J. and Vervisch, L. (1996). Response of the dynamic LES model to heat release induced effects. *Physics of Fluids 8,* (8), 2248–2250.

Ribault, C.L., Sarkar, S. and Stanley, S.A. (2001). Large eddy simulation of evolution of a passive scalar in plane jet. *AIAA Journal, 39,* (8), 1509–1516.

Rogallo, R.S. and Moin, P. (1985). Numerical simulations of turbulent flows. *Annual Review of Fluid Mechanics, 17,* 99–137.

Rogers, M.M. and Moser, R.D. (1992). The three-dimensional evolution of a plane mixing layer: the Kelvin-Helmholtz rollup. *Journal of Fluid Mechanics 243,* 183–226.

Roshko, A. (1976). Structure of turbulent shear flows: A new look. *AIAA Journal, 14,* (10), 1349–1357.

Slessor, M.D., Bond, C.L. and Dimotakis, P.E. (1998). Turbulent shear-layer mixing at high Reynolds numbers: effects of inflow conditions. *Journal of Fluid Mechanics 376,* 115–138.

Smagorinsky, J. (1963). General circulation experiments with the primitive equations. Part I. The basic experiment. *Monthly Weather Review, 91,* 99–164.

Shaw, R.H., Brunet, Y., Finnigan, J.J. and Raupach, M.R. (1995). A wind tunnel study of air flowing in waving wheat: Two-point velocity statistics. *Boundary-Layer Meteorology, 76,* 349–376.

Shenoy, U.V. and Toor, H.L. (1990). Unifying indicator and instantaneous reaction methods of measuring micromixing. *AIChE Journal 36*, 227–232.

Shu, C-W. (1997). Essentially non-oscillatory and weighted essentially non-oscillatory schemes for hyperbolic conservation laws. *Lecture Notes in Mathematics*, *1697*, 325–432.

Snir, M., Otto, S., Huss-Lederman, S., Walker, D. and Dongarra, J. (2001). *MPI - The complete reference.* Volume 1, The MPI Core Second Edition, The MIT Press.

Sotiropoulos, F. and Abdallah, S. (1991). The discrete continuity equation in primitive variable solutions of incompressible flow. *Journal of Computational Physics*, *95*, 212–227.

Steiner, H. and Bushe, W.K. (2001). Large eddy simulation of a turbulent reacting jet with conditional source–term estimation. *Physics of Fluids 13*, (3), 754–769.

Stoessel, A., Hilka, M. and Baum, M. (1996). Parallel direct numerical simulation of turbulent reactive flow. *Direct numerical simulation for turbulent reacting flows*, Éditions Technip, 33–47.

Stolz, S. and Adams, N.A. (1999). An approximate deconvolution procedure for large-eddy simulation. *Physics of Fluids*, *11*, (7), 1699–1701.

Tannehill, J.C., Anderson, D.A. and Pletcher, R.H. (1997). *Computational Fluid Mechanics and Heat Transfer.* Taylor and Francis

Thom, A. (1933). The flow past circular cylinder at low speeds. *Procedures, R. Soc. London*, *141*, 651–666.

Toor, H.L. (1975). The non–premixed reaction, in "Turbulence in Mixing Operations", Ed. Brodkey, R.S., Academic Press, New York.

Tsai, K. and Fox, R.O. (1995). Modeling multiple reactive scalar mixing with the generalized IEM model. *Physics of Fluids 7*, 2820–2830.

Tsai, K. and Fox, R.O. (1996). Modeling the scalar dissipation rate for a series–parallel reaction. *Chemical Engineering Science*, *51*, 1929–1938.

Tuminaro, R.S., Heroux, M., Hutchinson, S.A. and Shadid, J.N. (1999). Official Aztec User's Guide: Version 2.1. *http://www.cs.sandia.gov/CRF/aztec1.html*.

van Driest, E.R. (1956). On turbulent flow near a wall. *Journal of Aerospace Sciences*, *23*, 1007.

Vasilyev, O.V., Lund, T.S. and Moin, P. (1998). A general class of commutative filters for LES in complex geometries. *Journal of Computational Physics*, *146*, 82–104.

Vedula, P., Yeung, P.K. and Fox, R.O. (2001). Dynamics of scalar dissipation in isotropic turbulence: a numerical and modelling study. *Journal of Fluid Mechanics*, *433*, 29–60.

von Kaenel, R., Adams, N.A. and Kleiser, L. (2002). An approximate deconvolution model for large-eddy simulation of compressible flows with finite volume schemes. *Journal of Fluids Engineering*, *124*, (4), 829–835.

Vreman, B., Geurts, B. and Kuerten, H. (1997). Large-eddy simulation of the turbulent mixing layer. *Journal of Fluid Mechanics 339*, 357–390.

Wall, C., Boersma, B.J. and Moin, P. (2000). An evaluation of the assumed beta probability density function subgrid–scale model for large eddy simulation of nonpremixed, turbulent combustion with heat release. *Physics of Fluids 12*, (10), 2522–2529.

Winant, C.D. and Browand, F.K. (1974). Vortex pairing: the mechanism of turbulent mixing-layer growth at moderate Reynolds number. *Journal of Fluid Mechanics*, *63*, 237–255.

Wray, A.A. (1990). Minimal storage time-advancement schemes for spectral methods. *tech. rep., Center for turbulence research Report, Stanford University*.

Yeung, P.K., Xu, S. and Sreenivasan, K.R. (2002). Schmidt number effects on turbulent transport with uniform mean scalar gradient. *Physics of Fluids*, *14*, 4178–4191.

Yeung, P.K., Xu, S., Donzis, D.A. and Sreenivasan, K.R. (2004). Simulations of three-dimensional turbulent mixing for Schmidt numbers on the order of 1000. *Flow, Turbulence and Combustion*, *72*, 333–347.

Zang, Y., Street, R. and Koseff, J. (1993). A dynamic mixed subgrid scale model and its application to turbulent recirculation flows. *Physics of Fluids A*, *5*, 3186–3196.